INTERFACIAL CHEMISTRY IN BIPOLAR MEMBRANE-CONTAINING REDOX FLOW BATTERY SYSTEMS

Amy S. Metlay

A DISSERTATION

in

Chemistry

Presented to the Faculties of the University of Pennsylvania

in

Partial Fulfillment of the Requirements for the

Degree of Doctor of Philosophy

2024

Supervisor of Dissertation

Dr. Thomas E. Mallouk

Vagelos Professor in Energy Research,

Professor of Chemistry, Department Chair

Co-Supervisor of Dissertation

Dr. Daniel J. Mindiola

Brush Family Professor of Chemistry

Graduate Group Chairperson

Dr. E. James Petersson

Professor of Chemistry, Chair of Graduate Studies, Professor of Biochemistry & Biophysics

Dissertation Committee

Dr. Neil Tomson	Associate Professor of Chemistry
Dr. Eric Detsi	Associate Professor of Materials Science and Engineering
Dr. Christopher Murray	Richard Perry University Professor of Chemistry and Materials Science and Engineering

To my family, friends, and loved ones. I am forever grateful for your lessons, love, and encouragement.

ACKNOWLEDGMENT

I am incredibly fortunate to have had so many people surrounding and supporting me throughout my experience in graduate school. I've enjoyed every moment thanks to their involvement.

I first want to thank my PhD advisors Tom Mallouk and Dan Mindiola for their support. I specifically want to thank my primary advisor, Tom, for his guidance, positivity, and patience. Tom has an innate ability to spark and nurture scientific wonder in any student. His constant nudge towards the fundamental questions has helped shape my scientific self. I can safely say I would not be the same scientist I am today without him. I next want to thank my labmates, past and current, for all their help and motivation. Our scientific discussions over lunch helped elucidate countless research problems I was facing. Above all else, I want to thank them for their sincere friendship. Even the most stressful research days were made easier with their laughter and kindness. Finally, I want to thank my friends, family, and other loved ones for allowing me to develop into the person I am today. I especially want to thank my grandma, mom, dad, sister, and partner, Baris, for all their unconditional love and unwavering belief in me.

ABSTRACT

INTERFACIAL CHEMISTRY IN BIPOLAR MEMBRANE-CONTAINING REDOX FLOW BATTERY SYSTEMS

Amy S. Metlay

Thomas E. Mallouk

Bipolar Membranes (BPMs) are a promising membrane technology that is currently being integrated into a variety of electrochemical energy conversion and storage devices. The acid-base redox flow battery utilizes a BPM to separate its anolyte and catholyte chambers. In the charged state of the redox flow battery, the anolyte is strongly acidic and the catholyte is strongly basic, adding a cross-membrane potential to the system of ~830 mV. A major benefit of all flow battery technologies is the separation of the reaction volume from the electrolyte tank, enabling individual optimization for capacity and power. However, this architecture results in several components and interactions that must be controlled before critical performance metrics can be met. A fundamental investigation of three such components is the primary topic of this dissertation.

Chapter 1 provides a brief review of currently studied BPM devices and systems as well as open questions for research. In chapter 2, the role of graphite oxide as a water dissociation catalyst in BPMs is investigated. The ideal GO catalytic loading density and orientation inside a BPM's interface as well as the movement of ions around individual GO nanosheets is discussed. Chapter 3 focuses on the entirety of the acid-base redox flow battery system, utilizing engineered design of a new three-chamber system to mitigate effects of membrane fouling and strict catholyte restrictions. Chapter 4 presents a study of the fundamental electrochemical processes that occur at a graphitic carbon electrode surface. Chemically functionalized graphitic electrodes with hydrophilic properties display higher values of capacity and faster heterogeneous charge transfer kinetics. Finally, in chapter 5, conclusions and outlooks derived from this dissertation are discussed.

A better understanding of these individual components – BPMs, engineered system design, and electrode kinetics – will allow for the optimization of the acid-base redox flow battery as well as the possible integration of fundamental discoveries from this research into other electrochemical systems that utilize at least one of these components.

TABLE OF CONTENTS

LIST OF TABLES

LIST OF FIGURES

LIST OF SCHEMES

CHAPTER 1: BIPOLAR MEMBRANES INCORPORATED INTO STANDARD ELECTROCHEMICAL DEVICES

Abstract

Bipolar membranes (BPMs) facilitate water association (forward bias) and water dissociation (reverse bias). When incorporated into an electrochemical device such as an aqueous redox flow battery, a BPM can maintain a beneficial pH gradient between the cell's anode and cathode. Other properties such as Donnan exclusion and proton/hydroxide production have led to the inclusion of BPMs in a wide variety of additional green technologies, including dialysis and CO_2 capture systems. Efficient incorporation of BPMs into such systems requires the optimization of the BPM through considerations that include water dissociation catalyst choices, membrane material choices, and a complete understanding of the membrane's interfacial interactions. Much research is currently underway to understand the fundamental science behind these systems and their subsequent optimization in practical applications.

Introduction

The global transition towards greener technologies has seen the incorporation of bipolar membranes (BPMs) into many electrochemical devices and systems.[1] The unique properties imposed on a system by the inclusion of a BPM help to alleviate certain shortcomings that monopolar membrane systems exhibit. As examples, in CO_2 capture from oceanwater, a BPM's ability to swing the pH of the anolyte and catholyte chambers of the device towards more acidic or alkaline values allows for manipulation of the CO_2 to bicarbonate equilibrium, increasing CO_2 solubility and separations.[2] In solar water splitting cells, a BPM can maintain different extreme pH environments on either reactive side of the membrane, allowing the hydrogen and oxygen evolution reactions (HER and OER) to take place under ideal pH

conditions.[3, 4] Fuel Cell BPM systems similarly benefit from ideal pH environments for their reactions while also utilizing water production and subsequent self-humidification from the BPM to alleviate common issues like electrode drying and cracking.[5, 6] Donnan exclusion principles help mitigate CO_2 electrolyzer shortcomings like product crossover.[7, 8] As a final detailed example, cross-membrane potentials from BPMs in redox flow battery (RFB) systems enable the construction of aqueous RFBs (ARFBs) with open circuit voltages (OCVs) far surpassing the electrochemical water-splitting window.[9, 10] Water electrolyzers,[11] desalination systems and other separation technologies[12, 13] are also well developed for BPM integration. Notably, to date, most systems integrated with a BPM operate in the reverse bias direction, but all directional uses still have research interest (Fig. 1.1). Such widespread utilization of BPMs requires a thorough understanding of their function in order to optimize their use.

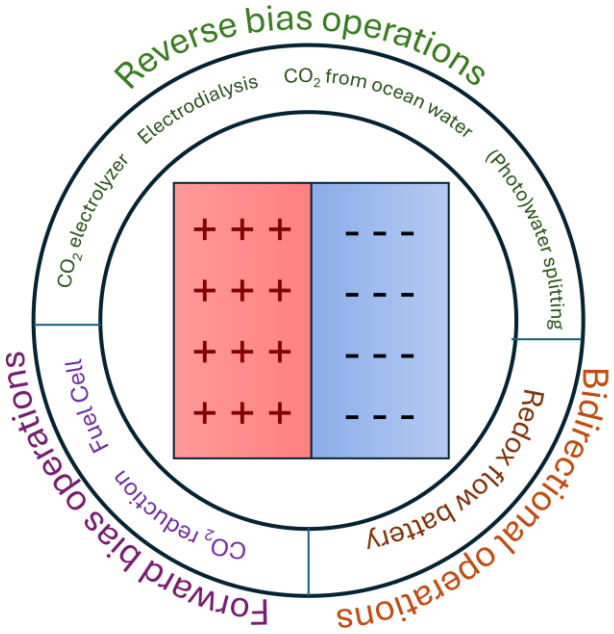

Figure 1.1. Established BPM technologies separated into their most common direction of use. Bidirectional use implies that both the forward and reverse bias directions are needed for the device's operation.

BPM Theory

A BPM is constructed by lamination of an anion-exchange layer (AEL) and a cation-exchange layer (CEL). At the AEL-CEL interface, upon lamination, mobile protons and hydroxides in the CEL and AEL respectively recombine, leaving behind the stationary charged headgroups of the AEL and CEL polymers in the so-called "space-charge region" (SCR). The electric field across the SCR results in a migratory force that is directly opposed to the diffusive force felt by the mobile ions, meaning that the AEL-CEL junction electrochemical potential solves to zero under equilibrium conditions (Fig. 1.2A).[14-16] Integration of a BPM into some devices results in two additional junctions and independent electric fields at the newly formed AEL-electrolyte and CEL-electrolyte interfaces.[17] These two interfaces can be solved for using the well-established Donnan potential.[18] Thus, a complete picture of a BPM at equilibrium results from the summation of the electrochemical potential differences across these three interfaces solving to the final form:

$$E_{mem} = \Delta pH \times 59 \text{ [mV/pH]}$$

In other words, for every difference of one pH unit across a BPM integrated into a device, 59 mV of cross-membrane potential is provided. As an example, if the CEL side of a BPM is in contact with 1 M hydrochloric acid and the AEL side of a BPM is in contact with 1 M potassium hydroxide (i.e. $\Delta pH = 14$), the cross-membrane potential of the system is ideally 830 mV at equilibrium. Alternatively, if both the CEL and AEL sides of a BPM are in contact with 1 M sodium chloride (i.e. $\Delta pH = 0$), the cross-membrane potential of the system is ideally 0 mV at equilibrium.[19]

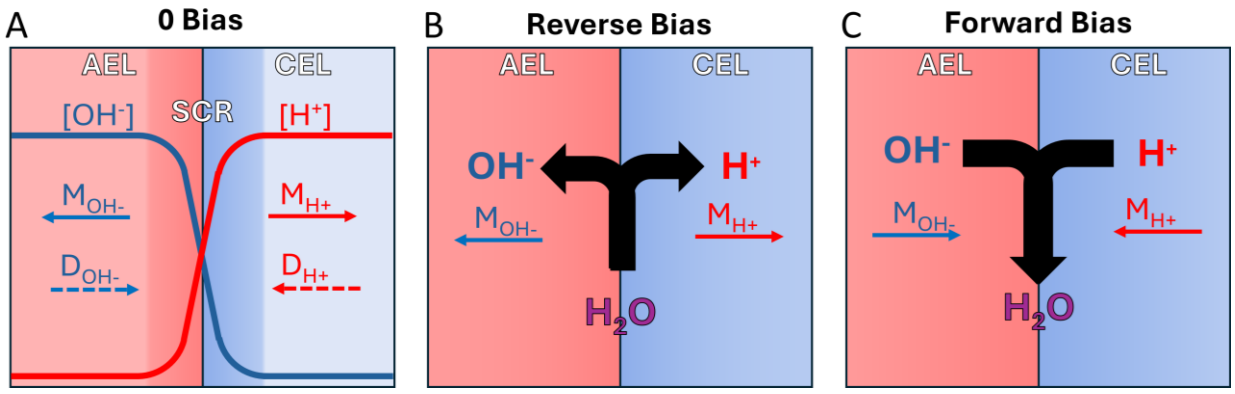

Figure 1.2. Graphical representation of BPMs operating in the (A) no bias or open circuit (OCV), (B) reverse bias, and (C) forward bias regimes. D_x (dashed arrow lines) represents diffusional movement of ions and M_x (solid arrow lines) represents migratory movement of ions.

The BPM system is further complicated when an external bias is applied, and things are shifted out of equilibrium.[1, 14, 15] A BPM is a current rectifier and can be moved from equilibrium in two different directions. Under forward-bias, assuming a ΔpH = 14, the applied electric field drives protons and hydroxide ions into the CEL and AEL respectively, where they meet at the AEL-CEL junction and react to form water. Co-ions (ions other than protons and hydroxides) can also transfer into the membrane system and ion pair with stationary ionic headgroups, which is an unproductive use of current (Fig. 1.2C).[20] Under a non-spontaneous reverse-bias, the applied electric field drives protons and hydroxide ions in the opposite direction, with the dissociation of water at the AEL-CEL junction supplying new proton and hydroxide ions through the water dissociation reaction (Fig. 1.2B). For practical use and integration into electrochemical devices, the kinetics of both directions of use in a BPM must be fast. Thus, a catalyst for water dissociation (and its reverse reaction) is typically included at the AEL-CEL junction to facilitate both forward and reverse bias directions.[21-23]

While not quantitatively understood, a combination of both electric field and catalytic effects is believed to play a role in a BPM's function.[24] The second Wein effect describes how an external electric field facilitates the dissociation of weak acids. Taking water to be a weak acid, a similar effect has been cited and solved for using Onsanger's theory for water dissociation in weak electrolytes.[22-26] Many numerical models have been developed to expand on Onsanger's theory and solve for BPM performance.[9, 21, 24, 26-28] However, the AEL and CEL are not weak electrolytes, and numerical models for transport and reactions in BPMs can be quite complex;[26] thus, the complete picture and ultimate role of the catalyst have yet to be fully elucidated. Importantly, numerical models developed without an Onsanger-like role for the electric field in water dissociation do not fit the experimental data well,[21] indicating that the electric field in a BPM must play some reactive role beyond simple migratory movement of ions upon catalytic dissociation.

Active Areas of BPM Research

The current state of BPM research can be broadly categorized into three areas – WD catalyst development, polymeric membrane material and architecture development, and device integration.

WD Catalyst Development

Development of WD catalysts spans various types of material research including organic materials like catalytically active polymers,[29] and inorganic materials like metal oxides.[21-23] Broadly, a good WD catalyst is believed to show some activity to HER, facilitate hydrogen-bonding, and display some O-H bond reorganization ability.[20]

Properties like conductivity, electron screening,[21] pka, and point of zero charge (pzc)[23] have all been investigated in a WD catalyst context. Oener et al. showed that metal oxide catalysts with acidic pzc

perform best in an architecture in which they are in contact with the proton producing CEL side of a BPM while, conversely, alkaline pzc metal oxides perform better on the AEL side of a BPM.[23] Chen et. al. showed that, for conducting metal oxide WD catalysts, an optimal loading density can be hundreds of nanometers thick due to what they theorize to be electronic screening of the electric field through the catalyst layer.[21]

Graphite oxide (GO) is a particularly interesting WD catalyst that has shown historically excellent performance in a BPM,[20, 28] but interestingly does not display some of the common properties found in good WD catalysts like partial electrical conductivity or a 3D geometry.[30, 31]

Membrane material development

The transport of reactive species (protons, hydroxides, water) into the reactive AEL-CEL interface is essential to the function of a BPM. As such, the development of polymeric materials with sufficiently high ionic conductivity is a critical area of research to push the onset of the mass transport limiting current during operations.[32, 33]

Additionally, structural integrity[34] and strong adhesion at the AEL-CEL junction in a BPM is required. Delamination, particularly due to ballooning from water formation during forward bias operations, plagues many BPM technologies. Architecturally unique membrane structures like fibrous electrospun junctions[35] and lithographically created pillars[36] in the AEL-CEL junction have been constructed to limit delamination processes. Unique polymeric materials with similar, more adhesive backbones have also been investigated for their role in mitigating delamination.[37]

Device integration

The ultimate motivation of BPM development is integration into devices.[1, 16] As mentioned above, many BPM devices are currently under development, but most remain far from wide commercialization. Factors like reaction overpotential, material cost, and reaction kinetics must all substantially improve before sufficient reaction current densities can be reached. A particularly interesting BPM device is the acid-base redox flow battery developed by the Mallouk group.[9, 10] As redox flow batteries undergo both charge and discharge processes, the acid-base redox flow battery is one of the few BPM-integrated technologies in which both the forward and reverse bias modes are utilized and thus must be well understood. An exemplary version of this system utilizes a viologen in acidic conditions as an anolyte and ferrocyanide in alkaline conditions as a catholyte, reaching an OCV of 1.6 V (Fig. 1.3).

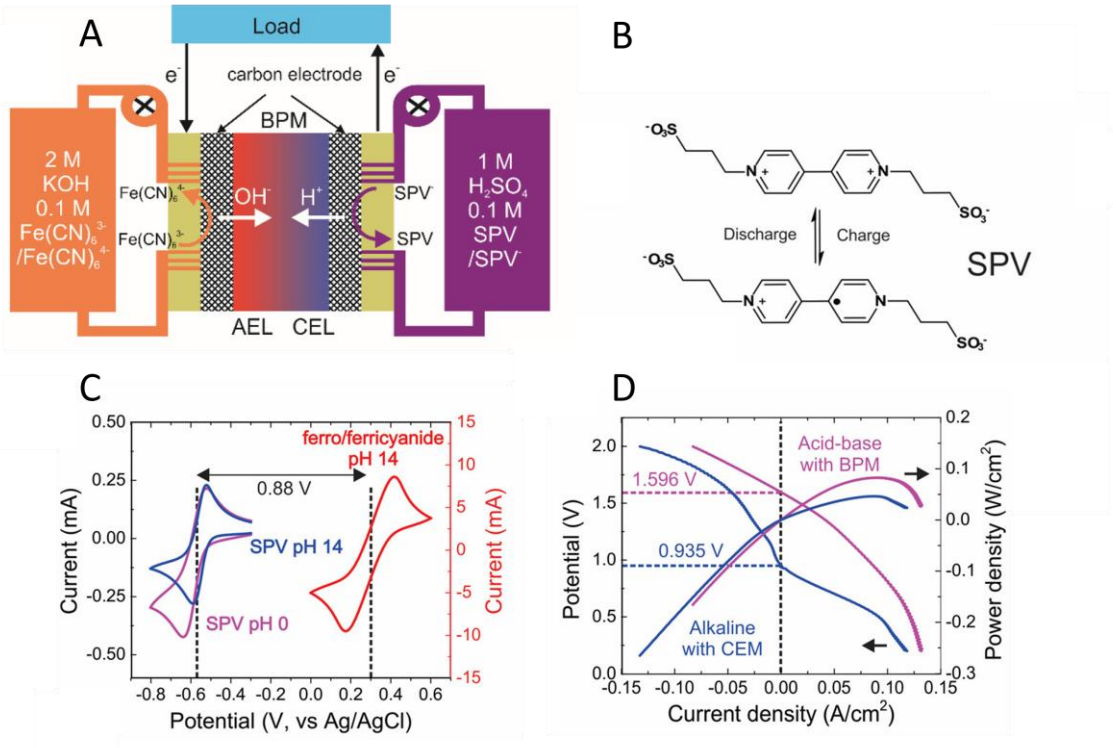

Figure 1.3. (A) Graphical representation of the acid-base redox flow battery operating under a forward bias. (B) Structural drawing of the anolyte (SPV) changing charge states. The catholyte (ferro/ferricyanide) is a simple cyanide coordinated iron species that undergoes an Fe(II)/Fe(III) transition. (C) Cyclic voltammograms of the expected $E_{1/2}$ difference and thus OCV of the representative redox flow battery if no cross-membrane potential is considered. (D) Polarization curves of the redox flow battery system with (purple) and without (blue) a BPM. Figure reproduced[9] following CC guidelines, copyright 2021, American Chemical Society.

Aqueous Redox Flow Batteries

ARFBs offer many benefits over their non-aqueous counterparts including increased safety, less expensive costs, improved conductivity and transport numbers, and more advanced membrane technologies.[38-40] Vanadium ARFBs represent some of the most advanced flow battery technologies, with actual commercialization having been reached.[41] All-iron flow batteries are a younger commercialized system, offering the benefit of less expensive materials.[42]

A major limitation of ARFBs is the relatively narrow water electrochemical stability window, which is nominally 1.23V but can approach ~2 V in certain aqueous media because of electrode overpotentials for hydrogen and oxygen evolution. While organic solvents such as acetonitrile can have an electrochemical stability window of up to 6.1 V[43] and thus have a wide range of redox species with vastly different electropotentials to select from, the range of possible electropotentials for ARFBs is far more limited.[39] When an ARFB is pushed far beyond 1.23 V, unwanted side reactions like HER and OER can set in, leading to poor faradaic efficiencies. The utilization of electrode materials such as graphite with slow kinetics and high overpotentials to HER and OER can expand this window, but they come with their own set of considerations such as slow kinetics for the reactions of interest in the ARFB and low capacitance.[44, 45]

As such, the inclusion of a BPM into an ARFB offers a unique work-around from which additional potential can be added to a cell's OCV independent of the selected anolyte and catholyte redox species.[9] Simple, abundant, and non-designer redox species can be readily incorporated into the ARFB system and upon the inclusion of a BPM, ARFBs with OCVs as high as 1.7 V have been obtained.[10]

However, this so-called "acid-base redox flow battery" remains far from optimized. As with all BPM devices, there exists a large development space for BPM improvements. In particular, in addition to typical factors like series resistance and charge transfer, the IR-drop of an acid-base redox flow battery is dependent on the overpotentials of water association and dissociation, meaning that BPM overpotentials must be minimized to get sufficient values of energy efficiency.[9] Additionally, a standard two-chamber system design of the acid-base redox flow battery is plagued by membrane fouling and poor faradaic efficiencies. Unique engineered system designs like a three-chamber cell have been developed to mitigate poor faradaic efficiencies but still leave space for continued development.[10] Finally, as acid-base redox flow batteries reach strikingly high OCVs, electrode materials such as graphite with slow kinetics and high overpotential to HER and OER must be utilized. However, carbon electrodes are historically plagued by slow heterogenous charge-transfer kinetics and low capacitance due to seemingly unavoidable contamination with adventitious hydrocarbons. Approaches to mitigate this contamination include laser ablation,[44, 45] thermal treatments,[46] and chemical functionalization.

Conclusion

Much BPM development is currently geared towards eventual integration into electrochemical devices and systems. For these systems to reach promising performance levels, BPM catalysts, membrane materials, and membrane architecture must all be optimized, and for this optimization to occur, a more fundamental understanding of a BPM's function is required. For example, the complete contributions

and interactions between internal electric fields and catalytic activity must be deconvoluted through first-principles theory, which can provide guidance for both numerical modeling and experimentation. Much ongoing research is aimed at achieving a better understanding of this interaction.

References

(1) Blommaert, M. A.; Aili, D.; Tufa, R. A.; Li, Q. F.; Smith, W. A.; Vermaas, D. A. Insights and Challenges for Applying Bipolar Membranes in Advanced Electrochemical Energy Systems. *ACS Energy Lett.* **2021**, *6* (7), 2539-2548.

(2) Digdaya, I. A.; Sullivan, I.; Lin, M.; Han, L. H.; Cheng, W. H.; Atwater, H. A.; Xiang, C. X. A direct coupled electrochemical system for capture and conversion of CO_2 from oceanwater. *Nat. Commun.* **2020**, *11* (1).

(3) Luo, J. S.; Vermaas, D. A.; Bi, D. Q.; Hagfeldt, A.; Smith, W. A.; Grätzel, M. Bipolar Membrane-Assisted Solar Water Splitting in Optimal pH. *Adv. Energy Mater.* **2016**, *6* (13).

(4) Vermaas, D. A.; Sassenburg, M.; Smith, W. A. Photo-assisted water splitting with bipolar membrane induced pH gradients for practical solar fuel devices. *J. Mater. Chem. A.* **2015**, *3* (38), 19556-19562.

(5) Ünlü, M.; Zhou, J. F.; Kohl, P. A. Hybrid Anion and Proton Exchange Membrane Fuel Cells. *J. Phys. Chem. C.* **2009**, *113* (26), 11416-11423.

(6) Ünlü, M.; Zhou, J. F.; Kohl, P. A. Hybrid Polymer Electrolyte Fuel Cells: Alkaline Electrodes with Proton Conducting Membrane. *Angew. Chem. Int. Ed.* **2010**, *49* (7), 1299-1301.

(7) Yan, Z. F.; Hitt, J. L.; Zeng, Z. C.; Hickner, M. A.; Mallouk, T. E. Improving the efficiency of CO2 electrolysis by using a bipolar membrane with a weak-acid cation exchange layer. *Nat. Chem.* **2021**, *13* (1), 33.

(8) Xie, K.; Miao, R. K.; Ozden, A.; Liu, S. J.; Chen, Z.; Dinh, C. T.; Huang, J. E.; Xu, Q. C.; Gabardo, C. M.; Lee, G.; et al. Bipolar membrane electrolyzers enable high single-pass CO_2 electroreduction to multicarbon products. *Nat. Commun.* **2022**, *13* (1).

(9) Yan, Z. F.; Wycisk, R. J.; Metlay, A. S.; Xiao, L. Q.; Yoon, Y.; Pintauro, P. N.; Mallouk, T. E. High-Voltage Aqueous Redox Flow Batteries Enabled by Catalyzed Water Dissociation and Acid-Base Neutralization in Bipolar Membranes. *ACS Cent. Sci.* **2021**, *7* (6), 1028-1035.

(10) Metlay , A. S.; Chyi , B.; Yoon , Y.; Wycisk , R. J.; Pintauro , P. N.; Mallouk, T. E. Three-Chamber Design for Aqueous Acid-Base Redox Flow Batteries. *ACS Energy Lett.* **2022**, 7 (3), 908-913.

(11) Mayerhöfer, B.; McLaughlin, D.; Böhm, T.; Hegelheimer, M.; Seeberger, D.; Thiele, S. Bipolar Membrane Electrode Assemblies for Water Electrolysis. *ACS Appl. Energy Mater.* **2020**, *3* (10), 9635-9644.

(12) Chen, T. Y.; Bi, J. T.; Ji, Z. Y.; Yuan, J. S.; Zhao, Y. Y. Application of bipolar membrane electrodialysis for simultaneous recovery of high-value acid/alkali from saline wastewater: An in-depth review. *Water Res.* **2022**, *226,* 119274.

(13) Wilhelm, F. G.; Pünt, I.; van der Vegt, N. F. A.; Strathmann, H.; Wessling, M. Asymmetric bipolar membranes in acid-base electrodialysis. *Ind. Eng. Chem. Res.* **2002**, *41* (3), 579-586.

(14) Parnamae, R.; Mareev, S.; Nikonenko, V.; Melnikov, S.; Sheldeshov, N.; Zabolotskii, V.; Hamelers, H. V. M.; Tedesco, M. Bipolar membranes: A review on principles, latest developments, and applications. *J. Membr. Sci.* **2021**, *617*.

(15) Giesbrecht, P. K.; Freund, M. S. Recent Advances in Bipolar Membrane Design and Applications. *Chem. Mater.* **2020**, *32* (19), 8060-8090.

(16) Yan, Z. F.; Mallouk, T. E. Bipolar Membranes for Ion Management in (Photo)Electrochemical Energy Conversion. *Acc. Mater. Res.* **2021**, *2* (12), 1156-1166.

(17) Blommaert, M. A.; Vermaas, D. A.; Izelaar, B.; Veen, B.; Smith, W. A. Electrochemical impedance spectroscopy as a performance indicator of water dissociation in bipolar membranes. *J. Mater. Chem. A.* **2019**, *7* (32), 19060-19069.

(18) Donnan, F. G. Theory of membrane equilibria and membrane-potentials in the presence of non-dialyzing electrolytes. *J. Membr. Sci.* **1995**, *100* (1), 45-55.

(19) Vermaas, D. A.; Wiegman, S.; Nagaki, T.; Smith, W. A. Ion transport mechanisms in bipolar membranes for (photo)electrochemical water splitting. *Sus. Energy Fuels* **2018**, *2* (9), 2006-2015.

(20) McDonald, M. B.; Freund, M. S. Graphene Oxide as a Water Dissociation Catalyst in the Bipolar Membrane Interfacial Layer. *ACS Appl. Mater. Interfaces* **2014**, *6* (16), 13790-13797.

(21) Chen, L. H. K.; Xu, Q. C.; Oener, S. Z.; Fabrizio, K.; Boettcher, S. W. Design principles for water dissociation catalysts in high-performance bipolar membranes. *Nat. Commun.* **2022**, *13* (1).

(22) Chen, L. H. K.; Xu, Q. C.; Boettcher, S. W. Kinetics and mechanism of heterogeneous voltage-driven water-dissociation catalysis. *Joule* **2023**, *7* (8), 1867-1886.

(23) Oener, S. Z.; Foster, M. J.; Boettcher, S. W. Accelerating water dissociation in bipolar membranes and for electrocatalysis. *Science* **2020**, *369* (6507), 1099.

(24) Yan, Z. F.; Zhu, L.; Li, Y. G. C.; Wycisk, R. J.; Pintauro, P. N.; Hickner, M. A.; Mallouk, T. E. The balance of electric field and interfacial catalysis in promoting water dissociation in bipolar membranes. *Environ. Sci.* **2018**, *11* (8), 2235-2245.

(25) Oener, S. Z.; Twight, L. P.; Lindquist, G. A.; Boettcher, S. W. Thin Cation-Exchange Layers Enable High-Current-Density Bipolar Membrane Electrolyzers via Improved Water Transport. *ACS Energy Lett.* **2021**, *6* (1), 1-8.

(26) Bui, J. C.; Corpus, K. R. M.; Bell, A. T.; Weber, A. Z. On the Nature of Field-Enhanced Water Dissociation in Bipolar Membranes. *J. Phys. Chem. C.* **2021**, *125* (45), 24974-24987.

(27) Bui, J. C.; Lucas, E.; Lees, E. W.; Liu, A. K.; Atwater, H. A.; Xiang, C. X.; Bell, A. T.; Weber, A. Z. Analysis of bipolar membranes for electrochemical CO_2 capture from air and oceanwater. *Energy Environ. Sci.* **2023**, *16* (11), 5076-5095.

(28) Lucas, E.; Bui, J.; Hwang, M.; Wang, K.; Bell, A.; Weber, A.; Ardo, S.; Atwater, H.; Xiang, C. Asymmetric bipolar membrane for high current density electrodialysis operation with exceptional stability. Preprint at C*hemRxiv*, 2023.

(29) Schulte, L.; White, W.; Renna, L. A.; Ardo, S. Turning water into a protonic diode and solar cell via doping and dye sensitization. *Joule* **2021**, *5* (9), 2380-2394.

(30) Kovtyukhova, N. I.; Ollivier, P. J.; Martin, B. R.; Mallouk, T. E.; Chizhik, S. A.; Buzaneva, E. V.; Gorchinskiy, A. D. Layer-by-layer assembly of ultrathin composite films from micron-sized graphite oxide sheets and polycations. *Chem. Mater.* **1999**, *11* (3), 771-778.

(31) Lerf, A.; He, H. Y.; Forster, M.; Klinowski, J. Structure of graphite oxide revisited. *J. Phys. Chem. B.* **1998**, *102* (23), 4477-4482.

(32) Luo, T.; Abdu, S.; Wessling, M. Selectivity of ion exchange membranes: A review. *J. membr. Sci.* **2018**, *555*, 429-454.

(33) De Porcellinis, D.; Mecheri, B.; D'Epifanio, A.; Licoccia, S.; Granados-Focil, S.; Aziz, M. J. Communication-Sulfonated Poly (ether ether ketone) as Cation Exchange Membrane for Alkaline Redox Flow Batteries. *J. Eletrochem. Soc.* **2018**, *165* (5), A1137-A1139.

(34) Pan, J.; Zhu, L.; Han, J. J.; Hickner, M. A. Mechanically Tough and Chemically Stable Anion Exchange Membranes from Rigid-Flexible Semi-Interpenetrating Networks. *Chem. Mater.* **2015**, *27* (19), 6689-6698.

(35) Shen, C. H.; Wycisk, R.; Pintauro, P. N. High performance electrospun bipolar membrane with a 3D junction. *Energy Environ. Sci.* **2017**, *10* (6), 1435-1442.

(36) Kole, S.; Venugopalan, G.; Bhattacharya, D.; Zhang, L.; Cheng, J.; Pivovar, B.; Arges, C. G. Bipolar membrane polarization behavior with systematically varied interfacial areas in the junction region. *J. Mater. Chem. A.* **2021**, *9* (4), 2223-2238.

(37) Kao, Y. L.; Chen, L. H. K.; Boettcher, S. W.; Aili, D. Divergent Synthesis of Bipolar Membranes Combining Strong Interfacial Adhesion and High-Rate Capability. *ACS Energy Lett.* **2024**.

(38) Winsberg, J.; Hagemann, T.; Janoschka, T.; Hager, M. D.; Schubert, U. S. Redox-Flow Batteries: From Metals to Organic Redox-Active Materials. *Angew. Chem. Int. Ed.* **2017**, *56* (3), 686-711.

(39) Chen, H. N.; Cong, G. T.; Lu, Y. C. Recent progress in organic redox flow batteries: Active materials, electrolytes and membranes. *J. Energy Chem.* **2018**, *27* (5), 1304-1325.

(40) Arenas, L. F.; de Leon, C. P.; Walsh, F. C. Redox flow batteries for energy storage: their promise, achievements and challenges. *Curr. Opin. Electrochem.* **2019**, *16*, 117-126.

(41) Park, M.; Ryu, J.; Wang, W.; Cho, J. Material design and engineering of next-generation flow-battery technologies. *Nat. Rev. Mater.* **2017**, *2* (1), 18.

(42) Hawthorne, K. L.; Wainright, J. S.; Savinell, R. F. Studies of Iron-Ligan Complexes for an All-Iron Flow Battery Application. *J. Electrochem. Soc.* **2014**, *161* (10), A1662.

(43) Gong, K.; Fang, Q. R.; Gu, S.; Li, S. F. Y.; Yan, Y. S. Nonaqueous redox-flow batteries: organic solvents, supporting electrolytes, and redox pairs. *Energy Environ. Sci.* **2015**, *8* (12), 3515-3530.

(44) Poon, M.; McCreery, R. L.; Engstrom, R. Laser Activation of Carbon Electrodes – Relationship Between Laser-Induced Surface Effects and Electron-Transfer Activation. *Anal. Chem.* **1988**, *60* (17), 1725-1730.

(45) Kozbial, A.; Zhou, F.; Li, Z. T.; Liu, H. T.; Li, L. Are Graphitic Surfaces Hydrophobic? *Acc. Chem. Res.* **2016**, *49* (12), 2765-2773.

(46) Yue, L.; Li, W. S.; Sun, F. Q.; Zhao, L. Z.; Xing, L. D. Highly hydroxylated carbon fibres as electrode materials of all-vanadium redox flow battery. *Carbon* **2010**, *48* (11), 3079-3090.

CHAPTER 2: LANGMUIR-BLODGETT DEPOSITION OF GRAPHITE OXIDE NANOSHEETS AS CATALYSTS FOR BIPOLAR MEMBRANE ELECTROCHEMISTRY

Abstract

Graphite oxide (GO) has been widely studied as an interfacial layer in bipolar membranes because of its activity as a catalyst for the water dissociation and acid-base neutralization reactions. However, the roles of GO nanosheet size, orientation, and surface coverage in controlling its catalytic activity are not well understood. GO nanosheets with lateral dimensions of several microns were prepared by oxidative exfoliation of natural graphite crystals, enabling their orientation and coverage to be observed directly by optical microscopy. The coverage and orientation of the GO nanosheets were measured as a function of different deposition methods, which included solution adsorption, Langmuir Blodgett transfer from an air-water interface, and spray-coating. Highly oriented GO films made by the Langmuir Blodgett method gave the best performance metrics. Interestingly, full coverage of the bipolar interface by GO nanosheets resulted in lower performance than partial coverage. This effect could be rationalized in terms of the differential permeability of H^+ and OH^- ions through GO, which leads to concentration polarization of OH^- on one side of the sheets.

Introduction

Bipolar membranes (BPMs) are ionomeric structures in which anion- and cation-exchange layers (AEL and CEL, respectively) are laminated together. Under reverse bias conditions, water dissociation occurs in the membrane junction and H^+ and OH^- ions are driven outward through the CEL and AEL layers, respectively. In forward bias the reverse process occurs, resulting in water formation in the junction. Because the water dissociation reaction is endoergic, the current-voltage curve of a BPM is asymmetric

and “diode-like”.[1-4] Donnan exclusion and current rectification in BPMs enables them to maintain or swing the pH on the two sides of an electrochemical cell and minimize molecule and ion crossover in reverse bias. These unique features of BPMs have led to their incorporation into a growing number of electrochemical systems. Originally developed for electrodialysis, BPMs have now been studied for applications that include solar-driven water electrolysis,[5] fuel cells,[6, 7] CO_2 capture from ocean water,[8, 9] CO_2 electrolysis,[10] and aqueous redox-flow batteries.[11, 12]

Concurrent with these practical developments, fundamental research has been carried out to understand the interplay between catalytic and electric field effects in driving the water dissociation and acid-base neutralization in BPMs.[13-16] Because uncatalyzed water dissociation (WD) is a kinetically slow process, a catalyst layer is needed at the bipolar interface to facilitate current flow in either direction.[4,11] While simple models of BPM catalysis are adequate to fit the major features of BPM polarization behavior,[11] they do not explain quantitatively how factors such as the thickness, acidity/basicity, and electronic conductivity of catalyst layer affect their performance.[15-21]

Recent experiments by Boettcher and coworkers have deconvoluted relationships between catalyst electronic conductivity, deposition thickness, and electron mobility for a variety of nanoparticulate metal oxide catalysts. They correlated the catalyst point of zero charge (PZC) with activity on the AEL or CEL side of the membrane.[17] Interestingly, they found that forward and reverse bias catalysis are optimized by using different materials and different catalyst layer thicknesses. Several research groups have also studied “3D” and interdigitated junction structures as a means of increasing catalytic surface area.[19, 22] While these structures enhance the performance of the BPM considerably, they further complicate the task of modeling the catalytic interface.

BPM catalysts are often modeled as continuum phases because the dimensions of the catalyst nanoparticles are typically small compared to the thickness of the catalyst layer. Graphite oxide (GO), which has been studied as a BPM WD catalyst both experimentally and computationally,[13, 20, 23, 24] is an exception because the individual sheets have sub-nanometer thickness but often micron-scale lateral dimensions. They can be deposited in the junction as monolayers, partial monolayers, or multilayers. An earlier study from our group showed how multiple iterations of layer-by-layer GO assembly onto an AEL could improve the electrochemical performance of a BPM.[13] While the thickness of the catalytic layers was not directly quantified, more complete catalytic surface coverage was hypothesized as the reason for enhanced performance. Earlier work by Freund et al. used spin-coating to create interfacial GO layers of varying thicknesses to determine an optimal loading density.[20]

In this study, GO nanosheets with lateral dimensions of several microns were prepared by oxidative exfoliation of natural graphite crystals. The large size and optical contrast of the GO sheets enabled their orientation and coverage on the AEL to be observed directly by optical microscopy. The coverage and orientation of the GO nanosheets in BPMs made from these modified AELs were measured as a function of different deposition methods, which included solution adsorption (SA) of anionic GO sheets onto the cationic AEM surface, Langmuir Blodgett (LB) transfer from an air-water interface, and spray-coating. Interestingly, partial monolayer coverages of GO grown by the LB method had substantially better performance in BPMs than complete monolayers or multilayers. Numerical models and electrochemical measurements of differential H^+ and OH^- migration through GO layers help to elucidate the mechanism of ion transport through GO-rich BPM catalyst junctions and explain qualitatively the optimum performance of partial monolayer GO catalysts.

Results and Discussion

GO synthesis, deposition, and reverse bias catalysis. Consistency in the synthesis of GO is challenging to achieve and predict via spectroscopic methods (Raman and IR) and X-ray powder diffraction. Batches of GO derived from different sources of graphite that appear similar spectroscopically (Fig. 2.6) can have very different overpotential characteristics in BPMs when they are made by SA deposition (Fig. 2.7). Similarly, while optical images of catalyst coverages appear similar, replicability in performance from deposition techniques such as spray coating, which leaves a randomly oriented catalyst layer, is poor in comparison to SA and LB deposition (Fig 2.8, 2.9). However, within a single batch of GO, the results obtained with multiple membranes by a given deposition technique (SA or LB) were highly reproducible (Fig. 2.9). Consequently, all comparisons were made with a single standard batch of GO.

Natural graphite crystals were oxidized following a previously reported procedure to yield fully exfoliated GO suspensions.[25] The large lateral size of these GO nanosheets enables straightforward optical imaging down to very low coverage of exfoliated GO sheets. Remarkably fine details such as edge shape and the presence of wrinkles can be identified (Fig. 2.10). A comparison of optical images taken after SA, LB, and spray coating of these large GO sheets onto a Fumasep AEL enables analysis of their coverage and orientation (Fig. 2.1).

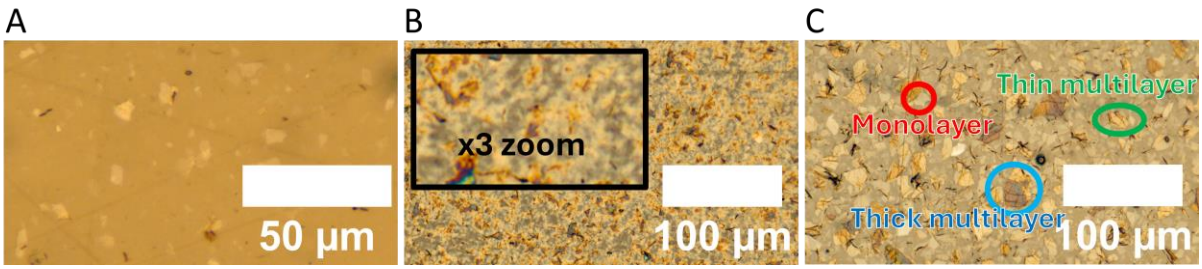

Figure 2.1. Optical microscope images of GO deposited on a Fumasep AEL using (A) SA, (B) spray coating with a 3x magnified inset, and (C) LB deposition techniques. An expanded view inset in (B) shows the chaotic orientation of GO sheets deposited by spray coating. Regions of monolayer, thin multilayer, and thick multilayer LB deposition are highlighted in (C).

With spray deposition, individual GO nanosheets cannot be differentiated as they are folded and stacked on top of each other, forming regions of dense coverage (Fig. 2.1B). With SA deposition, the sheets appear to be fully exfoliated and sparsely dispersed but with similar optical contrast indicating a uniform orientation (Fig. 2.1A). With LB deposition, depending on the chosen level of coverage (Table 2.2), we observe oriented single layers and multilayers of GO sheets at varying degrees of coverage (Fig. 2.1C). Importantly, the degree of coverage can be controlled using the LB method through the dip number and the initial volume of GO suspension added to the LB trough (Table 2.2).

The coverage of the highly oriented deposition techniques (SA and/or LB) was quantified through a thresholding method (see SI). To test the method's accuracy and leverage the predictive power that quantification of oriented GO coverage provides, the electrochemical performance of two different synthetic batches of GO incorporated into BPMs was compared (Fig. 2.11). Modulating the coverage of the two batches via LB deposition to match resulted in nearly identical overpotential performance (Fig. 2.11D), indicating that if the coverage of oriented GO nanosheets can be quantified, the electrochemical

performance can be predicted. As such, a comparison of BPM performance metrics under different orientation types and degrees of coverage was possible.

Freund, et al. have used reverse-bias overpotential and permselectivity as performance metrics to compare GO-containing BPMs made by spin coating at different levels of GO coverage.[20] They found that, generally, higher GO loading led to lower overpotential but poorer permselectivity. To investigate how these performance trends varied with deposition technique, permselectivity and overpotential data were compared for one batch of GO at high coverage using spray coating and LB methods (Fig. 2.2A, 2.12A). In the permselectivity measurements, the highly oriented nanosheets deposited by the LB method passed less current in the co-ion leakage portion of the j-E-curve,[2] and thus performed better than the more randomly oriented multilayer deposited by spray coating. In the overpotential comparison (Fig. 2.2B, 2.12B), the spray coating and LB methods gave comparable results, and both were dramatically superior to samples with no catalyst, underscoring the importance of the catalytic layer.

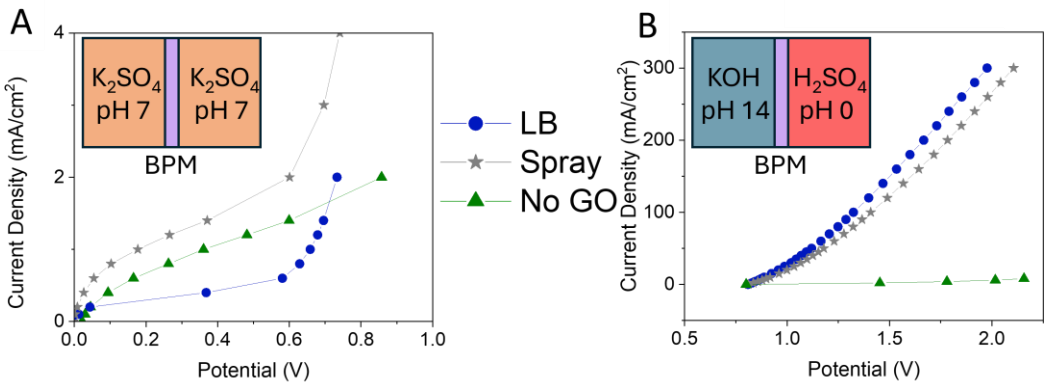

Figure 2.2. Reverse bias j-E curves in the (A) low current co-ion leakage region and (B) high current overpotential region for BPMs catalyzed by GO deposited by spray and LB methods. In (A), measurements were made with neutral K_2SO_4 solutions on both sides of the membrane, whereas in (B), strongly basic and strongly acidic solutions were used on the CEL and AEL sides of the membrane, respectively.

Highly oriented GO layers made by LB and SA deposition on Fumasep AEMs showed an interesting and non-monotonic trend in surface coverage vs. overpotential in the resulting BPMs (Fig. 2.3). Statistical analysis of the microscope images showed that at low coverage SA layers were more evenly distributed on the AEM surface than LB layers. In these cases, SA deposition (5 ± 2%) gave higher current density at a given overpotential than LB (7 ± 4%), presumably because larger areas in the LB sample were not covered by catalyst and were therefore non-catalytic for water dissociation. In other words, at low coverage SA deposition leads to a more uniform distribution of GO nanosheet coverage, and therefore more efficient catalysis, than LB deposition. Increasing the coverage of the LB samples to 50-60% gave the highest performing membranes. Curiously, higher LB coverage (~ 100%) gave significantly poorer performance. Similar trends were found with higher performing AEL materials such as Piperion (Fig. 2.13), but quantification of GO coverage on those materials was more difficult due to the low contrast between GO nanosheets and the Piperion membrane.

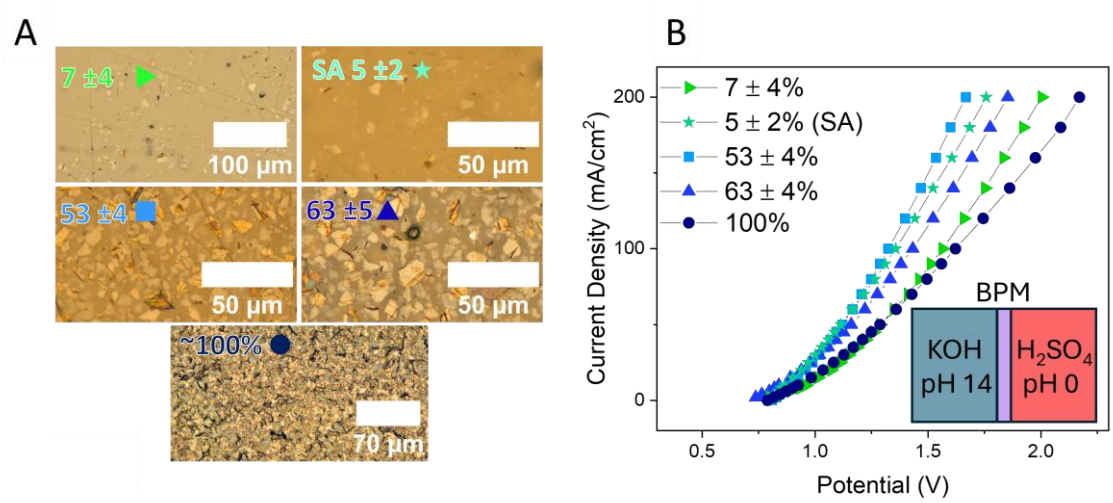

Figure 2.3. (A) Optical images of GO deposited on a Fumasep AEL at different LB and SA loadings (see Table 2.2 for details). Percent coverage was calculated as the average of three different regions of the image. (B) Overpotential j-E curves of BPMs containing the various LB interfacial GO regions.

H^+ and OH^- conduction through catalytic GO layers. The lower performance found with nearly complete monolayers of GO made by LB deposition is likely due to mass transport effects, since these samples contain more catalyst than low coverage, higher performing samples. One possible mechanism for the loss in activity is recombination of catalytically generated H^+ and OH^- if one or both of these ions must migrate around (rather than through) the GO nanosheets (Fig. 2.4). This possibility was tested experimentally by sandwiching GO layers between cation or anion exchange membranes. Membranes made by laminating two CELs together show little difference in proton conductivity with or without an oriented GO layer at the membrane interface. In contrast, membranes made by laminating two AELs together show a difference in hydroxide conductivity when an oriented GO layer is present (Fig. 2.4A). This suggests that transport of solvated H^+ ions through the GO sheets is relatively fast, but transport of OH^- ions is measurably slower. Because GO contains ionizable groups that impart a negative surface charge,[24] it is not unreasonable to expect that they preferentially transport protons.

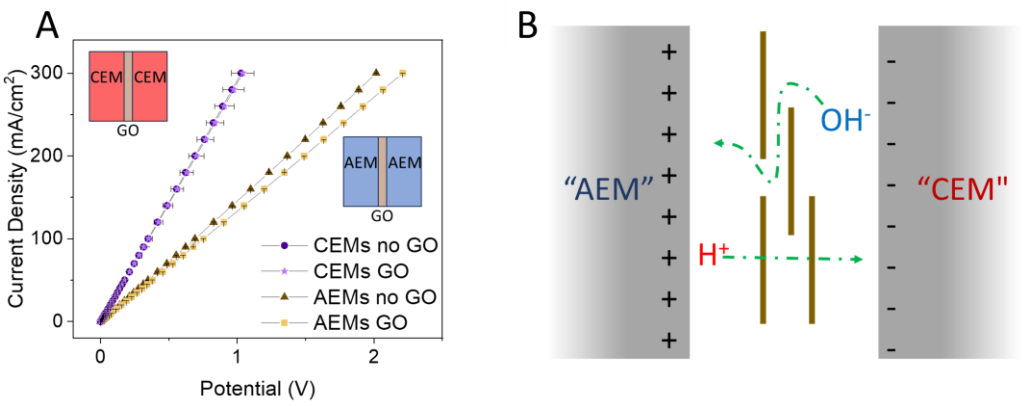

Figure 2.4. (A) Ionic conductivity of dense layers of GO nanosheets. (B) Cartoon depiction of electric field-driven migration of H^+ and OH^- ions through or around a GO nanosheet in a reverse-bias BPM. Hydroxide ions follow a more tortuous path than protons, leading to a locally higher concentration of ions and $H^+ + OH^-$ recombination on the CEL side of the membrane.

Numerical modeling of water dissociation and transport in BPMs. Because of the very different length scales of the electrical double layers (1-2 nm) and the lateral dimensions of GO nanosheets used in this study (µm), a numerical model of a 2D BPM that embodied both ionic movement through and around an oriented GO catalyst layer, as well as catalytic water dissociation and $H^+ + OH^-$ recombination, was nontrivial. Consequently, two simplified numerical multiphysics models were constructed to explore the picture illustrated in Fig. 2.4B. A 1D model of a BPM adapted from a previous study[11] (Fig. 2.14) showed an increase in water dissociation overpotential as ionic diffusion through the catalytic region was made asymmetric, with the OH^- and H^+ conductivities in the catalyst region differing by a factor of 10 (Fig. 2.5A). This model utilized the parameters from a previously published study.[11] A second simplified model calculated ion transport and water dissociation/$H^+ + OH^-$ recombination rates on two sides of a catalytically active GO monolayer in a tank of pH neutral water under an applied electric field (Fig. 2.15). This simplified model showed an increase in the rate of water formation at the surface of the GO

nanosheet facing the negative direction (analogous to the CEL in the BPM) of the applied electric field (Fig. 2.5B). Notably, while the H^+ + OH^- recombination rate is relatively constant along the entirety of the nanosheet surface in the model, the rate is lower near the edge of the GO sheet where the local concentration of OH^- is lower. This suggests that smaller nanosheets or less densely packed interfaces could provide a higher net reaction rate for generation and separation of H^+ and OH^- ions. Details of the numerical models are described more fully in the SI.

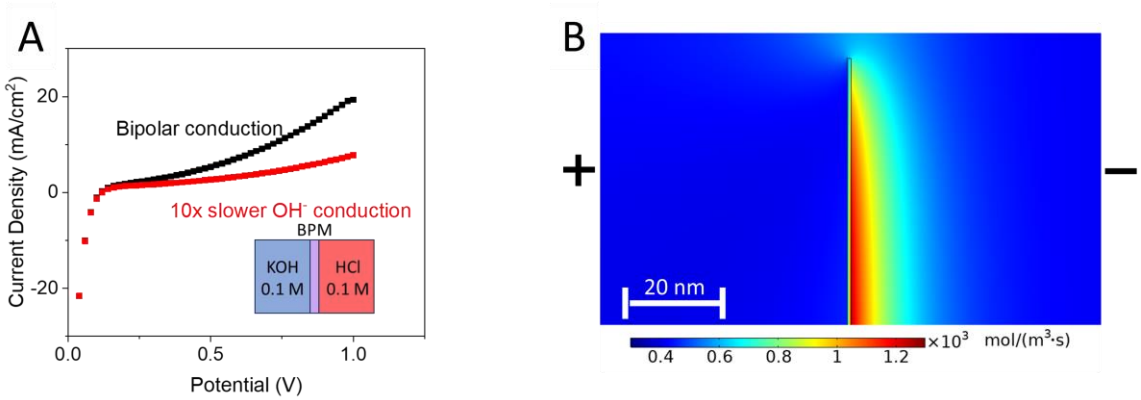

Figure 2.5. Numerical models depicting (A) the j-E-curve of a BPM with bipolar ionic GO conductivity (black), and slow GO conductivity towards hydroxide ions (red). See SI for full details on the parameters used in this model. (B) Asymmetrical and increased (red) water formation rates around a catalytically active GO nanosheet made ten times less conductive towards hydroxide ions than protons.

Conclusion

Optical microscopy of large GO nanosheets (~10 µm lateral dimensions) was used to correlate BPM electrochemical performance with GO deposition method and coverage. Oriented deposition techniques (LB and SA) gave improved permselectivity and overpotential performance. Increasing the areal coverage by LB deposition gave improved overpotential up to ~50% coverage, but interestingly, at full monolayer coverage the overpotential increased, suggesting a competition between catalysis and ion

recombination rates, likely because the transport of OH^- ions through the negatively charged GO sheets is slow.

Supporting Information

Materials

All chemicals were purchased from ThermoFisher Scientfic and used as received unless otherwise noted. Anion exchange membranes (Fumasep-30 and PiperION 20 μm) were purchased from the Fuel Cell Store. Platinum wires (0.5 mm diameter, 99.95%) were purchased from Alfa Aesar. Ag/AgCl reference electrodes with 3 M NaCl filling solution were purchased from Microelectrode. The peristaltic pump was purchased from MasterFlex (Cole-Parmer, No. 7553-80).

Graphite oxide (GO) was synthesized from specified graphite sources (325 mesh, GAK-2, Ukraine or 50 mesh, Aldrich see Table 2.1) following a previously reported method.[25] Graphite Oxide paste was purchased from Graphene Laboratories Inc and diluted as previously detailed before use.[27] Nafion 117 dispersion (5% in alcohol and water) was purchased from Sigma-Aldrich and solvent exchanged for DMF to make a 5 wt% stock solution following previous literature examples.[13] Nafion 212 was purchased from Ion Power and pretreated following standard procedures.[28] Briefly, membranes were soaked in a 3% hydrogen peroxide aqueous solution at 80 °C for 1 hour before being thoroughly washed with nanopure water and subsequently soaked in nanopure water at 80 °C for another hour. Finally, the membranes were soaked in a 1 M sulfuric acid aqueous solution at 80 °C for 1 hour before being rinsed with nanopure water one final time and stored at room temperature in 1 M sulfuric acid until use.

Table 2.1. GO batch material sourcing

GO batch name	Graphite Source
GO_A	Aldrich (50 mesh)
GO_B	Ukraine (GAK-2, 325 mesh)
GO_C*	Ukraine (GAK-2, 325 mesh)
GO_D	Ukraine (GAK-2, 325 mesh)
GO_E	Graphene Laboratories Inc (as commercial GO-paste)

*GO_C was used for all experiments unless otherwise noted

BPM fabrication

BPMs were prepared by a slight modification of a previously reported procedure.[12] Briefly, 3 cm x 3 cm anion exchange membrane (AEM) sheets were soaked in 1 M KOH for approximately 10 minutes. The membranes were next rinsed with nanopure water and firmly secured to a glass slide with Scotch tape. Graphite oxide (GO) was then deposited onto the AEM following a variety of techniques described below. Following GO deposition, the membrane glass slide was placed on a hot plate kept between 120-130 °C and sprayed with 1 mL of a 1.5 wt% Nafion 117 in DMF dispersion to form the cation exchange layer (CEL). Following CEL deposition, the scotch tape was removed from the membrane and glass slide and a single sheet of aluminum foil was placed on top of the exposed side of the BPM. The newly formed BPM was hot-pressed between an aluminum foil sheet and the original glass slide at 165 °F at 2000 psi for 20 minutes. The obtained BPM was stored in atmospheric conditions at room temperature before testing.

Catalyst deposition techniques

GO catalyst layers were deposited following one of three techniques (solution assembly, Langmuir Blodgett, air spraying) as detailed below:

Solution Assembly (SA)

Following securing of the AEM to a glass slide, approximately 1 mL of a 1.5 mg/mL aqueous GO suspension previously sonicated for 30 min was dropped onto the membrane surface and left to stand for 20 min. Following 20 min, the remaining GO was thoroughly rinsed away with nanopure water and the AEM/GO membrane was dried using an air gun.

Langmuir Blodgett (LB)

LB depositions were conducted using a KSV Nima LB with a trough size of 7.5x16 cm. Following securing of the AEM to a glass slide using Scotch tape, the membrane was further secured using Kapton tape. A 1 mg/mL dispersion of GO in isopropyl alcohol (IPA) was sonicated for 30 minutes. The LB trough was filled with nanopure water and the AEM glass slide was clipped into a starting position either above the water or already submerged in the water (Table 2.2). A specified amount (Table 2.2) of the GO/IPA dispersion was gently dropped using a 1 mL syringe on the surface of the water such that a film of GO formed on the water surface. The GO film was allowed to sit for 15 min before the glass slide was either removed from the water or dipped and subsequently removed from the water at a rate of 27 mm/min as the trough size compressed at a rate of 3 mm/min. The resultant AEM/GO assembly was allowed to gradually air dry and was not rinsed with water.

Table 2.2. Langmuir-Blodgett deposition details

Sample	Added GO*	Start position	Dip number
7 ±4% coverage	0.5 mL	In water	1
53 ±4% coverage	1.0 mL	In water	1
63 ±5% coverage	1.5 mL	In water	1
100% coverage	2.5 mL	Above water	3

* Accurate isotherms of GO monolayers were hard to measure using the LB technique due to formation of GO multilayers upon compression of the surface GO sheets instead of deviations in surface tension. As such, isotherm data is not provided, and numerical confirmation of monolayer formation was hard to achieve.

Air spraying

A 1.5 mg/mL aqueous suspension of GO was prepared by sonication. The AEM/glass slide assembly was placed on a hot plate kept at ~100 °C and sprayed with 150 µL of GO suspension.

Electrochemical measurements

Polarization curves (j-E curves) of BPMs were taken using a four-electrode design previously reported.[11] Briefly, the BPM was placed between the central chambers of an H-Cell with a 1 cm x 1 cm area exposed to Haber-Luggin capillaries in which Ag/AgCl reference electrodes were placed. At the far ends of the H-Cell, platinum wires were employed as working and counter electrodes. These wires were separated from the other H-Cell components by AEMs and CEMs to minimize the influence of any product generated at the surface of the platinum electrodes. For water dissociation overpotential measurements, the reference electrodes were connected to an EZStat Pro Potentiostat-Galvanostat

(NuVant Systems) to monitor cross-membrane potential. The platinum wires were connected to a DC power supply (Agilent E3612), from which galvanostatic steps were applied. For these overpotential measurements 1 M sulfuric acid and 1 M potassium hydroxide were utilized on the negative and positive sides respectively. For permselectivity measurements, a PGSTAT302N (Metrohm, Autolab) was used. The platinum wires were connected as working and counter electrodes, and the reference electrodes were connected as reference and sensing electrodes. A galvanostatic step experiment was employed at low current values. For these permselectivity measurements, 0.5 M potassium sulfate was used on both the positive and negative sides.

For proton GO ion conductivity tests, 5wt% Nafion 117 was sprayed on top of a Nafion 212/GO assembly as deposited by LB deposition (Table 2.2) to fully cover the GO. Experiments were conducted in an H-Cell containing 1 M sulfuric acid on both sides. For hydroxide GO ion conductivity tests, 5 wt% Sustainion XA-9 (Dioxide Materials, Fuel Cell Store) was sprayed on top of a AEM (Fumasep FAS-30)/GO assembly as deposited by LB deposition (Table 2.2) to fully cover the GO. Experiments were conducted in an H-Cell containing 1 M potassium hydroxide on both sides.

Optical imaging

Optical images were taken on an Olympus BX60M microscope using specified objective lenses. Images were processed to calculate catalyst coverage using a thresholding approach on ImageJ (see more detailed description below)

Spectroscopic measurements

RAMAN measurements were taken on a JASCO NRS-5500 Laser Raman Spectrometer using a 100x objective and a 785 nm laser. Infrared measurements were taken on a Bruker Vertex 70v instrument in transmission mode.

Quantifying GO coverage using ImageJ software

Quantification of orientated GO nanosheet coverage was conducted using a thresholding method built into the ImageJ software. Image processing follows the flow depicted in supporting schemes. Coverage is reported as an average of at least three different regions of the processed image in order to determine the uniformity of distribution.

After uploading and opening an image with the ImageJ software, the image type is switched to 8-bit gray scale (*Image → Type → 8-bit*). The 8-bit image is then processed by the enhance contrast feature until clear definition is seen between the GO nanosheets and the AEL background (*Process → Enhance Contrast → change percent to desired value*). A threshold is then set to transform the image to a binary black and white image (*Image → Adjust → Threshold → move bar to desired balanced value)*. Finally, the analyze particle tool is used to determine the area of the negative (black) space, here representing the AEL surface (*Analyze → Analyze Particles*).

Notably, thick multilayers of GO nanosheets appear darker than thin multilayers, and upon contrast enhancement and thresholding may appear as background. As such, area quantifications may be under estimations, especially for the high coverage samples where thick multilayers more readily form. An example of a thick multilayer nanosheet that was not counted in the surface area of the 60% coverage LB sample is labeled with a red star in supporting schemes.

Numerical model details

Both numerical models were built and solved using a COMSOL 5.1 Multiphysics package. Built-in Nernst-Planck-Poisson equations are used to describe ion transport and potential distribution in both models.

Model 1: 1D BPM (Fig. 2.5A, 2.14)

Model 1 is a 1D numerical model of a BPM adapted from a previously reported study.[11] Here, we used "Model 3" from that paper, in which both water dissociation and water formation are catalyzed. All parameters apart from the hydroxide ion conductivity and fixed charge in the catalyst layer were the same as used previously. The model geometry consisted of two 50 μm lengths of electrolyte on either side of a BPM composed of a 20 μm AEL and a 20 μm CEL. A 10 nm region at the AEL|CEL interface was assigned as the catalytic region where a catalytic enhancement factor of $10^{3.5}$ was applied to the rate of water formation and dissociation. In that region, the hydroxide ion diffusion coefficient was either equal to that reported in the parameter table below ("bipolar conductivity") or multiplied by a factor of 10^{-1} to represent low hydroxide ion conductivity through the GO catalyst layer. The membrane fixed charge was set to zero in the catalyst region.

All physics, variables, and equations including Onsager's theory on water dissociation in weak electrolytes were kept identical to that of the adapted model.[11] A stationary solver was used to solve for model 1. Parameters and boundary conditions used in this model include:

Table 2.3. Parameters used in Model 1

Parameter	Value
Temperature	298.15 [K]
Membrane fixed charge, c_fix	0.3 [mol/L]
Membrane permittivity	30
Electrolyte permittivity	80
Diffusion K^+	1.9e-5 [cm^2/s]
Diffusion Cl^-	2.03e-5 [cm^2/s]
Diffusion H^+	9.3e-5 [cm^2/s]
Diffusion OH^-	5.3e-5 [cm^2/s]
Diffusion H_2O	2.5e-9 [m^2/s]
Water association rate constant (2^{nd} order)	1.3e-11 [$M^{-1}*s^{-1}$]
Water dissociation rate constant (1^{st} order)	2e-5 [1/s]

Table 2.4. Initial conditions used in Model 1

Condition	AEL-facing electrolyte	AEL	CEL	CEL-facing electrolyte
Concentration K^+	0.1 [M]	0	0	0
Concentration Cl^-	0	0	0	0.1 [M]
Concentration H^+	0	0	c_fix	0.1 [M]
Concentration OH^-	0.1[M]	c_fix	0	0
Concentration H_2O	56 [M]	56 [M]	56 [M]	56 [M]

Model 2: 2D GO flake in a tank of pH neutral water (Fig. 2.5B, 2.15)

Model 2 geometry consisted of a square 2D tank of pH neutral water with 0.5 [µm] edge length. A 1 [nm] thick and 0.48 [µm] tall GO nanosheet was placed in the middle of the tank such that the long edges of the GO nanosheet ran in the Y-axis direction of the model (Fig. 2.15A). A constant electric potential of 1 [V] was applied across the tank of water perpendicular to the long edge of the GO-nanosheet. Water dissociation based on the equilibrium constant of water was assumed to occur everywhere:

$$H_2O \underset{k_a}{\overset{k_d}{\rightleftarrows}} H^+ + OH^- \quad (1)$$

Where rates of formation of all species (H_2O, H^+, OH^-) present in the model can be written as:

$$R_{H^+} = R_{OH^-} = -R_{H_2O} = k_d[H_2O] - k_a[H^+][OH^-] \quad (2)$$

In this model, the GO nanosheet catalyzes both water formation and dissociation by a factor of $10^{2.5}$ such that:

$$k_d = k_d^0 \times \begin{cases} 10^{2.5}, & (x,y)\ at\ GO\ flake \\ 1, & (x,y)\ elsewhere \end{cases} \quad (3)$$

$$k_a = k_a^0 \times \begin{cases} 10^{2.5}, & (x,y)\ at\ GO\ flake \\ 1, & (x,y)\ elsewhere \end{cases} \quad (4)$$

Diffusion of hydroxide ions through the GO nanosheet is a probed variable in this experiment as

$$D_{OH} = D_{OH}^0 \times \begin{cases} 10^{exp}, & (x,y)\ at\ GO\ flake \\ 1, & (x,y)\ elsewhere \end{cases} \quad (5)$$

Where D^0_{OH} is hydroxide diffusion as defined in Table 2.5 and *exp* is a variable probed at values ranging from 0 to -1. A value of exp = -1 is reported in Fig. 2.5B.

A time-dependent solver is used to solve for model 2. Parameters and boundary conditions used in this model include:

Table 2.5. Parameters used in Model 2

Parameter	Value
Temperature	298.15 [K]
Relative permittivity	18
Diffusion H^+	9.3e-5 [cm^2/s]
Diffusion OH^-	9.3e-5 [cm^2/s]
Diffusion H_2O	2.5e-9 [m^2/s]
Water formation rate constant (2^{nd} order)	1.3e-11 [$M^{-1}*s^{-1}$]
Water dissociation rate constant (1^{st} order)	2e-5 [1/s]
Concentration H_2O	56 [M]
Applied voltage	-1 [V]

Supporting images

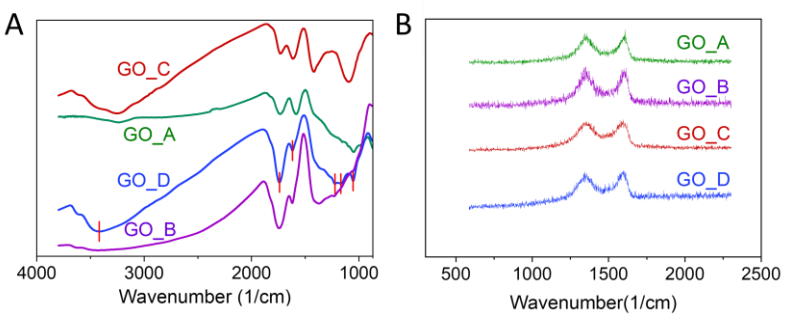

Figure 2.6. (A) Infrared spectra of four different synthesized batches of GO. (B) RAMAN spectra of four different synthesized batches of GO. Details on sourced starting material for the different batches can be found in Table 2.1.

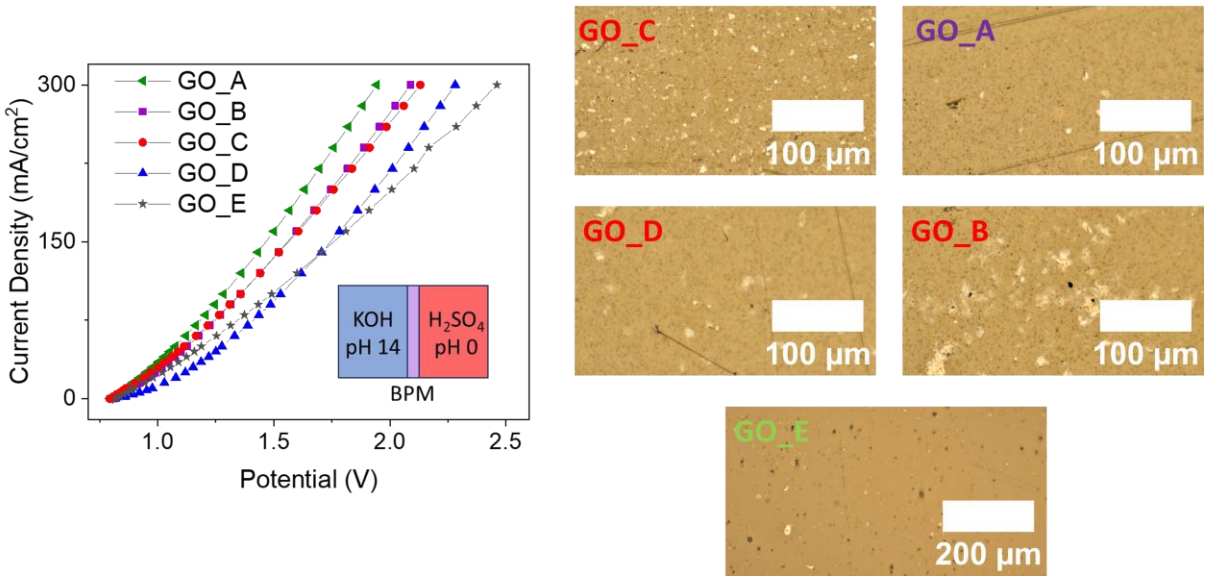

Figure 2.7. Overpotential j-E-curves of different synthesized batches of GO and a commercially sourced GO (GO_E) and the associated optical images of different GO batches deposited on an AEL surface using SA deposition techniques. Details on sourced starting material for the different batches can be found in Table 2.1.

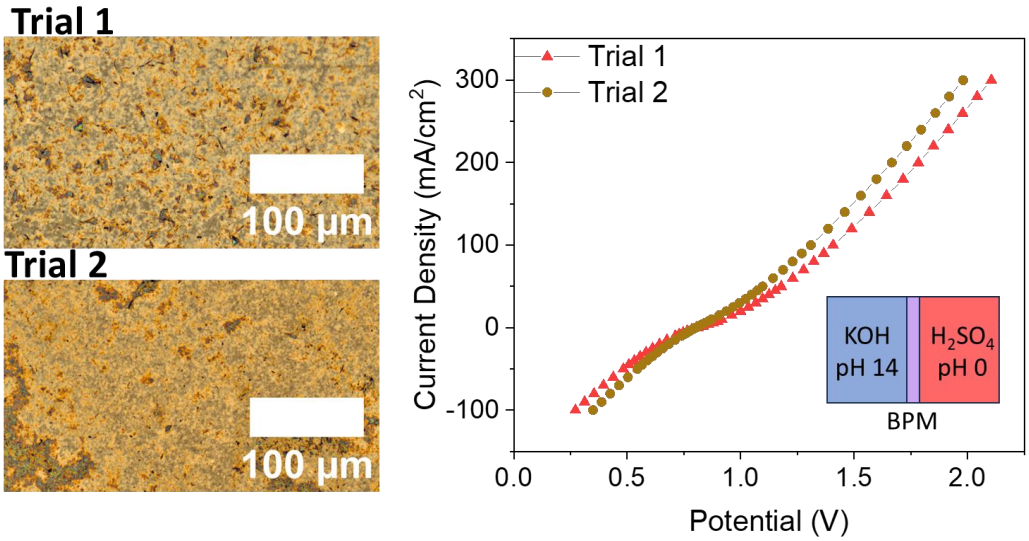

Figure 2.8. Overpotential j-E curves (right) of two different BPMs containing spray deposited GO interface. Optical images of the two different catalyst interfaces are depicted on the left.

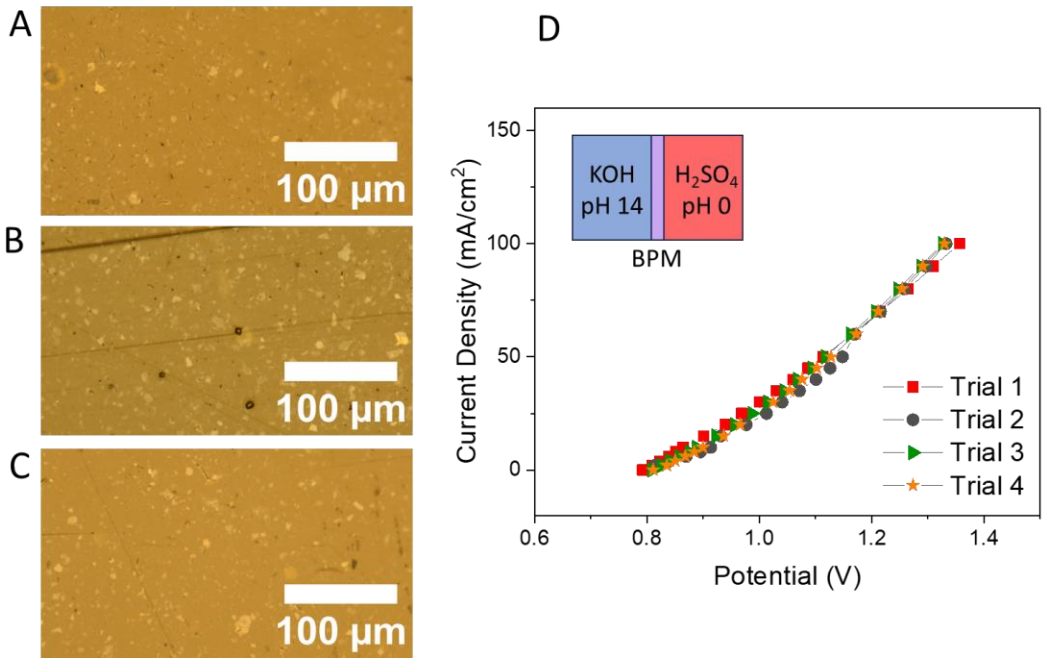

Figure 2.9. (A-C) Optical microscope images of three different solution adsorption (SA) GO_C depositions on a Fumasep AEM. The areal coverage of GO_C deposited through the SA technique was 6.5 (±1.9%) based on eight separate samples. (D) j-E curves for four different BPMs, all with GO_C as the catalyst, deposited via the SA method.

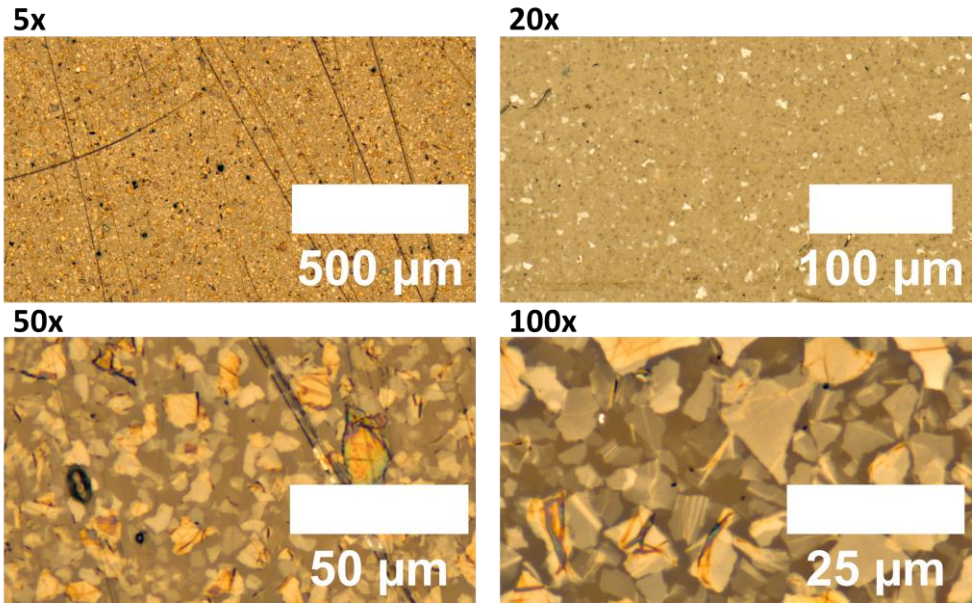

Figure 2.10. Optical images of GO deposited on an AEL surface using LB deposition techniques at different optical microscope objectives.

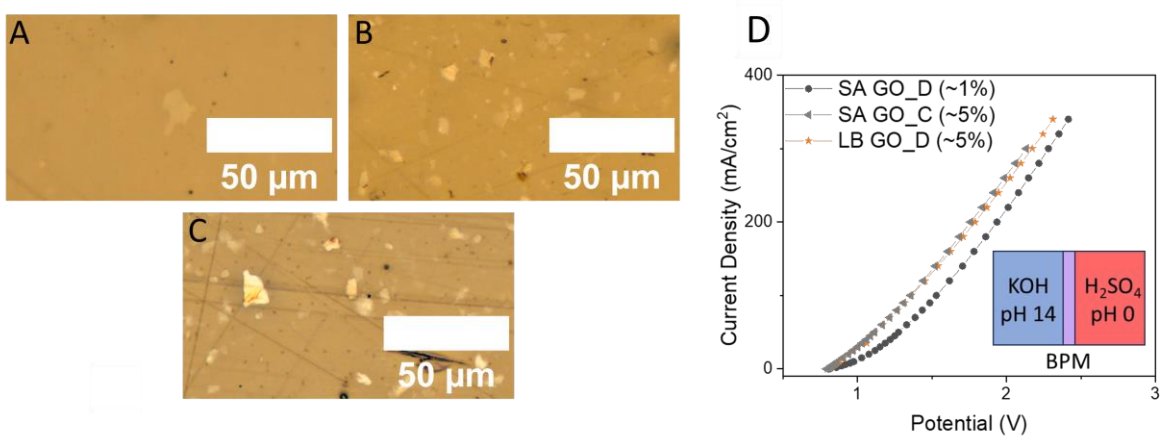

Figure 2.11. (A-C) Optical images of GO deposited on a Fumasep AEL using (A) SA of GO_D, (B) SA of GO_C, and (C) LB of GO_D. (D) Overpotential j-E curves of BPMs containing A-C interfacial GO regions.

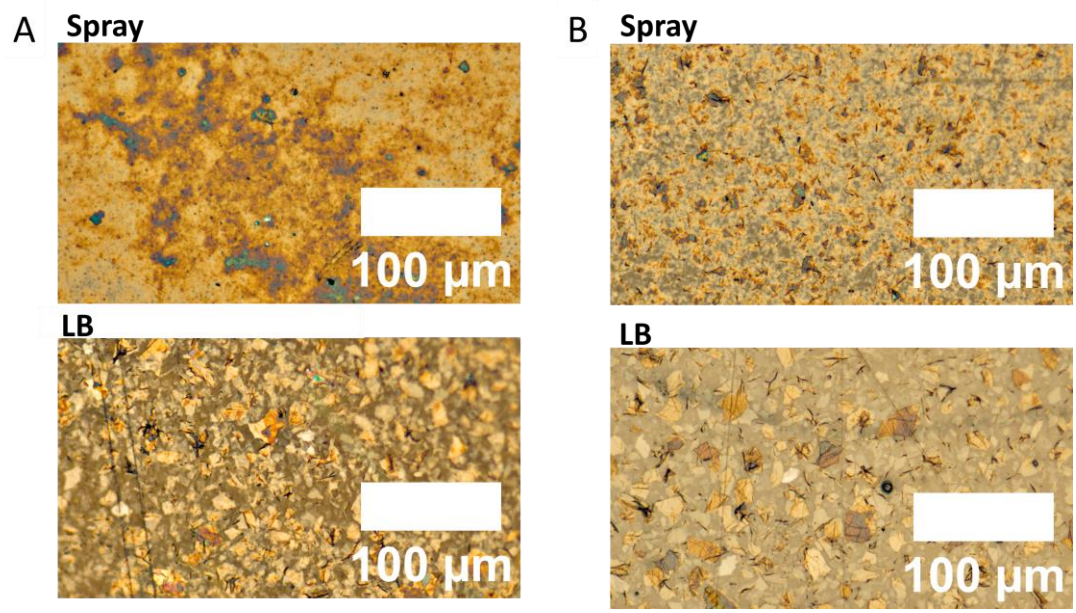

Figure 2.12. Optical images of different GO deposition types on an AEL. These GO interfaces were made into BPMs which were tested for (A) permselectivity performance in Figure 2.2A and (B) overpotential performance in Figure 2.2B.

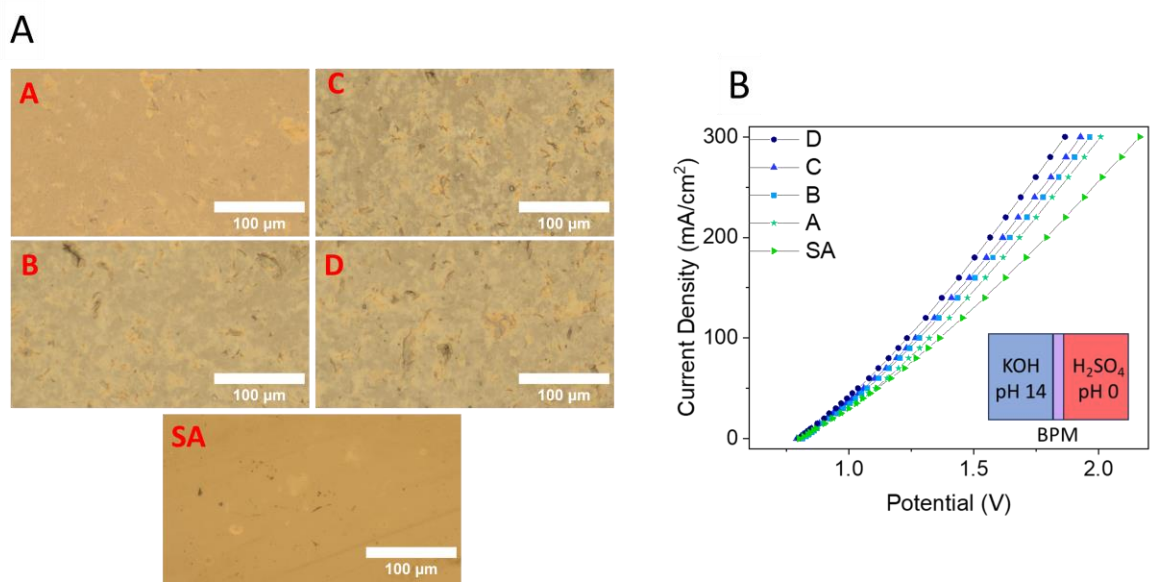

Figure 2.13. (A) Optical images of GO_B deposited on a Piperion AEL surface using LB deposition. These GO interfaces were made into BPMs. While coverage quantification cannot be made due to poor color contrast, qualitatively we can see that coverage follows the trend: D>C>B>A>SA. (B) Overpotential j-E-curves of these BPMs.

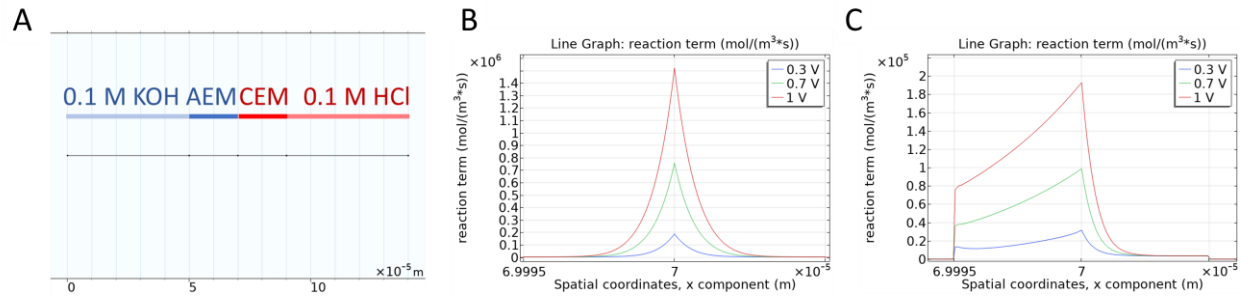

Figure 2.14. Numerical model 1's (A) example geometry, (B) catalytic reaction rate under bipolar ionic conductivity conditions and (C) x10 slower hydroxide ion conductivity in the catalyst region conditions.

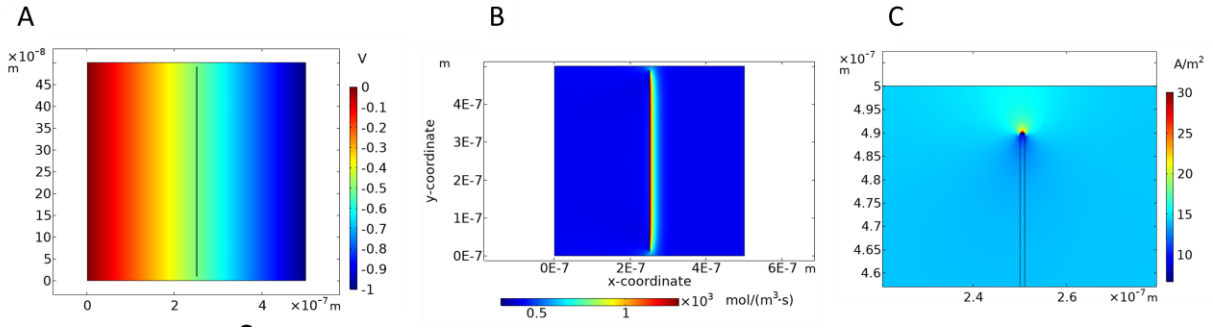

Figure 2.15. Numerical model 2's (A) example geometry under an applied electric field. (B) Full tank view of asymmetrical and increased (red) water association rates around a catalytically active GO flake made ten times less conductive towards hydroxides than protons. A zoomed in perspective of this plot is shown in Fig. 2.5B. and (C) Current density around the catalytically active and nonbipolar ionically conductive GO flake. A higher current (red) is seen at the ends of the GO flake where hydroxide ions can more readily migrate.

Supporting schemes

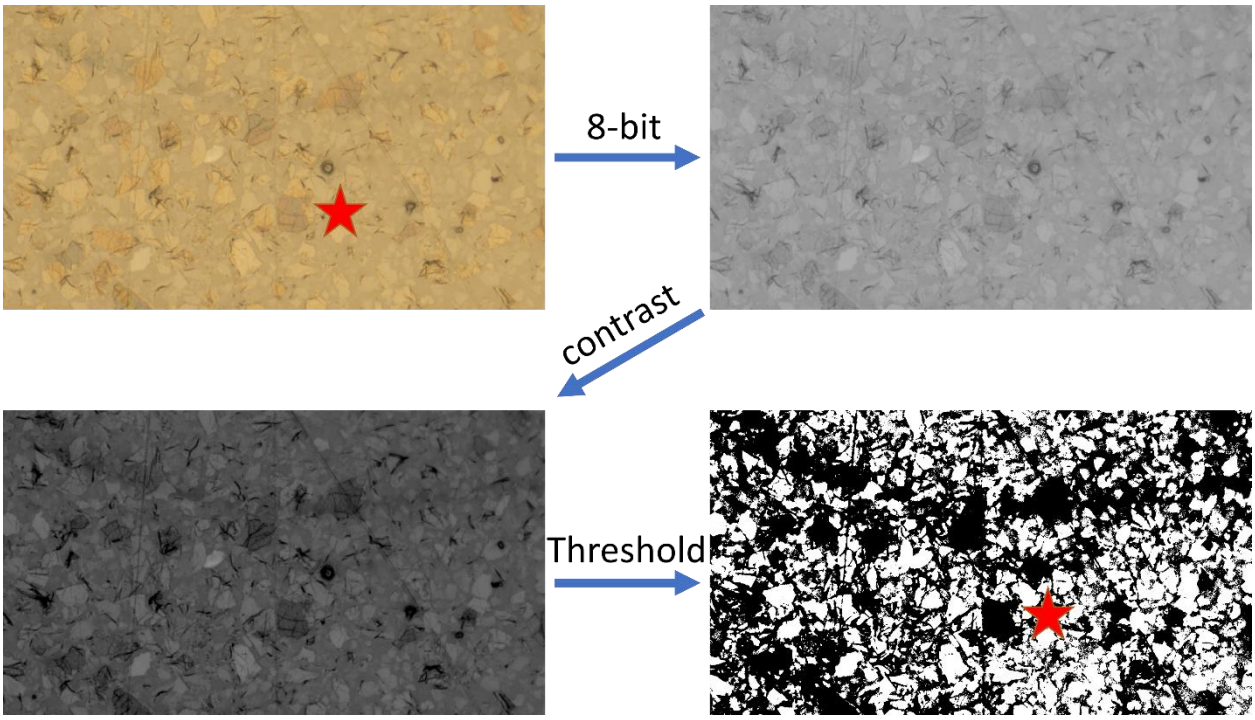

Scheme 2.1. Schematic of the process used to quantify orientated GO coverage using ImageJ software.

References

(1) Giesbrecht, P. K.; Freund, M. S. Recent Advances in Bipolar Membrane Design and Applications. *Chem. Mater.* **2020**, *32* (19), 8060-8090.

(2) Parnamae, R.; Mareev, S.; Nikonenko, V.; Melnikov, S.; Sheldeshov, N.; Zabolotskii, V.; Hamelers, H. V. M.; Tedesco, M. Bipolar membranes: A review on principles, latest developments, and applications. *J. Memb. Sci.* **2021**, *617*, 118538.

(3) Vermaas, D. A.; Wiegman, S.; Nagaki, T.; Smith, W. A. Ion transport mechanisms in bipolar membranes for (photo)electrochemical water splitting. *Sustain. Energ. Fuels.* **2018**, *2* (9), 2006-2015.

(4) Yan, Z. F.; Mallouk, T. E. Bipolar Membranes for Ion Management in (Photo)Electrochemical Energy Conversion. *Acc. Mater. Res.* **2021**, *2* (12), 1156-1166.

(5) Luo, J. S.; Vermaas, D. A.; Bi, D. Q.; Hagfeldt, A.; Smith, W. A.; Grätzel, M. Bipolar Membrane-Assisted Solar Water Splitting in Optimal pH. *Adv. Energy Mater.* **2016**, *6* (13).

(6) Ünlü, M.; Zhou, J. F.; Kohl, P. A. Hybrid Anion and Proton Exchange Membrane Fuel Cells. *J. Phys. Chem. C.* **2009**, *113* (26), 11416-11423.

(7) Ahlfield, J. M.; Liu, L. S.; Kohl, P. A. PEM/AEM Junction Design for Bipolar Membrane Fuel Cells. *J. Electrochem. Soc.* **2017**, *164* (12), F1165-F1171.

(8) Digdaya, I. A.; Sullivan, I.; Lin, M.; Han, L. H.; Cheng, W. H.; Atwater, H. A.; Xiang, C. X. A direct coupled electrochemical system for capture and conversion of CO_2 from oceanwater. *Nat. Commun.* **2020**, *11* (1), 4412.

(9) Bui, J. C.; Lucas, E.; Lees, E. W.; Liu, A. K.; Atwater, H. A.; Xiang, C. X.; Bell, A. T.; Weber, A. Z. Analysis of bipolar membranes for electrochemical CO_2 capture from air and oceanwater. *Energy Environ. Sci.* **2023**, *16* (11), 5076-5095.

(10) Yan, Z. F.; Hitt, J. L.; Zeng, Z. C.; Hickner, M. A.; Mallouk, T. E. Improving the efficiency of CO2 electrolysis by using a bipolar membrane with a weak-acid cation exchange layer. *Nat. Chem.* **2021**, *13* (1), 33.

(11) Yan, Z. F.; Wycisk, R. J.; Metlay, A. S.; Xiao, L. Q.; Yoon, Y.; Pintauro, P. N.; Mallouk, T. E. High-Voltage Aqueous Redox Flow Batteries Enabled by Catalyzed Water Dissociation and Acid-Base Neutralization in Bipolar Membranes. *ACS Cent. Sci.* **2021**, *7* (6), 1028-1035.

(12) Metlay, A. S.; Chyi, B.; Yoon, Y.; Wycisk, R. J.; Pintauro, P. N.; Mallouk, T. E. Three-Chamber Design for Aqueous Acid-Base Redox Flow Batteries. *ACS Energy Lett.* **2022**, 7 (3), 908-913.

(13) Yan, Z. F.; Zhu, L.; Li, Y. G. C.; Wycisk, R. J.; Pintauro, P. N.; Hickner, M. A.; Mallouk, T. E. The balance of electric field and interfacial catalysis in promoting water dissociation in bipolar membranes. *Energy Environ. Sci.* **2018**, *11* (8), 2235-2245.

(14) Bui, J. C.; Corpus, K. R. M.; Bell, A. T.; Weber, A. Z. On the Nature of Field-Enhanced Water Dissociation in Bipolar Membranes. *J. Phys. Chem. C* **2021**, 125 (45), 24974-24987.

(15) Chen, L. H. K.; Xu, Q. C.; Oener, S. Z.; Fabrizio, K.; Boettcher, S. W. Design principles for water dissociation catalysts in high-performance bipolar membranes. *Nat. Commun.* **2022**, *13* (1), 3846.

(16) Chen, L. H. K.; Xu, Q. C.; Boettcher, S. W. Kinetics and mechanism of heterogeneous voltage-driven water-dissociation catalysis. *Joule* **2023**, *7* (8), 1867-1886.

(17) Oener, S. Z.; Foster, M. J.; Boettcher, S. W. Accelerating water dissociation in bipolar membranes and for electrocatalysis. *Science* **2020**, 369 (6507), 1099.

(18) Oener, S. Z.; Twight, L. P.; Lindquist, G. A.; Boettcher, S. W. Thin Cation-Exchange Layers Enable High-Current-Density Bipolar Membrane Electrolyzers via Improved Water Transport. *ACS Energy Lett.* **2021**, *6* (1), 1-8.

(19) Shen, C. H.; Wycisk, R.; Pintauro, P. N. High performance electrospun bipolar membrane with a 3D junction. *Energy Environt. Sci.* **2017**, *10* (6), 1435-1442.

(20) McDonald, M. B.; Freund, M. S. Graphene Oxide as a Water Dissociation Catalyst in the Bipolar Membrane Interfacial Layer. *ACS Appl. Mater. Interfaces.* **2014**, *6* (16), 13790-13797.

(21) Schulte, L.; White, W.; Renna, L. A.; Ardo, S. Turning water into a protonic diode and solar cell via doping and dye sensitization. *Joule* **2021**, *5* (9), 2380-2394.

(22) Kole, S.; Venugopalan, G.; Bhattacharya, D.; Zhang, L.; Cheng, J.; Pivovar, B.; Arges, C. G. Bipolar membrane polarization behavior with systematically varied interfacial areas in the junction region. *J. Mater. Chem. A.* **2021**, *9* (4), 2223-2238.

(23) Jiang, Z.; Bazianos, P. P.; Yan, Z. F.; Rappe, A. M. Mechanism of Water Dissociation with an Electric Field and a Graphene Oxide Catalyst in a Bipolar Membrane. *ACS Catal.* **2023**, *13* (10), 7079-7086.

(24) Lerf, A.; He, H. Y.; Forster, M.; Klinowski, J. Structure of graphite oxide revisited. *J. Phys. Chem. B.* **1998**, *102* (23), 4477-4482.

(25) Kovtyukhova, N. I.; Ollivier, P. J.; Martin, B. R.; Mallouk, T. E.; Chizhik, S. A.; Buzaneva, E. V.; Gorchinskiy, A. D. Layer-by-layer assembly of ultrathin composite films from micron-sized graphite oxide sheets and polycations. *Chem. Mater.* **1999**, *11* (3), 771-778.

(27) Lucas, E.; Bui, J.; Hwang, M.; Wang, K.; Bell, A.; Weber, A.; Ardo, S.; Atwater, H.; Xiang, C. Asymmetric bipolar membrane for high current density electrodialysis operation with exceptional stability. Preprint at C*hemRxiv*, **2023**.

(28) Lin, K. X.; Chen, Q.; Gerhardt, M. R.; Tong, L. C.; Kim, S. B.; Eisenach, L.; Valle, A. W.; Hardee, D.; Gordon, R. G.; Aziz, M. J.; et al. Alkaline quinone flow battery. *Science* **2015**, *349* (6255), 1529-1532.

CHAPTER 3: THREE-CHAMBER DESIGN FOR AQUEOUS ACID-BASE REDOX FLOW BATTERIES

This chapter was previously published as Metlay, A.S.; Chyi, B.; Yoon, Y.; Wycisk, R.J.; Pintauro, P.N.; Mallouk, T.E. *ACS Energy Lett.* **2022**, 7 (3), 908-913. It is reproduced with permission, copyright 2022, American Chemical Society. I was the primary author and conducted the majority of the experimental work and manuscript writing.

Abstract

Aqueous acid−base redox flow batteries exploit a pH gradient maintained by a bipolar membrane to increase the energy storage capacity of the cell. An earlier study using a ferro-/ ferricyanide redox couple revealed that redox molecule transport processes rapidly degrade the bipolar membrane and cell cycle life. Here, we mitigate this problem using a three-chamber cell design that interposes a cation exchange membrane between the positive electrolyte and an inner KOH electrolyte on the basic side of the bipolar membrane. This arrangement improves the stability and cycle life of the cell. In addition, the KOH solution in the central chamber maintains the pH gradient across the bipolar membrane, eliminating the requirement for a high pH positive electrolyte. Highly positive and soluble redox couples such as bromine/ bromide that are unstable under strongly alkaline conditions can be used with the three-chamber design against 2,7- disulfonate-9,10-anthraquinone, achieving an open circuit voltage of ∼1.7 V.

Introduction

The intermittent nature of renewable energy sources such as solar and wind creates a need for reliable grid-level electrochemical energy storage systems. Redox flow batteries (RFBs) have been widely studied as a potentially cost-effective solution for electrical energy storage over periods of hours to weeks.[1,2] The independent scaling of RFBs' power and capacity, due to the separation of the cell stack and electrolyte tank, enables their unique customizability. Aqueous RFBs (ARFBs) in particular offer the additional benefits of low solvent cost and toxicity, as well as low series resistive losses, relative to their organic solvent counterparts, which can often achieve higher cell voltages. Consequently, the best developed systems, such as the all-vanadium,[3] zinc−bromine,[4] and polysulfide−bromine[5] ARFBs, utilize aqueous electrolytes. ARFBs containing water-soluble organic molecules[6,7] and abundant transition metals[8] such as iron have also been developed for use across a range of electrolyte pH values.[9−11] In these systems, both the negative and the positive sides of the RFB are typically in the same pH environment due to the monopolarity and permeability of the system's ion exchange membrane (IEM).[12,13]

A significant limitation of ARFBs is the narrow electrochemical window of water. Water is thermodynamically stable up to a potential difference of 1.23 V, although in practice the voltage of AFRBs can exceed this value because of the slow kinetics of the hydrogen and oxygen evolution reactions at carbon electrodes.[14] The acid−base redox flow battery (acid−base RFB) extends the thermodynamic limit of water decomposition by adding a cross-membrane potential.[15] By using a bipolar membrane (BPM) to separate the aqueous compartments,[16,17] the acid−base RFB can maintain different pH environments on its positive and negative sides even with continuous cycling. The BPM's anion exchange layer (AEL) faces the positive electrode, its cation exchange layer (CEL) faces the negative electrode, and water dissociation catalyst such as graphite oxide is located at the AEL/CEL

interface. Under reverse bias, water dissociates in the BPM junction. Hydroxide ions move through the positively charged AEL toward the positive electrode, and protons move through the negatively charged CEL toward the negative electrode. The opposite process occurs in forward bias with hydroxide ions and protons moving toward the AEL/CEL interface, where the acid−base neutralization reaction takes place. The sum of the resulting liquid−membrane and membrane−membrane interfacial potential drops results in a pH-dependent cross-membrane potential, which is independent of the redox couples used as long as their formal potentials are pH-independent.[16] Because the BPM selectively conducts protons and hydroxide ions, each unit of pH difference across the membrane adds approximately 59 mV to the cell voltage. Thus, a ΔpH of 14 across the bipolar membrane theoretically provides 830 mV of added voltage.[18]

Yan et al. recently exploited this effect to make aqueous acid−base RFBs that significantly exceeded the 1.23 V thermodynamic window of a single-pH ARFB.[15] Unfortunately, the acid−base RFB system reported in that study had poor retention of charge and discharge capacity.

This poor stability is likely due to transport of redox ions into the junction, which led to BPM fouling and a significant increase in membrane resistivity. The two parasitic processes, illustrated in Figure 3.1C, are migration of the positive redox couple ($[Fe(CN)_6]^{3-/4-}$) through the positively charged AEL and leakage of the anionic negative redox couple, 2,7- disulfonate-9,10-anthraquinone ($DSAQ^{2-}$), through the negatively charged CEL. Here, leakage is defined as the transport of a co-ion that has the same charge type as the fixed charge of the membrane layer. Cation exchange materials such as Nafion are particularly prone to this form of leakage due to the presence of water channels.[19−21]

The other mode of crossover in the acid−base RFB system is migration of the negatively charged, positive redox couple through the positively charged AEL. These redox anions can be trapped at the

AEL/CEL interface or transport slowly through the CEL via the leakage mechanism (Fig. 3.1C). Ferro-/ ferricyanide is often used as the positive redox couple in alkaline ARFBs.[10,11,15,22] In typical alkaline systems in which a cation exchange membrane (CEM) is used instead of a BPM, slow leakage occurs but does not immediately compromise the stability of the RFB.[23] However, in the acid−base RFB system in which ferro-/ferricyanide ions can compete with hydroxide for sites in the AEL, migration leads to a rapid rise in membrane resistance, most likely by trapping of ferro-/ ferricyanide ions at the AEL/CEL interface.

Here we report a two-part solution for circumventing the problem of membrane fouling in the acid−base RFB. First, by varying the thickness of the CEL in the BPM, we determined the dependence of negative redox ion leakage on CEL thickness and could minimize that effect. Second, we developed a three-chamber RFB design in which an additional CEM separates the positive electrolyte from a central aqueous KOH chamber. Thus, the highly alkaline, redox-molecule-free electrolyte contacts the AEL of the BPM (Fig. 3.1B) and exchanges K^+ ions with the electrolyte compartment that contains the negatively charged, positive redox couple (ferro-/ ferricyanide or bromine/bromide). A BPM with a relatively thick CEL (labeled below as 500-BPM) was used in the three-chamber experiments to minimize DSAQ leakage. While other three-chamber RFB systems have been previously studied,[24,25] none of them have so far utilized a BPM to maintain a pH dependent cross-membrane potential.

Results and Discussion

An additional advantage of the redox-molecule-free central chamber is that it can maintain a large pH gradient across the BPM without constraining the positive redox molecule to be stable in a strongly alkaline environment. By using degassed 5 M KOH in the central chamber and 1 M H2SO4 in the negative electrolyte chamber, a ΔpH of ∼15 pH units and thus a cross-BPM potential of ∼885 mV were

measured. Paired with the relatively air-stable (compared to viologens) DSAQ− ferrocyanide redox couples, we measured a ∼1.3 V open circuit voltage (Fig. 3.1D). Ferrocyanide is not indefinitely stable under highly alkaline conditions,[22] so without the central chamber, one could not realize such a high cross-membrane potential without compromising the stability of the cell. Bromine, a highly positive redox molecule that is also unstable under alkaline conditions, can also be used as the positive redox molecule. Bromine is a desirable choice for this system due to its high solubility, positive formal potential, and relatively fast redox kinetics. These benefits are illustrated in the polarization curves of the ferrocyanide−DSAQ system and the bromine− DSAQ system (Fig. 3.1D,E). The cell containing Br_3^-/Br^- in a pH 6.5 phosphate buffer achieves an OCV of ∼1.7 V (Fig. 3.1E). Unfortunately, bromine RFB systems are known to have crossover across Nafion and other CEMs. We notice similar crossover effects in our system. Cycling data as well as a further discussion on the bromine system can be found in the Supporting Information (SI). Nevertheless, the bromine system serves as a proof of concept that a three-chamber system enables the use of a broader range of molecules as the positive redox couple and that the acid−base RFB can reach very high cell potentials.

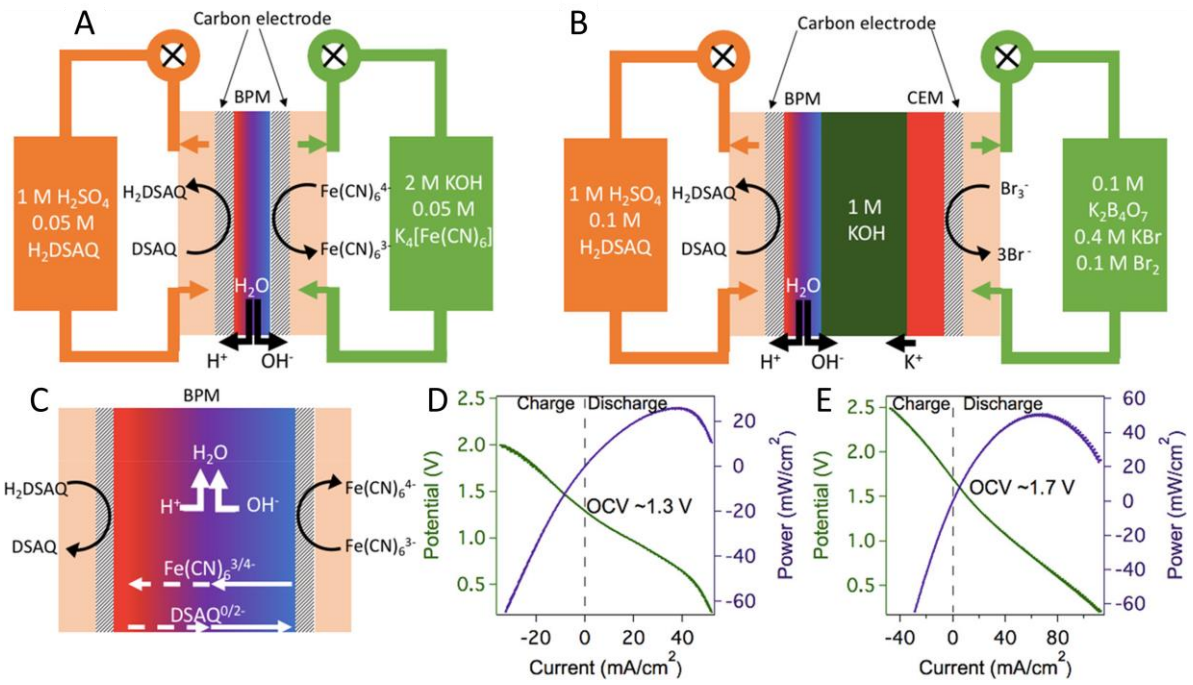

Figure 3.1. (A) Acid–base RFB two-chamber design. (B) Three-chamber design. (C) Transport of molecules in the two-chamber design during discharge (forward bias). Solid lines represent migration, and dashed lines represent leakage. (D) Polarization and power curves of a three-chamber acid–base RFB containing 50 mM DSAQ in 1 M H_2SO_4, 50 mM ferrocyanide in 2 M KOH, and degassed 5 M KOH. Scan rate of 100 mV/s. (e) Polarization and power curves of a three-chamber acid–base RFB with 0.1 M DSAQ in 1 M H_2SO_4, 0.1 M Br_2, and 0.4 M KBr in 0.1 M pH ~ 6.5 phosphate buffer, and 1 M KOH. Scan rate of 100 mV/s.

Two different CEMs were studied as separators between the positive and central chambers in the three-chamber design, Nafion 212 (Nafion) and Fumasep FKS-30 (Fumasep). In the three-chamber design both CEM types could be charge cycled without significant loss of capacity over 50 cycles (Fig. 3.2B, Fig. 3.6). In contrast, the two-chamber cell shows a significant increase in resistance in each charge cycle (Fig. 3.2A) and, thus, a progressively lower charging capacity before the cell reaches the set potential limit. Here an increase in resistance is apparent in the increasing steepness of the slope of the discharge portion of the cycles and the relatively stable slope of the charge portions of the cycles. The difference

between average charging voltage and average discharging voltage is representative of various impedances present in the cell.

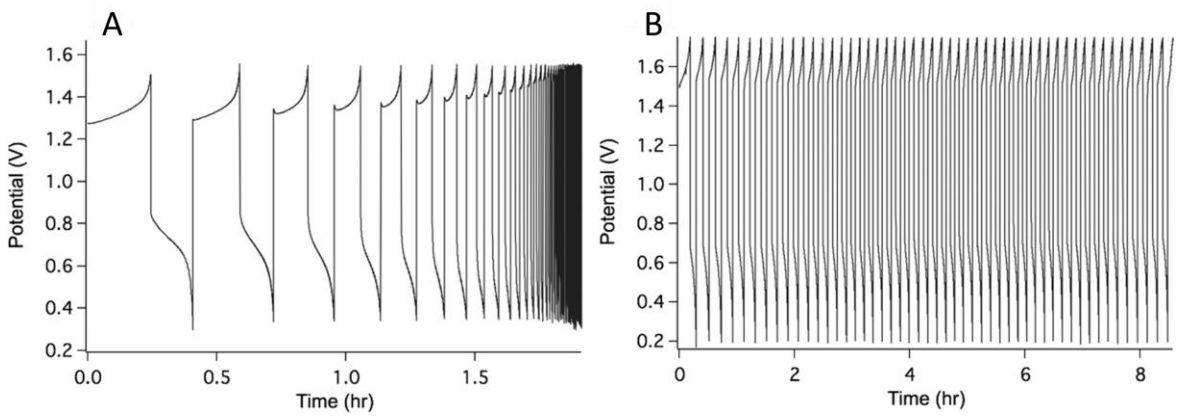

Figure 3.2. Charge cycling in the (A) two-chamber design and (B) three-chamber design using a Fumasep CEM and 5 M KOH in the central chamber. Both experiments used 20 mA/cm^2 charging/discharging cycles, 50 mM $K_4Fe(CN)_6$ in 2 M KOH on the cathodic side, and >50 mM DSAQ in 1 M H_2SO_4 on the anodic side.

An increase in this gap, as is evident in Figure 3.2A, indicates an increase in the overall resistance of the cell. This resistance increase is also reflected in the polarization curve of the two-chamber system taken before and after cycling (Fig. 3.4A). Following the relation $V = iR$, we see a stark increase in resistivity in forward bias (discharging) after cycling but a relatively constant resistance profile in reverse bias (charging). Thus, the measured charge/discharge capacity decays rapidly over the first few cycles in the two-chamber system (Fig. 3.3A). By the end of the cycling experiment there is a 100% charge and discharge capacity fade. Over the first 10 cycles, there is a discharge fade of 21% per cycle (2.1% per min) and a charge capacity fade of 22% per cycle (2.2% per hour). Notably, there appears to be a nonlinear dependence of capacity fade rate on both cycle number and time.

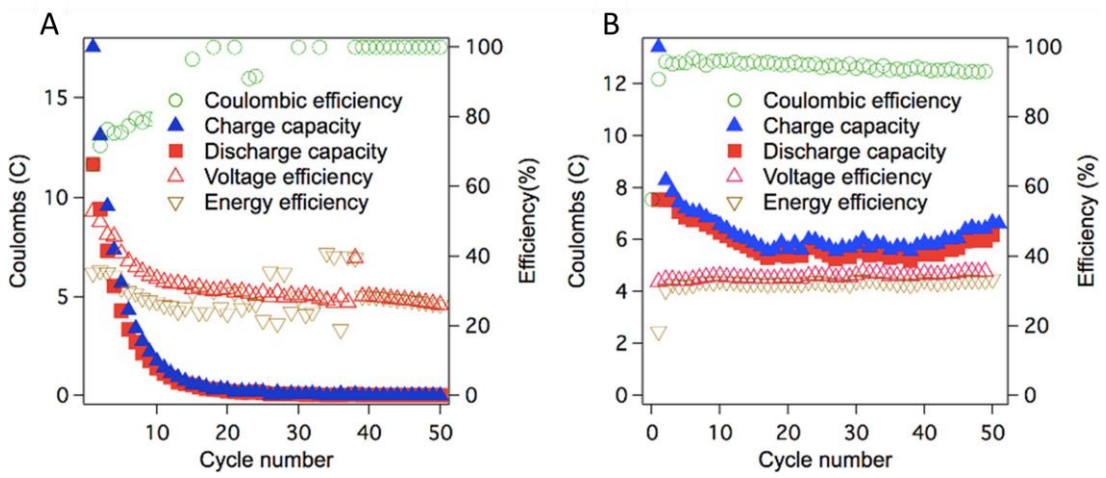

Figure 3.3. Discharge and charge capacity in coulombs and Coulombic, voltage, and energy efficiencies at ±20 mA/cm^2 for the (A) two-chamber and (B) three-chamber designs.

In contrast, in the three-chamber cell, the charge and discharge profiles are similar over the 50 cycles tested (Fig. 3.2B, Fig. 3.6). With both the Nafion and Fumasep CEMs there is an initial decrease in the charging time relative to the theoretical time predicted by Faraday's law. This decrease is likely partially due to an initial mechanical leakage of the electrolyte (Fig. 3.5C). Because 4 mL of electrolyte was cycled through the system throughout the charge cycling process, electrolyte leakage, as is evident from excess liquid left on the graphite flow fields following cell disassembly (Fig. 3.5C) could result in a capacity drop. After this first drop, the Fumasep cell showed an initial capacity decay followed by roughly constant round-trip energy efficiency and capacity over the remaining cycles (Fig. 3.3B). While the specific cause of this initial decay over the first 20 cycles is not definitively known, a possible cause is molecular crossover that eventually reaches an equilibrium state. A comparison of the three-cycle vs the 50-cycle inductively coupled plasma–optical emission spectrometry (ICP-OES) data (Table 3.1) lends support to this theory. A similar amount of iron is found to have crossed over after both three and 50 charge cycles, indicating that a crossover equilibrium may be reached early on, and afterward molecular crossover is

slower. A more rigorous time-based ICP-OES crossover investigation must be conducted to confirm this effect. The average discharge capacity fade is 0.36% per cycle (2.1% per hour) and the average charge capacity fade is 1.2% per cycle (7.0% per hour). However, if the first charge outlier is excluded, the average charge capacity fade is 0.42% per cycle (2.5% per hour), and if the first six cycles are excluded, the average charge capacity fade is 0.11% per cycle (0.67% per hour).

Table 3.1 [Fe] ICP-OES Data

	central compartment (mM)	BPM (mM)	Acid-side electrolyte (mM)
Three-chamber (Fumasep 50 cycles)	0.0063 (±2.0%)	3.8 (±6.7%)	0.017 (±2.3%)
Three-chamber (Nafion 50 cycles)	0.35 (±1.6%)	7.9 (±3.8%)	0.013 (±2.4%)
Three-chamber (Nafion 3 cycles)	0.012 (±1.9%)	3.8 (±7.8%)	0.013 (±2.7%)
Two-chamber (50 cycles)	N/A	17 (±4.8%)	1.76 (±0.36%)

In order to understand the rapid performance decay of the two-chamber cell, experiments were performed in an H-cell in which reference electrodes were placed on either side of the BPM, enabling the potential drop across the membrane to be measured. A 1 M concentration of H_2SO_4 solution and 2

M KOH solution filled the compartments facing the CEL and AEL, respectively, and platinum electrodes were used to electrolyze these solutions, driving an ionic current through the membrane. Over the course of a single cycle of current steps (Fig. 3.4B), there was relatively little difference in transmembrane potential when redox molecules DSAQ and $K_4Fe(CN)_6$ were added to the acid and base solutions, respectively. However, when currents were applied to mirror charge cycling in the H-cell, there was a clear difference. The transmembrane potential remained constant with cycling in the "no molecules" case but rapidly decayed when the redox molecules were added (Fig. 3.4C). This experiment indicates that the primary effect of cycling is to degrade the performance of the BPM rather than to alter the compositions of the acidic and basic electrolyte solutions.

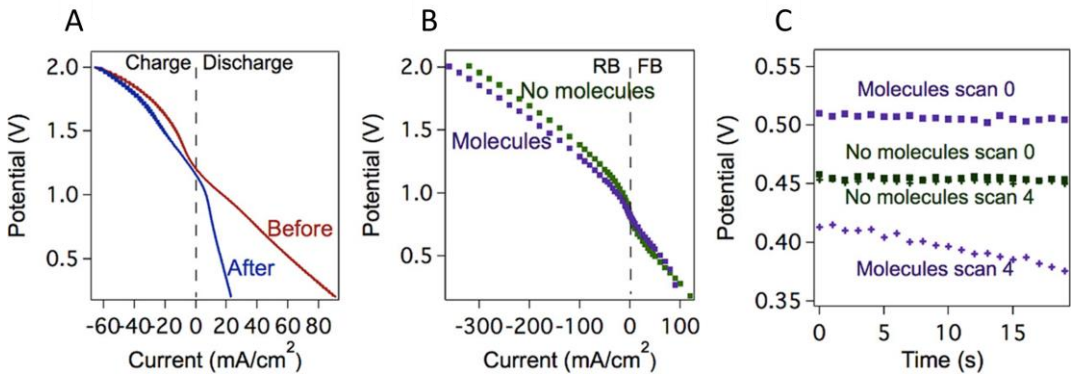

Figure 3.4. (A) Polarization curve of the two-chamber cell design before (red) and after (blue) cycling to failure. Here failure is defined as the decrease in charge and discharge capacity to zero. A scan rate of 100 mV/s was used. (B) *j–E* curve of the BPM in an H-Cell with 1 M H_2SO_4 on the negative side and 1 M KOH on the positive side without any additional redox molecules (green, "no molecules") and with >50 mM DSAQ in 1 M H_2SO_4 on the negative side and 50 mM $K_4Fe(CN)_6$ in 2 M KOH on the positive side (purple, "molecules"). (C) Potential decay at an applied forward bias of 60 mA/cm^2 of the redox molecule-containing H-cell (purple) and the H-cell without redox molecules (green) after no applied constant current (squares, "scan 0"), and after 4 rounds of 8 min cycling at +20

and −20 mA of applied current to mimic the charge and discharge cycles of the redox flow battery (crosses, “scan 4”).

Analysis of the electrolytes after the charge cycling of the three-chamber system reveals additional information about ferro-/ferricyanide exchange into the BPM and transport into the acidic compartment of the cell. Cyclic voltammetry shows a low concentration of ferrocyanide in the central chamber for both CEM types (Fig. 3.7). ICP-OES was used to obtain quantitative crossover data (Table 3.1).

Both Nafion and Fumasep CEMs allowed a small amount of leakage of iron into the central 5 M KOH chamber and the BPM, and in the case of the two-chamber cell, into the negative electrolyte after 50 charging cycles. Most notably, the crossover of iron to the acidic side of the cell was reduced by a factor of 100 or more in the three-chamber cell. The Fumasep CEM resulted in lower iron concentrations than the Nafion CEM in all environments except the acid electrolyte, where the two concentrations were comparable. This is likely due to a higher co-ion selectivity and thus slower leakage through the Fumasep membrane relative to Nafion. Nafion is known to contain water channels in its structure that lead to enhanced ion leakage.[20]

In the two-chamber design, the small amount of Fe crossover alone is not sufficient to account for the dramatic decrease in charge and discharge capacity upon cycling. The relative stability of the Coulombic efficiency (Fig. 3.3A) also argues against Fe crossover as the primary mechanism of capacity fading. For the capacity of the two-chamber system to decrease to zero by a crossover mechanism, the BPM and negative electrolyte chamber would need to contain ∼50 mM of the ferro-/ferricyanide couple. A more likely mechanism, which is consistent with all of the data, is the concentration and precipitation of ferro-/ferricyanide salts or their decomposition products in the BPM junction. Negatively charged $[Fe(CN)_6]^{3-/4-}$ ions can compete for anion exchange sites in the AEL of the BPM, so in the discharge cycle

(forward bias direction of the BPM), they are efficiently electromigrated to the junction region of the BPM. Their transport through the CEL of the BPM, via a leakage mechanism, is slower because the CEL has a high concentration of negative fixed charge. This leads to accumulation of iron compounds in the junction region. In contrast, in the three-chamber system, the AEL of the BPM is exposed to a much lower concentration of $[Fe(CN)_6]^{3-/4-}$ ions, especially in the case of the less permeable Fumasep CEM. This results in less buildup of iron species in the junction and also slower leakage through the CEL to the acidic electrolyte. By ICP-OES analysis, all three-chamber samples contain less Fe in the BPM after cycling than the two-chamber samples. This indicates slower accumulation of Fe-containing species in the BPM in the three-chamber experiment, and thus the membrane resistance remains relatively constant.

DSAQ leakage was investigated with BPMs of different CEL thicknesses in order to determine the effect of DSAQ leakage on membrane fouling. The general structure and fabrication[15] of these BPMs were the same, but the thickness of the CEL layer was varied by using different quantities (200, 300, 400, or 500 µL) of a 5 wt % sulfonated poly(ether ether ketone) (SPEEK) in DMF diluted to 1 mL total volume. Details of the dilutions and membrane thicknesses of these samples are given in Table 3.3. All BPMs were tested with a Nafion CEM and run for three cycles for the 200-, 300-, and 400-BPMs and 50 cycles for the 500-BPM. DSAQ crossover was apparent in both the 200-BPM and 300-BPM samples from UV−visible spectroscopy (Fig. 3.9) and a noticeable change in the color of the central chamber solution from colorless to pink (Fig. 3.8). From the UV-vis spectra (Fig. 3.9A), the concentration of DSAQ in the central chamber (Table 3.3) was found to decrease dramatically with increasing CEL thickness. The 400-BPM and 500-BPM samples showed no obvious color change, and UV−vis spectra showed no detectable absorbance at the 500 nm absorbance maximum of DSAQ. On the basis of a calibration curve of DSAQ in

5 M KOH (Fig. 3.9C), the 400-BPM and 500-BPM samples showed DSAQ concentrations in the central chamber below 0.006 mM.

Polarization curves were taken before and after charge cycling for all four BPMs (Fig. 3.10). The 200-BPM and 300-BPM have noticeable resistance changes in the forward bias direction of the polarization curves, whereas the 400-BPM and 500-BPM remained relatively constant with the 400-BPM displaying slightly higher resistivity after cycling. Because all four of these samples were tested in the three-chamber system, this apparent membrane fouling must be due to DSAQ-based changes in the BPM. In fact, in the 200-BPM case, DSAQ leakage was so substantial that a precipitate could be visually observed in the BPM upon charge cycling completion and disassembly of the cell (Fig. 3.8C). Notably, the slope of the polarization curves before charge cycling is similar across all four membrane types, indicating that while changing the thickness of the CEL has an extreme impact on DSAQ crossover, its impact on membrane resistivity is minimal (Fig. 3.10). So, on the basis of a qualitative analysis of solution color change, quantitative UV−vis, and a polarization curve analysis, we can conclude that increasing the CEL thickness in the BPM minimizes the degree of ion leakage across the acid−base RFB cell and thus minimizes membrane fouling of the BPM.

Conclusion

In conclusion, we have determined that the principal cause of poor capacity retention in the two-chamber acid−base RFB is membrane fouling that arises from ferro-/ferricyanide electromigration upon cycling. This process is not unexpected since anionic complexes can compete with hydroxide ions for sites in the AEL of the BPM. Additionally, we determined that DSAQ leakage can contribute to membrane fouling. Increasing the thickness of the CEL greatly attenuates the leakage of DSAQ, and adding a CEM and central alkaline chamber barrier between the positive electrolyte and the BPM also

dramatically reduces the ferro-/ferricyanide crossover rate, as quantified by ICP. Additionally, the third chamber enables the use of a highly alkaline environment on the AEL side of the BPM and eliminates the need for strongly alkaline conditions in the positive electrolyte environment. Thus, a highly positive redox couple that is unstable in strong base, Br_3^-/Br^-, could be used with a cross-membrane ΔpH of ∼14 to realize an OCV of 1.7 V.

We note that several challenges remain for BPM-based ARFBs to become competitive with more conventional ARFB designs and chemistries. First, while the crossover rate can be mitigated by using the three-chamber design and thicker CEL layers in the BPM, it does still occur at a measurable rate and therefore other strategies – e.g., slurry redox couples or more selective membranes – will be needed for realistic energy storage applications. Second, polarization of the BPM occurs at relatively low current density (∼20−30 mA/cm^2) because of slow catalysis of the water dissociation reaction in the BPM junction and slow electrode kinetics at carbon electrodes. Thus, improvements in these catalysts will be important for achieving high round-trip efficiency with BPM-based ARFBs. Third, the additional chamber and membrane of the three-chamber system add to the complexity and the total series resistance of the cell. From EIS (Fig. 3.11), under a 20 mA/cm^2 reverse bias the two-chamber system has a series resistance of approximately 2.3 Ω while the three-chamber system has a series resistance of approximately 4.1 Ω. Notably, a large portion of this added series resistance is likely due to poorer contact between the graphite flow fields and the porous carbon electrodes in the three-chamber system, as compared to the two-chamber system where the electrodes are tightly clamped between the flow fields and the membrane. Securing the electrode to the graphite flow fields with copper tape decreases the series resistance to 3.4 Ω. Further systematic improvements can be made to improve this contact and decrease the series resistance.

Supporting Information

Materials

Chemicals were purchased from Sigma Aldrich and used as received unless otherwise noted. Anion exchange membranes (Fumasep FAS-30), Nafion 212, Nafion 117, and cation exchange membranes (Fumasep FKS-30) were purchased from the Fuel Cell Store. Sulfonated poly(ethyl ethyl ketone) (SPEEK) was prepared following a previously reported method[26] and stored as a 5 wt% solution in DMF. Graphite oxide (GO) was prepared following a previously reported method.[27] Platinum wires (0.5 mm diameter, 99.95%) were obtained from Alfa Aesar. Ag/AgCl with 3 M NaCl filling solution reference electrodes were obtained from Microelectrode.

2,7 – Disulfonate-9,10-anthraquinone (DSAQ) was purchased from AK Scientific Inc and was passed through a cation exchange column loaded with 0.1 M HCl before drying to a yellow powder at 70 °C. Carbon paper (Sigracet GDL 39 AA) was purchased from the Fuel Cell Store and thermally treated at 400 °C for 24 hours in air before use. Toray Paper 120 was also purchased from the Fuel Cell Store and pretreated with acid following a previously reported procedure.[9] Briefly, electrodes were sonicated in isopropyl alcohol for 10 minutes and then soaked for 5 hours at 50 °C in a 3:1 volumetric mixture of sulfuric acid to nitric acid. Gasket material and tubing were purchased from McMaster Carr. The peristaltic pumps were purchased from MasterFlex (Cole-Parmer, No. 7553-80). The flow battery cell was purchased from Scribner (Redox Flow Cell Test Fixture).

BPM fabrication

BPMs were prepared by a slight modification of a previously reported procedure.[28] Briefly, the anion exchange membranes were cut into 3 cm x 3 cm squares and soaked in 1 M KOH for approximately 2 min. Upon soaking the membranes noticeably swelled and changed to a slightly yellow color. The

membranes were then thoroughly rinsed with water and secured to a clean glass slide with minimal amounts of Scotch tape. Approximately 1 mL of GO suspension (1 mg/mL) was dropped onto the membrane surface and left to stand for 20 min, after which the remaining GO was rinsed away with water and the AEM/GO membrane composite was dried using an air gun. The AEM/GO glass slide was then placed on a hot plate kept between 120-130 °C as 1 mL of a SPEEK solution (specific wt% values specified in Table 3.3) was air-sprayed on the exposed AEM/GO membrane. The newly prepared BPM was peeled off of the glass slide with the aid of water, and then thoroughly dried on a warm vacuum table for 20 min before sandwiching in aluminum foil and placing on a 165 °F hot press at 2000 psi for 30 min. The obtained BPM was stored in air before testing.

Electrochemical measurements

Cyclic voltammetry (CV) was conducted in specified aqueous electrolytes and concentrations. Platinum wires and Ag/AgCl were used as the working, counter, and reference electrodes. Scans were conducted using a PGSTAT302N (Metrohm, Autolab) instrument at 100 mV/s scan rate.

Polarization curves of the BPM were taken using a four-electrode design as previously reported.[28] The BPM was placed between the central chambers of an H-cell with a 1 cm x 1 cm exposed area. Two Ag/AgCl reference electrodes were placed on either side of the BPM using Haber-Luggin capillaries. An EZStat Pro Potentiostat-Galvanostat (NuVant Systems) was connected to the reference electrodes and used to monitor the cross-membrane potential. At either end of the H-cell platinum wires were employed as the working and counter electrodes. These electrodes were separated from the reference electrodes by AEMs and CEMs to minimize the influence of any electrochemical products generated at the surfaces of the driving electrodes. These platinum electrodes were connected to a DC power supply

(Agilent E3612), from which the current was supplied stepwise. 1 M H_2SO_4 was utilized on the negative side and 1 M KOH on the positive side as electrolytes unless otherwise noted.

Spectroscopic measurements

UV-vis measurements were taken on an Agilent Cary 60 UV-Vis instrument. Samples were held and run in disposable plastic cuvettes. Standards of potassium ferrocyanide and DSAQ were both made to be 0.50 mM in 5 M KOH and then diluted systematically in order to obtain a calibration curve.

Redox flow battery measurements

General Considerations: Two-chamber experiments utilized a flow battery design as detailed by Scribner (Redox Flow Cell Test Fixture), while three-chamber experiments utilized a flow battery design with either a PTFE (Fig. 3.5A) or a Sylagrad (Fig. 3.5B) central compartment. In three-chamber ferrocyanide-DSAQ batteries, 5 M KOH was used in the central chamber, and was purged with N_2 gas in order to reach higher alkalinity before incorporation into the battery. In three-chamber bromine-DSAQ batteries, 1 M KOH was utilized. Positive and negative electrolytes (and if specified the central 5 M KOH solution) were peristaltically pumped at a flow rate of ~30 mL/min. All measurements were conducted with the cell in an argon filled glove-bag at ambient temperature. PTFE Gasket material (McMaster, 9711k26) was used to separate and secure each component of the cell. Each gasket had a 1 cm x 1 cm window. One 1 cm x 1 cm electrode was used on both sides of the cell, and a 1 cm x 1 cm area of BPM (as well as Fumasep or Nafion membrane in the three-chamber design) was exposed.

All electrochemical measurements were conducted using an EZStat Pro Potentiostat-Galvanostat (NuVant Systems). Charge/discharge experiments were conducted by galvanostatic application of a 20 mA/cm^2 current with cutoff upper and lower potential limits of 1.75 V and 0.2 V for ferrocyanide-DSAQ

battery cycling, and at an applied current density of 10 mA/cm^2 with cutoff upper and lower potential limits of 2.27 V and 0.5 V as well as 20 mA/cm^2 with cutoff upper and lower potential limits of 2.3 V and 0.25 V for bromine-DSAQ battery cycling. Polarization curves were obtained after an initial complete charge at approximately 100% state of charge by application of a CV scan between 2 V and 0.2 V for the ferrocyanide-DSAQ battery and between 2.5 V and 0.2 V for the bromine-DSAQ battery at a scan rate of 100 mV/s.

Electrolyte compositions

Ferrocyanide-DSAQ two-chamber cycling and polarization: Typical experiments utilized a positive electrolyte composed of 50 mM potassium ferrocyanide in 2 M KOH (4 mL) and a negative electrolyte composed of >50 mM DSAQ in 1 M H_2SO_4 (4 mL). One 1 cm x 1 cm Sigracet carbon paper electrode was used on either side of the cell. A 500-BPM was used.

Ferrocyanide-DSAQ three-chamber cycling and polarization: Typical experiments utilized a positive electrolyte composed of 50 mM potassium ferrocyanide in 2 M KOH (4 mL) and a negative electrolyte composed of >50 mM DSAQ in 1 M H_2SO_4 (4 mL). Degassed 5 M KOH was used to fill the middle chamber. One 1 cm x 1 cm Sigracet carbon paper electrode was used on either side of the cell. A 500-BPM was used unless otherwise specified.

Bromine-DSAQ three-chamber cycling: Typical experiments utilized a positive electrolyte composed of 0.10 M Br_2, 1 M potassium bromide, and 0.1 M 6.5 pH phosphate buffer (8 mL). Negative electrolytes were composed of 50 mM DSAQ in 1 M H_2SO_4 (4 mL). 1 M KOH was used to fill the middle chamber. A Nafion 117 membrane was used to separate the central KOH chamber from the Br_2/KBr electrolyte chamber. One 1 cm x 1 cm acid treated Toray paper was used on either side of the cell. A 500-BPM was used. Some experiments (which resulted in rapid deterioration of the carbon paper electrode)

substituted a pH 9.8 borate buffer for the phosphate buffer in the Br_2/KBr electrolyte chamber following a previously reported electrolyte system. [8]

Bromine-DSAQ three-chamber polarization: Typical experiments utilized a positive electrolyte composed of 0.1 M Br_2, 0.4 M potassium bromide, and 0.1 M of a 6.5 pH phosphate buffer (4 mL). Negative electrolytes were composed of 0.1 M >DSAQ in 1 M H_2SO_4 (4 mL). 1 M KOH was used to fill the middle chamber. A Nafion 212 membrane was used to separate the central KOH chamber from the Br_2/KBr electrolyte chamber. One 1 cm x 1 cm Sigracet carbon paper electrode was used on either side of the cell. A 500-BPM was used.

The following electrochemical reactions take place in the redox flow battery (RFB):

Ferrocyanide/DSAQ RFB

Positive (charge): $FeCN_6^{4-} \rightarrow FeCN_6^{3-} + e^-$

Negative (charge): $DSAQ^{2-} + 2H^+ + 2e^- \rightarrow H_2DSAQ^{2-}$

Bromine/DSAQ RFB

Positive (charge): $3Br^- \rightarrow Br_3^- + 2e^-$

Negative (charge): $DSAQ^{2-} + 2H^+ + 2e^- \rightarrow H_2DSAQ^{2-}$

<u>ICP measurements and data analysis</u>

Ion concentrations in BPMs were determined by first soaking the BPM after charge cycling in 5 mL of 1 M NaCl for at least one week. The concentration as determined by ICP was then normalized to an assumed area and thickness of 1 cm x 1 cm x 60 µm. This available volume assumes that the entire

exposed membrane can potentially hold ions, and thus does not consider volume exclusion by the polymeric backbones that make up the membrane. The ICP standard regression was composed of 100, 500, 1000, and 10,000 ppb Fe and K standards with a correlation coefficient of 0.99997. Qualitative measurements of K concentrations in the negative electrolyte and absorbed in the BPM after cycling are found in Table 3.2.

Based on relative Fe and K crossover concentrations, we can explain the detailed crossover mechanism of ferrocyanide in the two-chamber design as follows. In the positive chamber, ferrocyanide exists in a variety of ion-paired forms ($K_xFe(CN)_6^{(-3-x)}$ and $K_yFe(CN)_6^{(-4-y)}$ where x=0-3, and y=0-4). As such, for every iron atom, up to four potassium ions can be associated with the complex. Thus, when ferro/ferricyanide undergoes migration through the AEL towards the AEL/CEL interface, ion-paired potassium ions can dissociate from ferro/ferricyanide ions and exchange into the CEL, possibly explaining the high potassium concentration in the BPM relative to the lower iron concentration. Then, anionic or ion-paired potassium ferro/ferricyanide complexes may continue through the CEL via a leakage mechanism. Alternatively, under reverse bias, the potassium ions can dissociate from ferro/ferricyanide at the AEL/CEL interface and pass through the CEL by a more efficient electromigration process. Thus, potassium and iron can be found in both the BPM and in the negative electrolyte, but the potassium is transported more efficiently and is detected at a far higher concentration. Under forward bias, the accumulation of ferro/ferricyanide ions at the relatively acidic AEL/CEL interface can result in decomposition and/or precipitation of the complexes and an increase in the series resistance of the BPM.

Comparing the three-chamber and the two-chamber 500-BPM designs, more iron is observed in the two-chamber design. Assuming the transport mechanisms and failure modes described above are

operative, the same logic can be applied to compare the three-chamber and the two-chamber designs. That is, when anionic Fe-containing complexes are present in high concentration in direct contact with the AEL of the BPM, they compete with OH^- for sites in the AEL. When these complexes are not in direct contact with the AEL, far less ferro/ferricyanide transport occurs. Looking specifically at the Nafion three-chamber design, the concentration of both potassium and iron is initially lower after six charge cycles than after the full 50 cycles. This difference is more starkly apparent for the iron concentration. In the three-chamber design the BPM is directly facing highly concentrated KOH. Consequently, potassium has far more access to the BPM than iron, and so an equilibrium between the potassium in the central chamber and the potassium in the BPM is reached early on, whereas very little iron is initially or ever in direct contact with the BPM via the central chamber, explaining the difference in iron concentration between the 3 and 50 cycles of the Nafion three-chamber design.

Concentrations of iron in Table 3.1 were averages from the 259.941, 238.204, and 239.562 nm Fe wavelengths.

Bromine RFB cycling

Charge cycling data of the bromine species is depicted in Figure 3.12. Bromine based RFB systems are known to experience rapid crossover of neutral bromine or ion-paired bromides across Nafion or other CEMs.[9] As depicted in Figure 3.12, the system reported here experiences similar crossover over a 6-hour cycle experiment, especially at higher applied current densities (i.e. the 20 mA system depicts more capacity fade than the 10 mA system because following Faraday's Law, higher applied current allows for electrochemical processes to occur faster). Once the bromine molecules or tribromide ions cross over into the middle KOH chamber, the bromate ions formed by alkaline disproportionation can exchange with the more hydrophilic hydroxide ions on the AEL, chemically attacking the membrane and

decreasing the hydroxide conductivity of the BPM over time. Methods used to partially counter this crossover effect as well as electrode destruction are discussed below.

Notably, a few considerations must be made when charge cycling a bromine RFB, all of which were considered in the construction of our system. First, elemental bromine is known to intercalate into graphite.[29] Additionally, bromine is strongly oxidizing and destructive to carbon electrodes.[30] We found that under alkaline conditions (e.g. borate buffer at pH~9.8[8]), bromine appears to react with the carbon paper electrode (a graphitic material) to an extreme extent and ultimately disintegrates the electrode (Fig 3.12C). This destruction manifests itself in increasing resistivity in both the forward and reverse bias directions. Investigations into other electrode materials such as glassy carbon may prove to be beneficial in alleviating this problem. However, this problem is mitigated by using a phosphate buffer to create a nearly pH neutral acidic environment. The high concentration of potassium ions in both the central and positive electrolyte chambers results in a high transference number for potassium relative to other cations, maintaining the pH difference upon cycling. Such pH gradients have previously been successfully maintained using Nafion 117 membranes.[12]

Neutral bromine (Br_2) can easily leak through Nafion membranes and thus can cross the CEM into the central electrolyte chamber.[9] While such crossover does occur in the three-chamber system, the bromine/tribromide equilibrium can be exploited to lessen crossover and BPM degradation. Anionic bromide or tribromide species must ion-pair with a cation in order to cross over the CEM. Thus, future investigations into different cation pairs may help to address the bromine crossover problem. Additionally, tribromide and bromide salts are both very soluble in aqueous media, so membrane fouling due to bromide precipitation at the BPM AEL/CEL interface is unlikely, and also is not apparent in our experiments (Fig. 3.12E). In Figure 3.12E, a BPM that was removed from the 3-chamber system after

cycling was placed in an H-cell with fresh 1 M KOH, allowing for the AEL to ion exchange some bromide with hydroxide ions. In this case, we measure a cross-membrane potential that is not indicative of membrane fouling, indicating that rather than a destructive precipitation-based mechanism, the failure of the bromine system is due to ion exchange. Also, in the case of the borate buffered system (0.1 M borate buffer, 0.1 M Br_2, 0.4 M KBr vs. 0.1 M DSAQ, 1 M H_2SO_4), after the completion of the cycling experiment, electrode destruction is seen only on the positive side (Fig. 3.12D). If a significant amount of bromine were to fully cross over into the negative electrolyte chamber, negative electrode destruction might also be apparent. For these reasons, we can conclude that the mechanism of failure of the bromine battery is the ion exchange of bromate ions into the anion exchange membrane and the subsequential decrease in the BPM's hydroxide ion conductivity.

In an attempt to minimize capacity fade due to bromine crossover we utilized an excess of negative electrolyte (DSAQ) relative to the positive electrolyte (bromine). In addition, because the primary crossover mechanism involves neutral bromine passing through the CEM, lowering the concentration of neutral bromine should minimize the crossover. Neutral bromine combines with bromide ions according to the equilibrium:

$$Br_2 + Br^- \rightleftharpoons Br_3^-$$

Accordingly, increasing the concentration of bromide in the solution should lower the concentration of neutral bromine. Following these considerations, we cycled the bromine containing battery with a Nafion 117 membrane, a fourfold excess of bromine relative to DSAQ, and a high concentration (1 M) of bromide ions. Finally, somewhat more durable Toray paper electrodes were used instead of thermally

treated carbon electrodes. These modifications gave a few hours of stable cycling of the bromine-KOH-DSAQ three-chamber redox flow battery at a 10 mA/cm^2 current density (Fig. 3.12A).

A few other experiments were conducted to address the apparent bromide crossover problem, but these modifications did not appear to have any significant effect. First, other CEM membrane types including a homemade 50 µm SPEEK membrane and the previously used 30 µm Fumasep membrane were used but gave similar results. Second, using sodium as the cation rather than potassium also showed similar results.

Supporting images

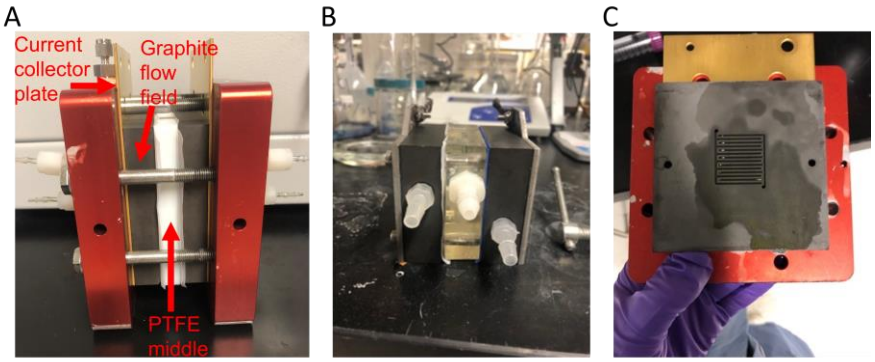

Figure 3.5. (A) PTFE three-chamber design (B) Sylagard three-chamber design (C) excess electrolyte left over on graphitic flow field after cycling.

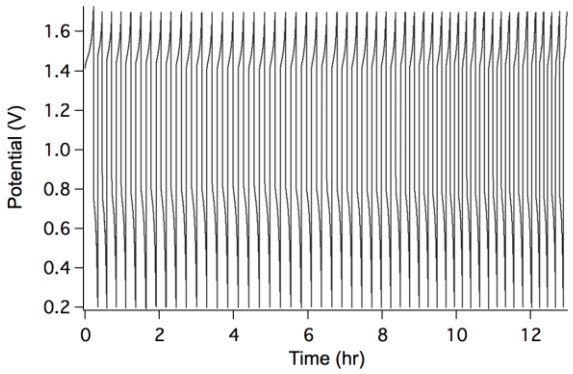

Figure 3.6. Charge cycling of the PTFE three-chamber design using Nafion as the CEM. The cell is composed of 50 mM ferrocyanide in 2 M KOH (positive), 5 M KOH (middle), and >50 mM DSAQ in 1 M H_2SO_4 (positive).

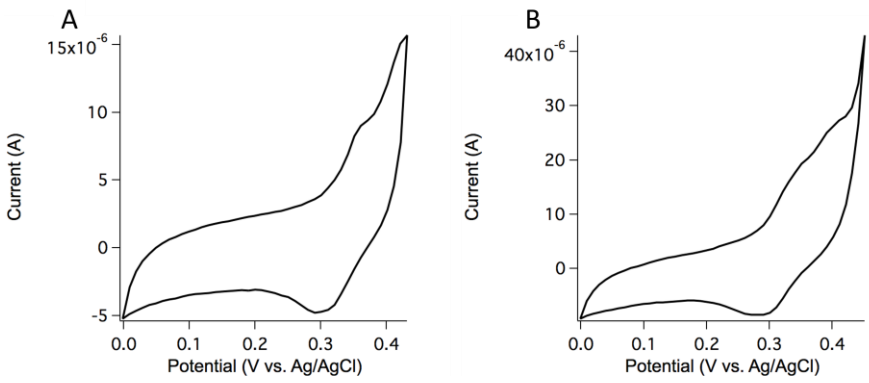

Figure 3.7. Cyclic voltammograms of the ferrocyanide region of the (A) Fumasep and (B) Nafion three-chamber design middle chamber after charge cycling at ±20 mA. CVs are run with glassy carbon, platinum, and Ag/AgCl working, counter, and reference electrodes respectively. A scan rate of 100 mV/s was used.

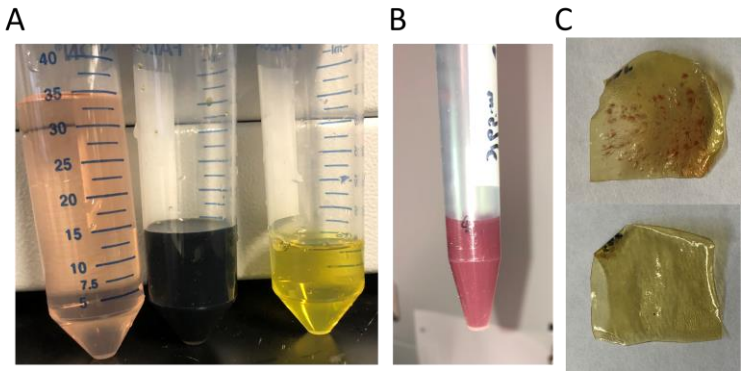

Figure 3.8. (A) Electrolyte after a 300-BPM three-chamber experiment. Left (pink) is the central 5M KOH, middle (black) is the negative electrolyte, right (yellow) is the positive electrolyte. (B) Electrolyte after a 200-BPM three-chamber experiment from the central chamber. (C) BPMs after charge cycling for the (top) 200-BPM and (bottom) 500-BPM.

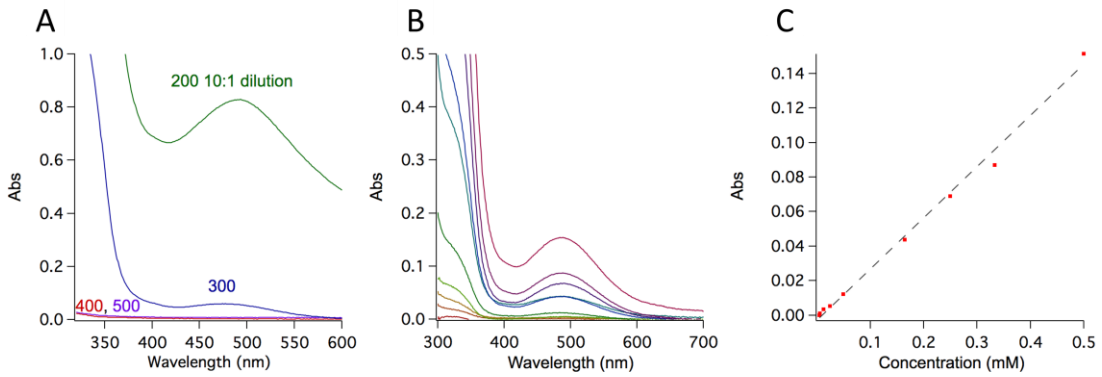

Figure 3.9. (A) UV-Vis data of the DSAQ absorbance region. of the 200 (green), 300 (blue), 400 (red), and 500 (purple) BPMs. Note that the 200-BPM sample had to be diluted with 10 mL of 5 M KOH in order to obtain a readable absorbance signal. (b) UV-Vis calibration of DSAQ from 0.5 mM to 0.005 mM in 5 M KOH. Nonzero absorbance values were found for concentrations as low as 0.00625 mM. Absorbance vs wavelength across all concentrations is plotted. (B) concentration vs absorbance for peak absorbance value (found at wavelength 484 nm). The trendline has the linear form y=3.3856x+0.0095 with a corresponding r-squared value of 0.9938

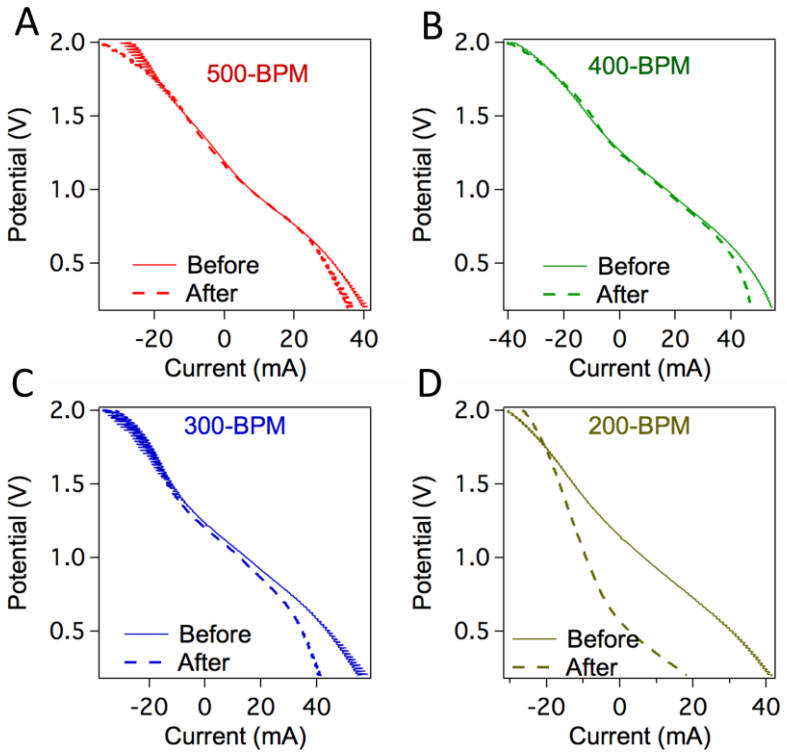

Figure 3.10. Polarization curves of the (A) 500-BPM, (B) 400-BPM, (C) 300-BPM, and (D) 200- BPM. Data was collected before (solid line) and after (dashed line) charge cycling. Positive current represents the forward bias (discharge). Cells are composed of 50 mM ferrocyanide in 2 M KOH (positive), 5 M KOH (middle), and >50 mM DSAQ in 1 M H_2SO_4 (positive). A scan rate of 100 mV/s was used.

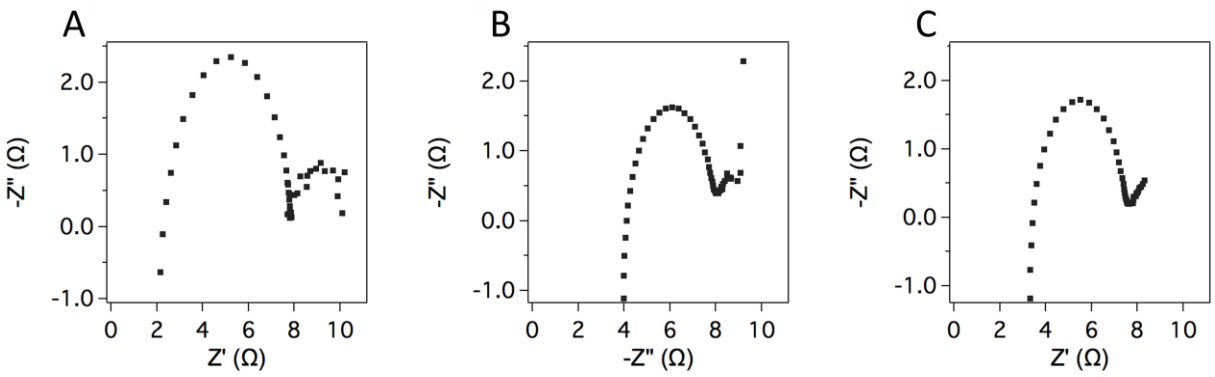

Figure 3.11. EIS data of various acid-base RFB systems. Cells are composed of 50 mM ferrocyanide in 2 M KOH (positive), 5 M KOH (middle), and >50 mM DSAQ in 1 M H_2SO_4 (positive). All scans taken at an applied DC of 20 mA from 10000 Hz to 1 Hz. (A) Two-chamber system (B) three-chamber system with 5 M KOH middle chamber (C) three-chamber system with 5 M KOH and copper tape used to secure carbon paper electrodes directly to the graphite flow fields.

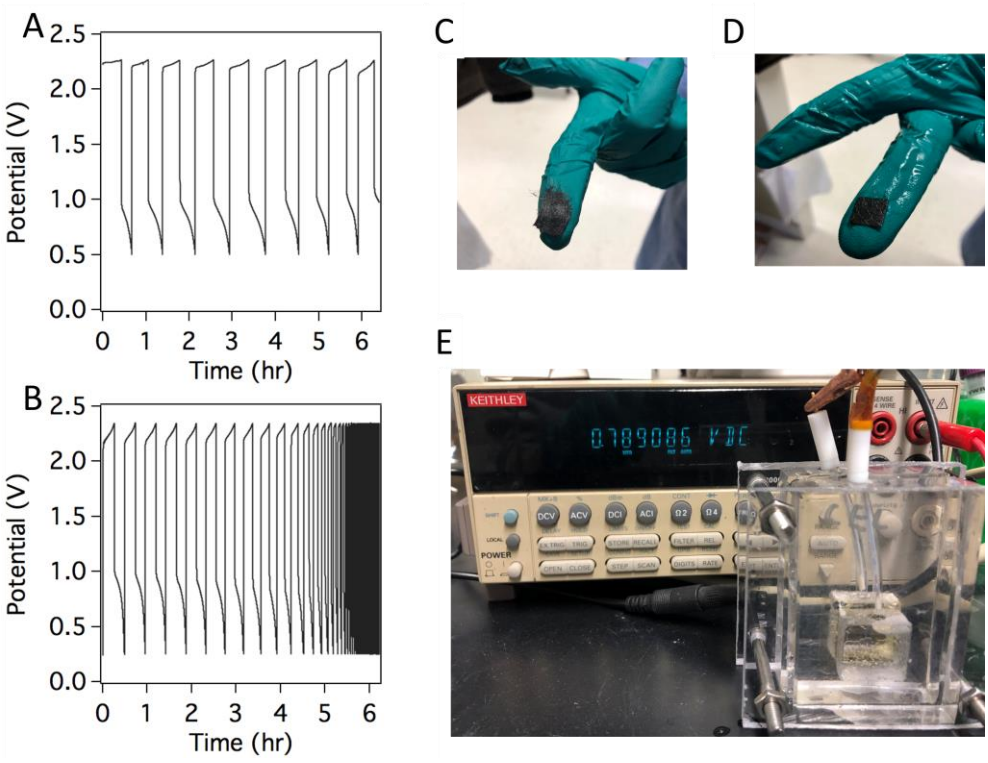

Figure 3.12. Charge cycling at (A) ±10 mA and (B) ±20 mA of the three-chamber bromine-DSAQ redox flow battery. For both experiments, the cell is composed of 0.1 M bromine and 1 M potassium bromide in 0.1 M of a pH ~6.5 phosphate buffer (positive), 1 M KOH (middle), and 50 mM DSAQ in 1 M H_2SO_4 (positive). Electrodes from the borate buffered bromine-DSAQ three-chamber system cycling. (C) positive electrolyte (D) negative electrolyte. (E) Cross-membrane potential of BPM after charge cycling with bromine. 1 M H_2SO_4 is on the negative side and 1 M KOH is on the positive side. This value falls within the typical range of seen cross-membrane potentials under such conditions, and thus does not show signs of membrane fouling.

Supporting tables

Table 3.2. K ICP data

	BPM (mM)	Acid-side electrolyte (mM)
Three-chamber (Fumasep 50 cycles)	6.2	0.044
Three-chamber (Nafion 50 cycles)	4.3	0.052
Three-chamber (Nafion 3 cycles)	3.6	0.0043
Two-chamber (50 cycles)	4.4	0.084

The actual values of potassium are qualitative as they are well beyond the calibration range of the ICP-OES. These numbers are more indicative of there being a large concentration of potassium than of any comparative value between the three-chamber and two-chamber designs.

Table 3.3. CEL thickness investigation

	Wt% CEL solution	BPM thickness	Middle [DSAQ] after cycle
200-BPM	1%	51 µm (0.0020 in)	2.4 mM
300-BPM	1.5%	58 µm (0.0023 in)	0.015 mM
400-BPM	2%	64 µm (0.0025 in)	N/A
500-BPM	2.5%	76 µm (0.0030 in)	N/A

The total thickness of the BPM was estimated using a caliper ranging from 1 to 0.0001 in in measurable distance. As different wt% solutions and thus different amounts of organic solvent were used for the different BPM types, the exact thickness of the CEL layer cannot be accurately estimated from the total BPM thickness. Organic solvent can etch away parts of the AEL base, so while the starting thickness for all BPMs is a 30 µm AEL, the AEL thickness once incorporated into the BPM may vary as a function of CEL wt% in solution. 200, 300, and 400-BPM samples were cycled for approximately 3 cycles while the 500-BPM was cycled for 50 cycles

References

(1) Winsberg, J.; Hagemann, T.; Janoschka, T.; Hager, M. D.; Schubert, U. S. Redox-Flow Batteries: From Metals to Organic Redox-Active Materials. *Angew. Chem., Int. Ed*. **2017**, 56, 686–711.

(2) Chen, H. N.; Cong, G. T.; Lu, Y. C. Recent progress in organic redox flow batteries: Active materials, electrolytes and membranes. *J. Energy Chem*. **2018**, 27, 1304–1325.

(3) Li, L. Y.; et al. A Stable Vanadium Redox-Flow Battery with High Energy Density for Large-Scale Energy Storage. *Adv. Energy Mater*. **2011**, 1, 394–400.

(4) Lai, Q. Z.; Zhang, H. M.; Li, X. F.; Zhang, L. Q.; Cheng, Y. H. A novel single flow zinc-bromine battery with improved energy density. *J. Power Sources* **2013,** 235, 1–4.

(5) Fan, F. Y.; et al. Polysulfide Flow Batteries Enabled by Percolating Nanoscale Conductor Networks. *Nano Lett*. **2014**, 14, 2210–2218.

(6) Er, S.; Suh, C.; Marshak, M. P.; Aspuru-Guzik, A. Computational design of molecules for an all-quinone redox flow battery. *Chem. Sci*. **2015**, 6, 885–893.

(7) Son, E. J.; Kim, J. H.; Kim, K.; Park, C. B. Quinone and its derivatives for energy harvesting and storage materials. *J. Mater. Chem. A* **2016**, 4, 11179–11202.

(8) Robb, B. H.; Farrell, J. M.; Marshak, M. P. Chelated Chromium Electrolyte Enabling High-Voltage Aqueous Flow Batteries. *Joule* **2019**, 3, 2503–2512.

(9) Huskinson, B.; et al. A metal-free organic-inorganic aqueous flow battery. *Nature* **2014**, 505, 195–198.

(10) Jin, S. J.; et al. Near Neutral pH Redox Flow Battery with Low Permeability and Long-Lifetime Phosphonated Viologen Active Species. *Adv. Energy Mater.* **2020**, 10, 2000100.

(11) Lin, K. X.; et al. Alkaline quinone flow battery. *Science* **2015**, 349, 1529–1532.

(12) Khataee, A.; Wedege, K.; Drazevic, E.; Bentien, A. Differential pH as a method for increasing cell potential in organic aqueous flow batteries. *J. Mater. Chem. A* **2017**, 5, 21875–21882.

(13) Luo, T.; Abdu, S.; Wessling, M. Selectivity of ion exchange membranes: A review. *J. Membr. Sci.* **2018**, 555, 429–454.

(14) Tomiyasu, H.; Shikata, H.; Takao, K.; Asanuma, N.; Taruta, S.; Park, Y.-Y.; et al. An aqueous electrolyte of the widest potential window and its superior capability for capacitors. *Sci. Rep.* **2017**, 7, 45048.

(15) Yan, Z. F.; et al. High-Voltage Aqueous Redox Flow Batteries Enabled by Catalyzed Water Dissociation and Acid-Base Neutralization in Bipolar Membranes. *ACS Cent. Sci.* **2021**, 7, 1028–1035.

(16) Giesbrecht, P. K.; Freund, M. S. Recent Advances in Bipolar Membrane Design and Applications. *Chem. Mater.* **2020**, 32, 8060–8090.

(17) Parnamae, R.; Mareev, S.; Nikonenko, V.; Melnikov, S.; Sheldeshov, N.; Zabolotskii, V.; Hamelers, H.V.M.; Tedesco, M.; et al. Bipolar membranes: A review on principles, latest developments, and applications. *J. Membr. Sci*. **2021**, 617, 118538.

(18) Donnan, F. G. Theory of membrane equilibria and membrane potentials in the presence of non-dialyzing electrolytes. *J. Membr. Sci.* **1995**, 100, 45–55.

(19) Li, Y. G. C.; et al. Bipolar Membranes Inhibit Product Crossover in CO2 Electrolysis. *Cells. Adv. Sustain. Syst.* **2018**, 2, 1700187.

(20) De Porcellinis, D.; et al. Communication-Sulfonated Poly(ether ether ketone) as Cation Exchange Membrane for Alkaline Redox Flow Batteries. *J. Electrochem. Soc.* **2018**, 165, A1137–A1139.

(21) Li, X.; et al. Symmetry-breaking design of an organic iron complex catholyte for a long cyclability aqueous organic redox flow battery. *Nat. Energy* **2021**, 6, 873–881.

(22) Luo, J.; et al. Unraveling pH dependent cycling stability of ferricyanide/ferrocyanide in redox flow batteries. *Nano Energy* **2017**, 42, 215–221.

(23) Paez, T.; Martinez-Cuezva, A.; Palma, J.; Ventosa, E. Revisiting the cycling stability of ferrocyanide in alkaline media for redox flow batteries. *J. Power Sources* **2020**, 471, 228453.

(24) Park, M.; et al. A High Voltage Aqueous Zinc-Organic Hybrid Flow Battery. *Adv. Energy Mater*. **2019**, 9, 1900694.

(25) Gong, K.; et al. A zinc-iron redox-flow battery under $100 perkW h of system capital cost. *Energy Environ. Sci.* **2015**, 8, 2941–2945.

(26) Shen, C.H.; Wycisk, R.; Pintauro, P. N. High performance electrospun bipolar membrane with a 3D junction. *Energy Environ. Sci.* **2017**, 10, 1435-1442.

(27) Kovtyukhova, N. I.; Ollivier, P. J.; Martin, B. R.; Mallouk, T. E.; Chizhik, S. A.; Buzaneva, E. V.; Gorchinskiy, A. D. Layer-by-layer assembly of ultrathin composite films from micronsized graphite oxide sheets and polycations. *Chem. Mater.* **1999**, 11, 771-778.

(28) Yan, Z. F.; Zhu, L.; Li, Y. G. C.; Wycisk, R. J.; Pintauro, P. N.; Hickner, M. A.; Mallouk, T. E. The balance of electric field and interfacial catalysis in promoting water dissociation in bipolar membranes. *Energy Environ. Sci.* **2018**, 11, 2235-2245.

(29) Gaier, J. R.; Ditmars, N. F.; Dillon, A. R. Aqueous electrochemical intercalation of bromine into graphite fibers. *Carbon* **2005**, 43, 189-193.

(30) Cho, K. T.; Tucker, M. C.; Ding, M.; Ridgway, P.; Battaglia, V. S.; Srinivasan, V.; Weber, A. Z. Cyclic Performance Analysis of Hydrogen/Bromine Flow Batteries for Grid-Scale Energy Storage. *ChemPlusChem* **2015**, 80, 402-411.

CHAPTER 4: FAST OUTER-SPHERE ELECTRON TRANSFER AND HIGH SPECIFIC CAPACITANCE AT COVALENTLY MODIFIED CARBON ELECTRODES

This chapter was previously published as Metlay, A.S.; Chyi, B.; Sheehan, C.J.; Shallenberger, J.R.; Mallouk, T.E. *J. Am. Chem. Soc.* **2024**, doi.org/10/1021/jacs.4c04088. It is reproduced with permission, copyright 2024, American Chemical Society. I was the primary author and conducted the majority of the experimental work and manuscript writing.

Abstract

Carbon electrodes typically display sluggish electron transfer kinetics due to the adsorption of adventitious molecules that effectively insulate the surface. Here, we describe a method for rendering graphitic carbon electrodes permanently hydrophilic by functionalization with 4-(diazonium)benzenesulfonic acid. In aqueous electrolytes, these hydrophilic carbon electrodes exhibit metal-like specific capacitance (~40 μF/cm^2) as measured by cyclic voltammetry, suggesting a change in the double-layer structure at the carbon surface. Additionally, the modified electrodes show fast charge transfer kinetics to outer-sphere one-electron redox couples such as ferro/ferricyanide as well as improved electron transfer kinetics in alkaline aqueous redox flow batteries.

Introduction

The electronic conductivity of carbon and its relative inertness in aqueous electrochemical systems has made it the electrode material of choice for a multitude of uses that include bioanalysis,[1-8] electrosynthesis,[9-13] separations,[14] and electrochemical energy conversion.[15-19] However, the sluggish charge-transfer kinetics of carbon electrodes in aqueous media limits their performance in these

applications. Noble metals such as platinum generally provide faster electrode kinetics, but they are prone to fouling, they catalyze side reactions such as hydrogen and oxygen evolution, and they are expensive. Thus, understanding and controlling the kinetics of charge transfer at the surface of carbon electrodes has been a long-standing challenge in the electrochemical community.

Early experiments by McCreery and co-workers suggested that the surface chemistry of carbon was the principal cause of its slow electron transfer kinetics.[20] They showed that *in situ* pulsed laser activation dramatically increased the double-layer capacitance and heterogeneous charge transfer rate between glassy carbon electrodes and ascorbate, dopamine, and ferricyanide in aqueous solutions. However, the laser activation effect was temporary as electron transfer rates decayed over a period of 20-30 minutes.[20] These effects were attributed to the adsorption of contaminants onto the hydrophobic carbon surface. Later research by Liu, et al. showed that UV-ozone cleaning temporarily removed air- or water-borne hydrocarbon contaminants from the surfaces of graphene and highly ordered pyrolytic graphite (HOPG).[21-23] The newly hydrophilic carbon surfaces showed enhanced electron transfer kinetics but again became hydrophobic and kinetically slow as adventitious molecules re-adsorbed to the carbon surface. Other strategies for activating carbon electrodes include anodic pulsing[24] and heating in air,[25] but in these cases the improvement in electron transfer kinetics is again transitory.

Much research has been devoted to characterizing[26-28] or improving[25, 29, 30] the charge transfer kinetics of carbon electrodes. However, in general these studies do not couple the two ideas, either introducing a method of characterization without a permanent solution or providing a temporary solution without a molecular-level investigation into the enhanced capacitance or change in surface chemistry. Thus, there remains no durable solution to the problem of carbon electrode electrochemistry.

Here we describe a simple and convenient covalent modification scheme that imparts hydrophilicity to graphitic carbon surfaces via an ambient temperature reaction with 4-(diazonium)benzenesulfonic acid, which is generated *in situ* by diazotization of sulfanilic acid. An investigation of the surface chemistry confirms the chemical functionalization of the carbon surface and achieves durably enhanced capacitance and kinetics of the modified carbon electrodes.

Results

The functionalization of graphitic electrode materials and HOPG with 4-(diazonium)benzenesulfonic acid was achieved by following a method previously developed for carbon nanoparticles,[31, 32] as detailed in Supporting Information (Fig. 4.1). Briefly, 4-(diazonium)benzenesulfonic acid was generated *in situ* by reacting sulfanilic acid with aqueous sodium nitrite and HCl. The electrodes were immersed in this solution overnight and then rinsed with hot ethanol.

Figure 4.1. Cartoon depiction of the functionalization of a graphitic surface with 4-(diazonium)benzenesulfonic acid (red spheres). Adventitious hydrophobic molecules (depicted as green goop) cover the hydrophobic surface prior to functionalization. Covalent modification with molecules bearing negatively charged sulfonate groups dramatically lowers the surface coverage of the hydrophobic molecules at both graphitic edge and basal plane sites.

X-ray photoelectron spectra (XPS) confirm the presence of sulfur-containing groups on the carbon surface following functionalization (Table 4.1, Fig. 4.7,8). XPS acquired with modified HOPG samples shows the presence of sulfur at both edge and basal plane sites. The density of sulfur-containing groups is about two times higher on the edge sites, suggesting that graphitic edge or defect sites are more readily modified. XPS of both carbon paper and HOPG samples also show the presence of nitrogen after functionalization. However, the N:S atomic ratios are approximately 0.6:1 and 0.3:1 at HOPG basal plane and edge sites, respectively, indicating that while some functionalization may occur through electrophilic azo coupling to graphite, the reaction primarily involves coupling between the graphitic surface and phenylsulfonate radicals that are derived from the azide salt. Fitting of the sulfur spectra shows two chemically distinct components, which may reflect the different surface species that result from azo and radical coupling.

Surface wetting and electrochemical experiments were carried out to probe the changes in hydrophilicity[21] and heterogeneous electron transfer kinetics[20, 33] following functionalization (Fig. 4.2). Water droplet contact and absorption were recorded for carbon paper electrodes as purchased, after a 400°C thermal treatment that is typical for electrodes used in electrochemical devices such as redox flow batteries,[34] and after functionalization with 4-(diazonium)benzenesulfonic acid (Fig. 4.2B-D). Both the thermal treatment and chemical functionalization result in a marked increase in hydrophilicity relative to the as-purchased sample. Based on the timescale of water absorption, the chemically modified sample is more hydrophilic than the thermally treated sample. The chemically modified samples remained hydrophilic over long periods of time. In UV/O_3 treatment experiments reported by Liu et al., the improvements in hydrophilicity were temporary, with carbon electrodes becoming hydrophobic within minutes.[21] In contrast, the water contact experiments here on chemically modified electrodes were performed 28 days after functionalization with 4-(diazonium)benzenesulfonic acid, and

30 days after thermal treatment, showing long term retention of hydrophilicity. These results are in nice agreement with similar water contact experiments reported for HOPG basal plane sites (Fig. 4.9A,B).

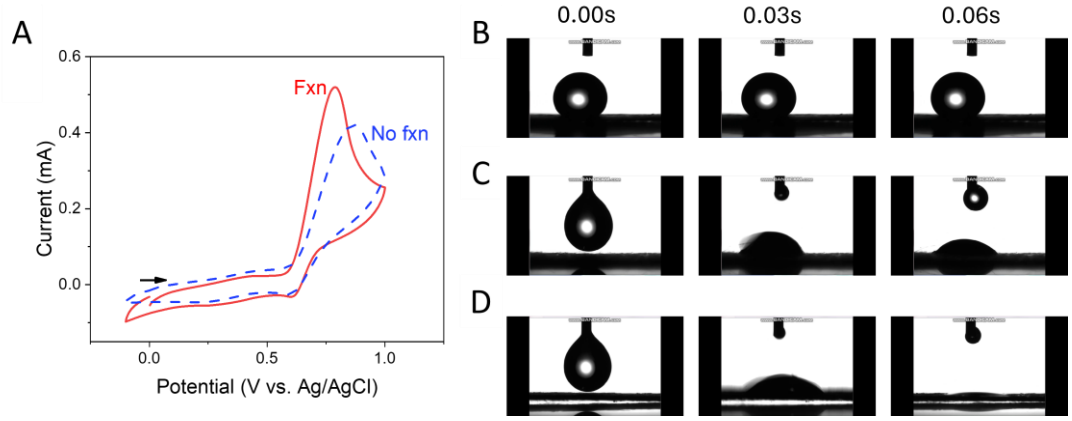

Figure 4.2. (A) Cyclic voltammetry of 3 mM acetaminophen in pH 2.2 citric acid solution at 40 mV/s scan rate using freshly alumina slurry polished unmodified (blue dashed line "No fxn") and modified graphitic rod electrodes (red solid line "Fxn"), the latter CVs were acquired ~5 hours after the functionalization step. Time-dependent water contact and adsorption photos of water droplets on (B) as-purchased Sigracet 39AA carbon paper, (C) thermally treated carbon paper exposed to air for 30 days, and (D) modified carbon paper exposed to air for 28 days.

The cyclic voltammetry of acetaminophen at a graphite rod electrode was recorded before and after treatment with 4-(diazonium)benzenesulfonic acid (Fig. 4.2A). The oxidation of acetaminophen is known to follow an ECE mechanism, in which the initial electron transfer step is followed by proton transfer, and the reaction is irreversible under the conditions of the experiment.[33] The cathodic shift of the anodic wave at the modified carbon electrode is comparable to the results obtained by McCreery, et al. using laser activation and can be attributed to acceleration of the initial electron transfer step.[20] In contrast to the laser activation experiments in which this effect is transitory, fast electron transfer was observed hours after chemical functionalization. The chemical stability of the functionalized electrodes in an

alkaline electrolyte is demonstrated over a 24-hour period of exposure by cyclic voltammetry in Figure 4.9C.

To quantify the changes in the redox kinetics of the modified electrodes, the Nicholson method for quasi-reversible systems[35] was applied to the cyclic voltammetry of a one-electron redox couple (ferro/ferricyanide) (Fig. 4.3,10). In the Nicholson method, the potential difference between the anodic and cathodic peaks is used to determine the dimensionless parameter Ψ across a range of scan rates. Ψ is plotted against $(\pi Dfv)^{-1/2}$, where D is the diffusion coefficient of ferricyanide, here taken as 6.7×10^{-6} $cm^2\ s^{-1}$,[26, 36] f is F/RT, and v is the scan rate in V/s. The slope of the linear fit across the range of scan rates is equal to the heterogeneous kinetic rate constant k^0. Based on this analysis, graphitic rod electrodes modified with 4-(diazonium)benzenesulfonic acid show a nearly fivefold increase in k^0 relative to unmodified electrodes. Notably, k^0 for the modified graphite electrode (0.02 cm/s) is approximately one fifth the value measured for macroscopic (0.2 mm diameter) Pt electrodes in aqueous sodium chloride solution.[37]

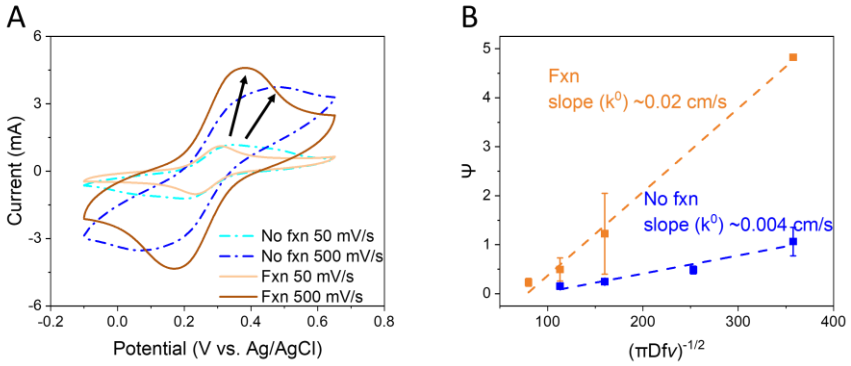

Figure 4.3. (A) Cyclic voltammetry of 10 mM potassium ferricyanide in 1 M aqueous potassium hydroxide solution at 50 and 500 mV/s scan rates, comparing unmodified (blue dashed line) and modified (orange solid lines) graphitic rod electrodes. (B) Nicholson plot of the scan rate-dependent parameter Ψ derived from the difference between

anodic and cathodic cyclic voltametric peak potentials. Averaged data and error bars represent experiments run on multiple electrodes.

Functionalization of the carbon electrode surface also leads to a marked increase in their specific capacitance in aqueous media (Fig. 4.4). Cyclic voltametric experiments[38] were carried out to measure the double layer capacitance (C_{dl}), electrochemically active surface area (ECSA), and specific capacitance (C_s) of modified and unfunctionalized electrodes in 1 M aqueous KOH solutions. Here, C_{dl} was obtained by plotting the difference between anodic and cathodic currents divided by two vs. scan rate at a specified potential (Fig. 4.11).[38] The ECSA was then calculated for unmodified carbon electrodes from their specific capacitance using the typical value of 20 µF/cm^2.[26, 39] These electrodes were subsequently functionalized, and their specific capacitance was calculated from the double layer capacitance by using Eq. 1, with the assumption that the ECSA values did not change.

$$ECSA = C_{dl}/C_s \quad \text{(eq. 1)}$$

To test the assumption that the surface area was constant, a surface area analysis experiment was done on Sigracet carbon paper using Brunauer-Emmett-Teller (BET) analysis (Fig. 4.12, Table 4.2). BET analysis showed that the 4-(diazonium)benzenesulfonic acid functionalized paper had a lower micropore surface area than the heat-treated, unmodified electrodes by a factor of roughly 2, meaning that the increase in C_s calculated after functionalization with 4-(diazonium)benzenesulfonic acid may represent a significant underestimate.

Cyclic voltametric experiments showed that functionalization of carbon electrodes with 4-(diazonium)benzenesulfonic acid increases the value of C_s to approximately 40 µF/cm^2, a value close to

that measured for noble metals such as Pt in aqueous media.[39] Notably, McCreery and coworkers reported a larger (~200 µF/cm^2) but transient increase in C_s of glassy carbon electrodes upon laser activation.[20] Values of C_s, C_{dl}, k^0, and ECSA are tabulated in Table 4.3.

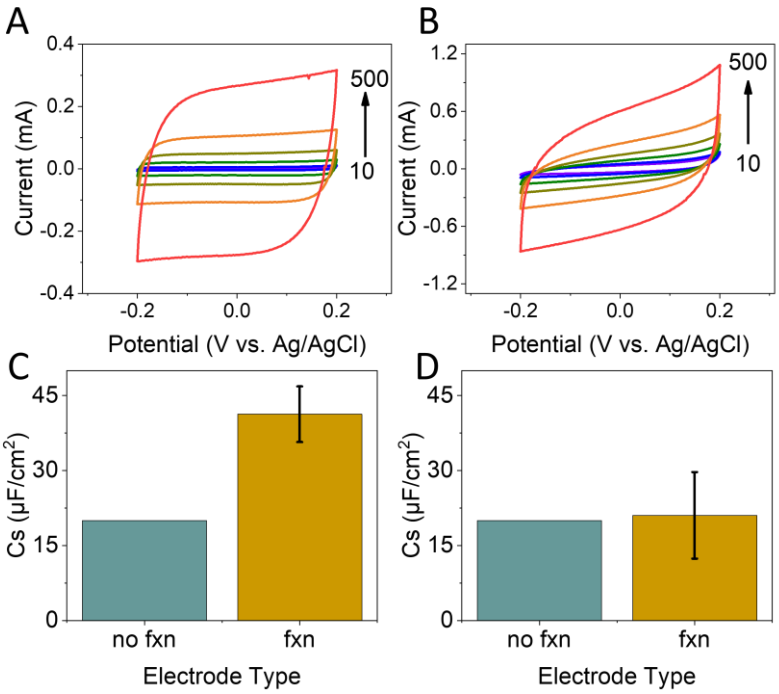

Figure 4.4. (A) Cyclic voltammetry in 1 M aqueous KOH measured at scan rates between 10 to 500 mV/s using unmodified graphitic rod electrodes and a (B) 4-(diazonium)benzenesulfonic acid modified electrodes. (C) Comparison of specific capacitance of unmodified (blue left "no fxn") and modified graphitic rod electrodes (yellow right "fxn") in 1 M aqueous KOH and (D) 0.2 M tetrabutylammonium hexafluorophosphate in acetonitrile.

The CV experiments were repeated in an aprotic solvent (acetonitrile) containing a non-coordinating electrolyte, where essentially no change was seen in the specific capacitance upon functionalization (Fig. 4.4D, Fig. 4.11). Recent experiments by Yoon et al. have shown that the C_s values of metal and metal oxide electrodes are similar when surface ion transfer reactions are eliminated by using non-aqueous, non-coordinating electrolyte solutions.[39] They note that deviations in values of C_s among different

electrode materials with otherwise identical ECSAs is due to specific adsorption of H^+/OH^- ions. Under aprotic conditions, no H^+/OH^- ions are present and thus cannot adsorb to the surface independent of material or relative hydrophilicity. As such, ECSA values measured under aprotic conditions and in the absence of coordinating ions are a "purer" comparison of actual surface areas. As will be noted in the discussion section, while adventitious hydrocarbons can alter the rate of interfacial electron transfer and the capacitance, we do not expect them to change the ECSA of the electrode material. And, because the modified and unmodified carbon electrodes show a similar trend to that shown by Yoon et al,[39] we have a further indication that functionalization with 4-(diazonium)benzenesulfonic acid results in a surface chemical change and thus a specific capacitance effect in water rather than a simple increase in surface area.

Comparative tests of modified and unmodified carbon paper electrodes were performed in an alkaline aqueous redox flow battery (ARFB) system previously described by Aziz and coworkers.[34] Polarization curves taken after reaching 100% state of charge (SOC) show current enhancement in the mass transfer region (peak current increase) and in the kinetic region of the curve (flattening of the slope) when the modified carbon electrodes are used (Fig. 4.5). This result holds over repetitive charge cycles and polarization curve tests (Fig. 4.13).

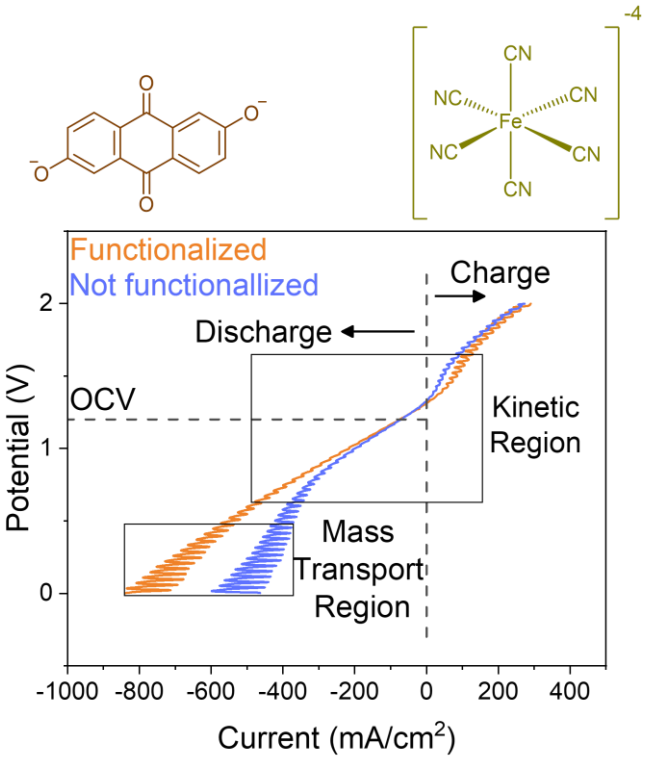

Figure 4.5. Polarization curves of alkaline ARFBs at 100% SOC composed of dihydroxy anthraquinone (upper left) against ferrocyanide (upper right) using thermally treated carbon paper electrodes (blue) and 4-(diazonium)benzenesulfonic acid treated carbon paper electrodes (orange).

Discussion

The functionalization of graphitic electrodes with 4-(diazonium)benzenesulfonic acid results in a permanent increase in both electron transfer kinetics and specific capacitance. Both effects can be interpreted in terms of the hydrophilicity of the modified surface, which inhibits the adsorption of electronically insulating molecules. As discussed by McCreery[20] and Liu,[21] removal of adventitious non-polar molecules from a carbon electrode surface improves the charge transfer kinetics between the electrode and solution-phase redox couples, and also increases the specific capacitance in aqueous

media. Interestingly, the physical and chemical methods that they use to activate carbon electrodes also render them hydrophilic, albeit transiently.

Two factors may contribute to the increase in specific capacitance of carbon electrodes. Following the Helmholtz model of double layer capacitance,[40] the electrode surface can be approximated as a simple capacitor of the form

$$C=\kappa\varepsilon_0(A/d) \qquad \text{(eq. 2)}$$

where C is capacitance, κ is the dielectric constant, ε_0 is the permittivity of free space, A is the area of the capacitor plates, and d is the distance between capacitor plates. According to equation 2, the capacitance may increase by increasing the dielectric constant, increasing the capacitor plate area, and/or decreasing the distance between the capacitor plates. As the ECSA is approximately constant in our experiments (Fig. 4.4D), it cannot contribute significantly to the increase in C_s. This leaves changes in κ and d as possibilities.

Following the Helmholtz model, adsorbed water within the outer Helmholtz plane (the first solvated plane of ions) serves as the dielectric in the double layer capacitor. Upon laser activation, heat treatment, or functionalization with 4-(diazonium)benzenesulfonic acid, the electrode surface becomes hydrophilic due to the removal of adventitious nonpolar molecules. The removal of this hydrophobic layer effectively moves the outer Helmholtz plane closer to the conductive electrode surface and thus lowers the value of d.

Concurrently, the hydrophilicity of the activated or chemically modified carbon surface may alter the local structure and dielectric properties of water. In the lyotropic (or Hofmeister) series,[41, 42] the arylsulfonate group is categorized as a structure breaker. Recent research by Fumagalli, et al. shows that

at a graphene surface, the dielectric constant of water differs greatly from that of bulk water, decreasing from a bulk value of 80 to ~3.[43] In the Helmholtz model, this interfacial layer comprises the dielectric of the capacitor. By disrupting the water structure at the graphite surface, the sulfonate groups may increase the local value of κ. Additionally, the specific adsorption of charged species (K^+ and OH^- in our experiments), which would likely be inhibited by the adsorption of hydrophobic contaminants, may also contribute to the observed increase in C_s. As noted in Yoon et. al., adsorption of OH^- ions in particular can dramatically alter the specific capacitance of an electrode material.[39]

Conclusion

Graphitic carbon electrodes were successfully modified with 4-(diazonium)benzenesulfonic acid to impart enhanced and permanent hydrophilicity to the carbon surface. These hydrophilic surfaces are resistant to deactivation effects commonly seen with carbon-based electrodes in aqueous media. The modified electrodes display enhanced double-layer and specific capacitance values akin to those of noble metals such as platinum, as well as markedly faster kinetics for electron transfer to aqueous one-electron redox couples. Improved ARFB performance was also found when modified electrodes were used, demonstrating their potential utility in electrochemical energy conversion and analytical applications in which carbon is the unique electrode material of choice.

Supporting Information

Materials

All chemicals were purchased from ThermoFisher Scientific and used as received unless otherwise noted. Carbon paper (Sigracet 39AA) was purchased from the Fuel Cell Store and treated as described below. Graphitic rods (014743.KN) were purchased from ThermoFisher Scientific. Highly ordered pyrolytic graphite (SPI-2) was also purchased from ThermoFisher Scientific. Nafion 212 was purchased from Ion Power and pretreated following literature methods.[34] Epoxy (Loctite 1373425 Hysol 1C, white) was purchased from Amazon. Silver paste (DuPont CP4922N-100) was purchased from Delta Technologies. Gasket material (PTFE 3/8", 9711k26) was purchased from McMaster Carr. Platinum wires (0.5 mm diameter, 99.95%) were purchased from Alfa Aesar. Ag/AgCl reference electrodes with 3 M NaCl filling solution were purchased from Microelectrode. The peristaltic pump was purchased from MasterFlex (Cole-Parmer, No. 7553-80). The flow battery cell was purchased from Scribner (Redox Flow Cell Test Fixture).

Carbon paper functionalization

As purchased carbon papers were thermally treated by baking at 400°C for 24hr under ambient conditions. Further functionalized samples were subsequently reacted with sulfanilic acid following a procedure adapted from a previously described method.[31] Briefly, 0.3 g of carbon paper, 0.6 g of sodium nitrite, and 1.3 g sulfanilic acid were carefully combined in a 250 mL Erlenmeyer flask containing 100 mL of nanopure water. 750 µL of concentrated hydrochloric acid was slowly added to generate 4-(diazonium)benzenesulfonic acid *in situ*. The flask opening was covered in parafilm wrap and placed on a shaker to gently agitate and react overnight. Following the reaction, the carbon paper was thoroughly washed with hot ethanol and left out to air dry before further use.

Graphitic rod electrode fabrication

Graphitic rods were entirely encapsulated in epoxy within a chemically resistive plastic rod roughly 1 cm in diameter. The electrode epoxy assembly was baked at 60-70 °C for 12 hours to ensure complete hardening of the epoxy coating. Once hardened, the epoxy surface was filed down with sandpaper (240 grit) until a small portion of the electrode was exposed (Fig 4.6). The electrode was finally polished with alumina slurry (1.0, 0.3, 0.05 µm) before use.

Highly ordered pyrolytic graphite (HOPG) functionalization

HOPG was functionalized as following a similar procedure to that used with the carbon paper. Briefly, a 0.178 g piece of HOPG was placed in an Erlenmeyer flask containing 30 mL of nanopure water, 0.38 g of sodium nitrite, 0.82 g of sulfanilic acid, and 470 µL of hydrochloric acid. The flask opening was covered in parafilm wrap and placed on a shaker to gently agitate and react overnight. Following the reaction, the HOPG was thoroughly washed with hot ethanol and left out to air dry before further use.

Electrochemical measurements

Cyclic voltammetry (CV) was conducted under specified electrolyte conditions. Platinum wire, graphitic rod electrodes, and Ag/AgCl were used as counter, working, and reference electrodes respectively in aqueous solutions. Acetonitrile-based electrolyte experiments used a platinum wire pseudo reference as the reference electrode. Scans were conducted using a PGSTAT302N (Metrohm, Autolab).

Redox flow battery testing was conducted using a Scribner flow cell following a cell setup previously reported[44,45] with a Nafion 212 membrane and an electrolyte composition of 4 mL of 0.5 2,6-dihydroxyanthraquinone (DHAQ) in 2 M potassium hydroxide vs. 15 mL of 0.4 M potassium ferrocyanide in 1 M potassium hydroxide as previously reported.[34] Redox flow battery (RFB) electrochemical

measurements were conducted using an EZStat Pro Potentiostat-Galvanostat (NuVant Systems). Charge/discharge experiments were conducted by galvanostatic application of a 100 mA/cm^2 bias with cutoff upper and lower potential limits of 1.6 V and 1.1 V with an electrolyte pump rate of 40 mL/min. Polarization curves were obtained after reaching 100% state of charge (SOC) by application of a CV scan taken between 2 V and 0.2 V at a scan rate of 100 mV/s.

XPS measurements

Experiments were performed using a Physical Electronics VersaProbe III with a monochromatic Al kα x-ray source. Scans were taken for C 1s, O 1s, F 1s, N 1s, and S 2p edges. Duplicate areas on each sample were initially analyzed by low energy resolution survey spectra. Most of those measurements showed excellent uniformity across the samples. In one case (functionalized HOPG edge) the measured composition was outside the expected uncertainty of the analysis so both locations were analyzed by high energy resolution spectra.

HOPG samples: The basal plane of the non-functionalized sample contained very little oxygen and a very narrow C 1s line shape. Both are consistent with a non-functionalized, well-ordered carbon. Note that the full-width-at-half-maximum (FWHM) on carbon can be broadened by (1) functionalization, (2) disorder and (3) the presence of both sp^2 and sp^3 carbon. Both (1) and (3) tend to broaden the envelope to the high binding energy side while (2) can broaden the entire envelop. The edge plane of the unfunctionalized HOPG contained more oxygen as well as certain impurities (Ca, S, Na and N). The functionalized HOPG contained N, O and S. There were higher levels of C, O and N on the edge planes relative to the basal planes. Sulfur was present in two chemical states, labeled “SO3” (167.7±0.1 eV) and “SO4” (168.6±0.2 eV) in Figure 4.8. The relative proportion of the two species varied from sample to sample. The basal plane samples also contained small amounts of Si (likely a siloxane).

Carbon paper samples: The untreated and heat-treated papers were very similar and contained very little O functionalization. The C 1s FWHM was broader than that of unfunctionalized HOPG suggesting more disorder. The functionalized carbon paper samples contained the highest levels of S and O of any sample type. They also contained Na, but little or no N.

Contact angle measurements

Water contact angles (WCA) on carbon paper were measured using a Ramé-Hart standard automated goniometer (model 200) with 5 µL drop size. WCA on HOPG were taken using a Hitachi camera and the National Instruments Vision Acquisition software. A 10 µL drop size was used.

Surface area measurements

Surface area measurements were taken on a TriStar II instrument using N_2 adsorption. A Brunauer-Emmett-Teller (BET) analysis model was applied to the collected data.

Supporting images

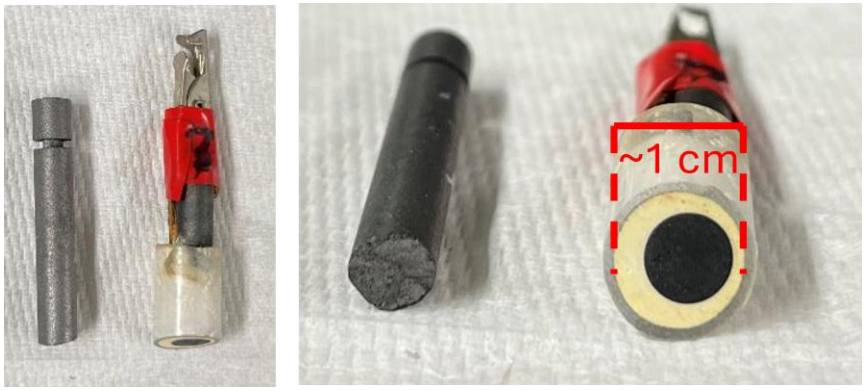

Figure 4.6. Fully constructed graphitic rod electrode next to a bare graphitic rod. While polished to a relatively flatter surface, the rod still retains noticeable surface roughness.

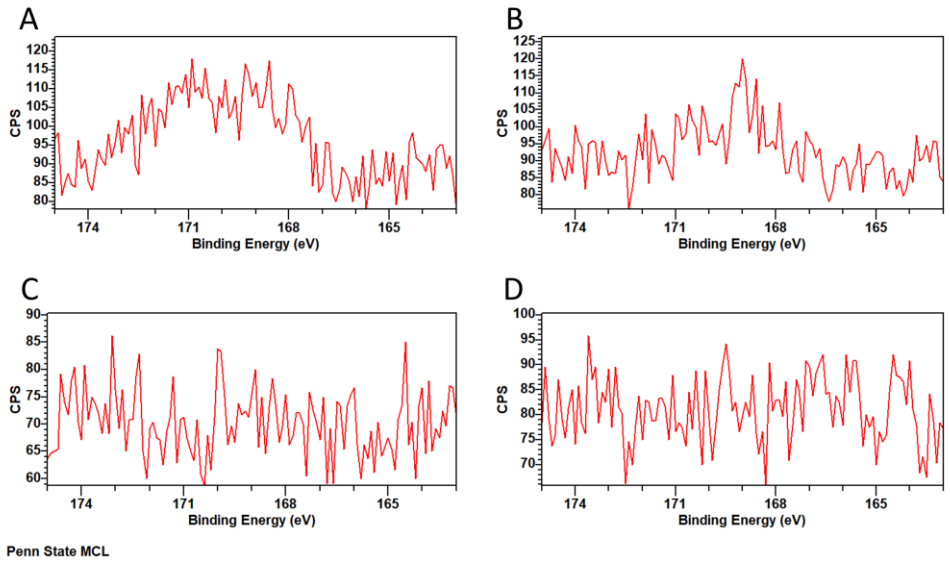

Figure 4.7. XPS Sulfur 2p spectra of unfunctionalized HOPG (A) edge sites and (B) basal plane sites and (C) as purchased carbon paper and (D) thermally treated carbon paper.

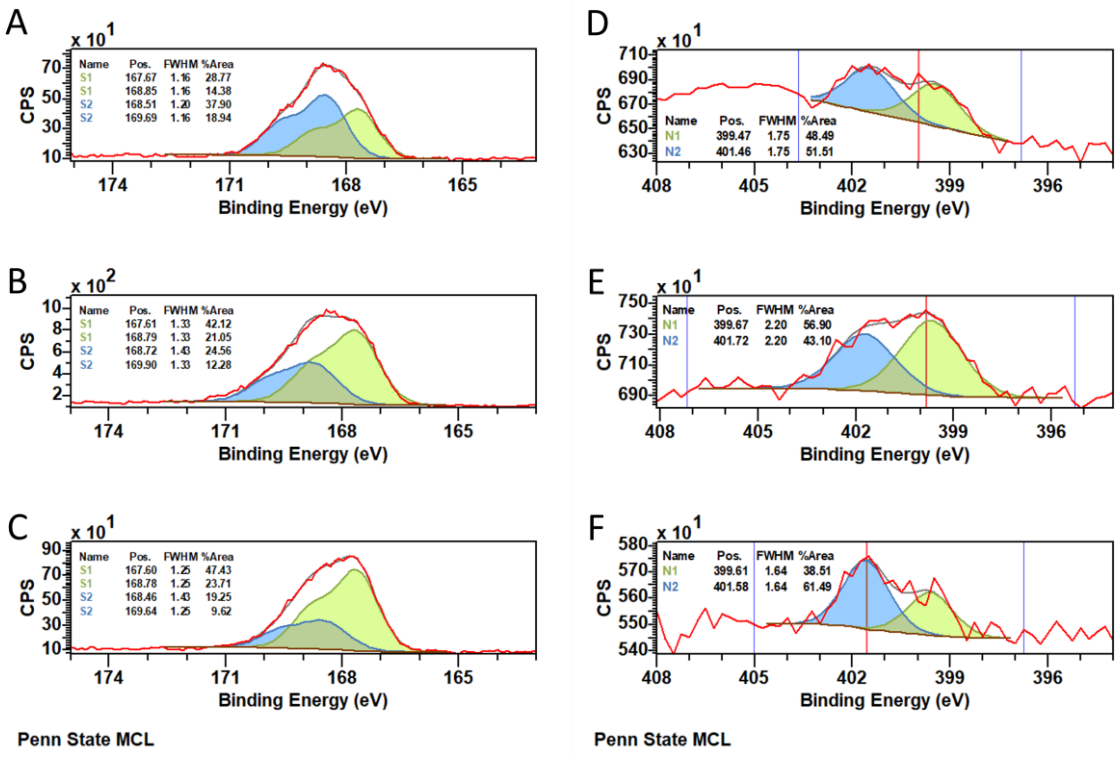

Figure 4.8. XPS Sulfur 2p spectra of 4-(diazonium)benzenesulfonic acid functionalized (A) HOPG edge sites, (B) HOPG basal plane sites, and (C) carbon paper and XPS Nitrogen 1s spectra of 4-(diazonium)benzenesulfonic acid functionalized (D) HOPG edge sites, (E) HOPG basal plane sites, and (F) carbon paper.

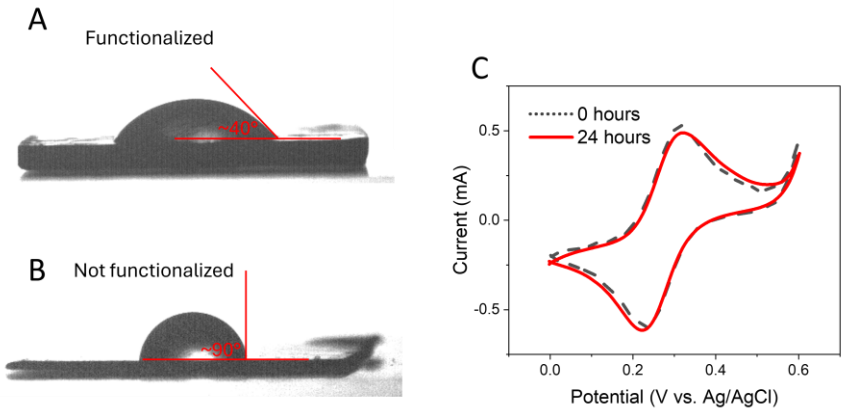

Figure 4.9. Water contact angle photos on the basal plane of HOPG (A) functionalized with 4-(diazonium)benzenesulfonic acid and (B) not functionalized. Notably, from XPS data (Table 4.1), the basal plane of HOPG is functionalized to a lesser extent than the defect- and edge-rich graphitic materials (carbon paper and HOPG edge). (C) Cyclic voltammetry of 10 mM potassium ferricyanide in 1 M potassium hydroxide taken at 100 mV/s scan rates at 0 hours of exposure to the solution (black dashed) and 24 hours of exposure to the solution (red solid).

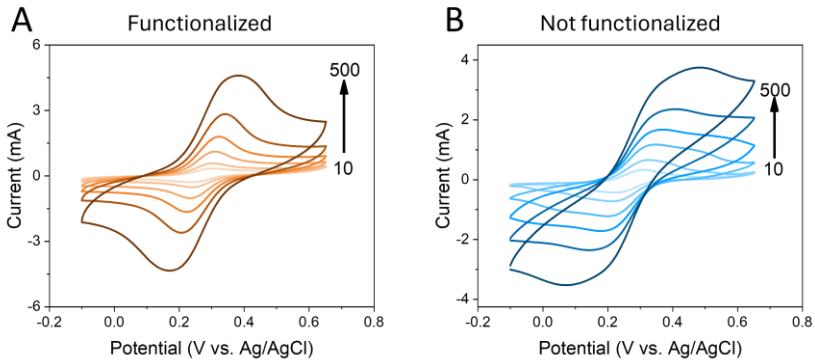

Figure 4.10. Cyclic voltammetry of 10 mM potassium ferricyanide in 1 M potassium hydroxide taken at 10, 20, 50, 100, 200, and500 mV/s scan rates using (A) a 4-(diazonium)benzenesulfonic acid functionalized graphitic rod electrode and (B) a not functionalized graphitic rod electrode.

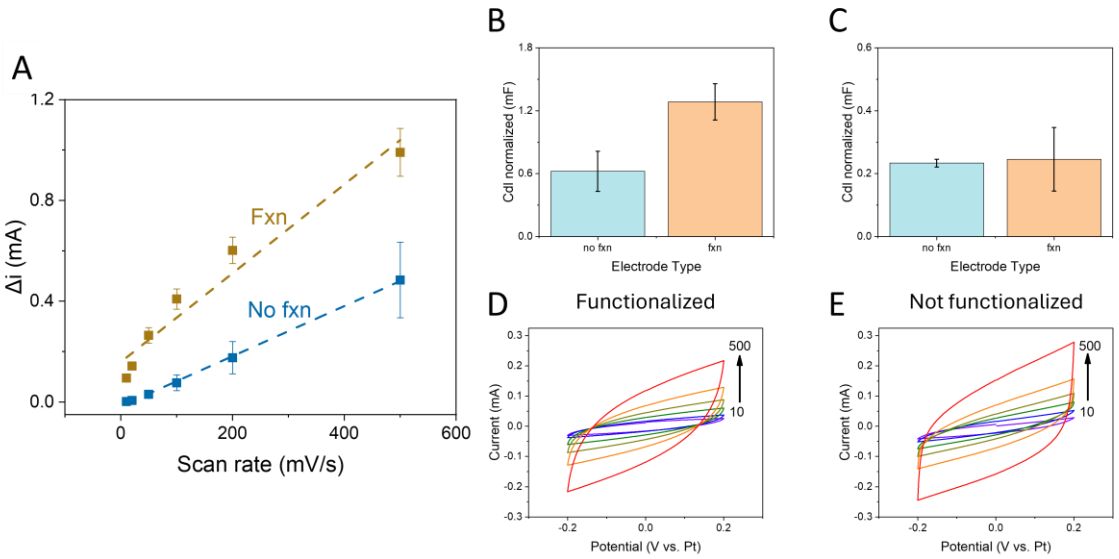

Figure 4.11. (A) Linear fitting analysis of protic (1 M potassium hydroxide) double layer experiments to solve for values of C_{dl} for 4-(diazonium)benzenesulfonic acid functionalized (orange "Fxn") and not functionalized (blue "No fxn") graphitic rod electrodes. And bar graph depictions of difference in double layer capacitance (C_{dl}) for not functionalized (blue) and 4-(diazonium)benzenesulfonic acid functionalized (orange) graphitic rod electrodes in (B) 1 M potassium hydroxide and (C) 0.2 M tetrabutylammonium hexafluorophosphate in acetonitrile. And Cyclic voltammetry of 0.2 M tetrabutylammonium hexafluorophosphate in acetonitrile taken from 10 to 500 mV/s scan rates using (D) a 4-(diazonium)benzenesulfonic acid functionalized graphitic rod electrode and (E) a not functionalized graphitic rod electrode.

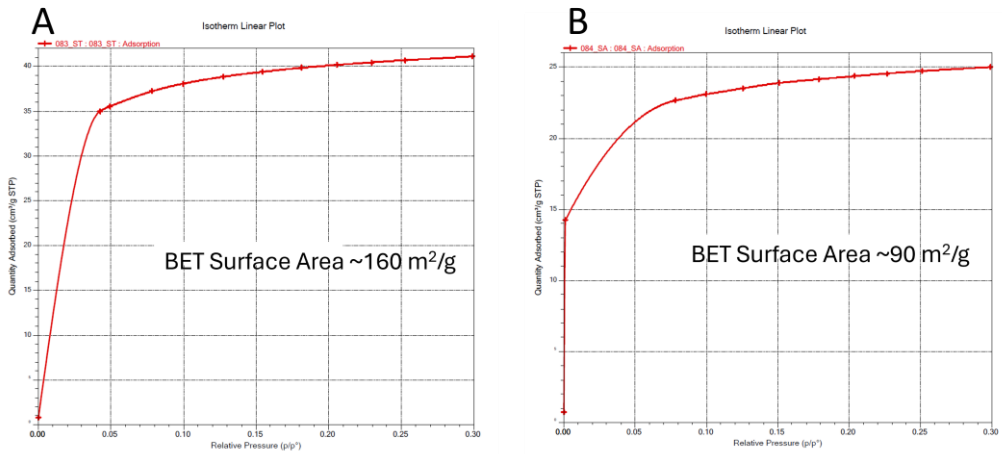

Figure 4.12. Nitrogen adsorption isotherm for thermally treated carbon paper (A) not functionalized and (B) functionalized. Data points (crosses) are fitted to the Brunauer-Emmett-Teller (BET) model (solid line).

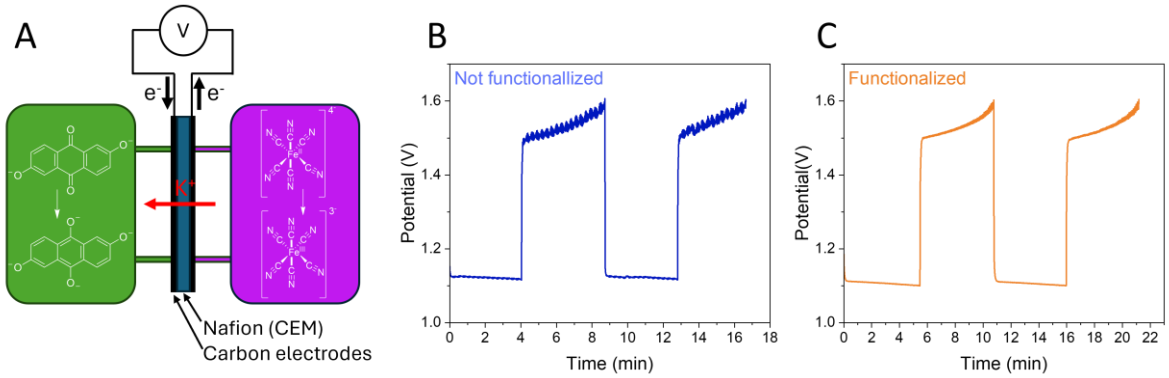

Figure 4.13. (A) Schematic diagram of the alkaline redox flow battery (ARFB) used in electrochemical experiments and example charge discharge curves following the ARFB experiment detailed in the methods section for a battery containing (B) unfunctionalized and (C) functionalized carbon paper electrodes. The set up of the system is detailed in the methods section of the SI, with both tests using the same electrolyte concentration, flow rate, and charging density.

Supporting tables

Table 4.1. XPS data

Sample	C	O	S	N
Purchased	98.9	1.1	-	-
No fxn	98.5	1.5	-	-
Fxn	85.2±2.7	10.3±2.3	2.4±0.7	0.4±0
No fxn HOPG edge	92.1	7.5	0.2	0.2
No fxn HOPG basal	98.8	1.2	-	-
Fxn HOPG edge	85.9±2.9	11.1±2.1	2.3±0.8	0.8±0.1
Fxn HOPG basal	91.0	6.1	1.1	0.7

XPS data for carbon paper as purchased, thermally treated but not functionalized ("No fxn"), and thermally treated and 4-(diazonium)benzenesulfonic acid functionalized ("fxn") as well as both functionalized and unfunctionalized HOPG samples. High resolution scan data are reported as atomic percentages.

Table 4.2. BET data

Electrode type	1	2	3	Average	Standard deviation
Not functionalized	160	120	125	135	22
Functionalized	90	75	80	82	8

BET surface areas of thermally treated but not functionalized carbon paper, and thermally treated and 4-(diazonium)benzenesulfonic acid functionalized carbon paper. Column 1 values are taken from the data shown in Figure 4.12. All values reported in m^2/g

Table 4.3. Accumulated electrochemical values

Electrode Type	k^0 (cm/s)	Cdl (mF)	Cs (µF/cm^2)	ECSA ** (cm^2)	Geometric area*** (cm^2)
Not functionalized	0.0035±0.001	0.5±0.1	20*	25±9	1.2
Functionalized	0.016 ±0.001	1.1±0.3	41±6	25±9	1.2

Compilation of calculated values for thermally treated but not functionalized electrodes, and thermally treated and 4-(diazonium)benzenesulfonic acid functionalized electrodes. Charge transfer rate constants (k^0) refer to 10 mM ferricyanide in 1 M potassium hydroxide solutions. Double layer capacitance (C_{dl}), specific capacitance (C_s), and electrochemically active surface area (ECSA) were calculated from experiments in 1 M potassium hydroxide solutions.

*Literature value as discussed in main body of manuscript

**~30% deviation is due to differences in roughness factor of each rod after sanding. As seen in Figure 4.6, bumps and cracks are visible on the rod after sanding.

***Calculated assuming a diameter of 6.15 mm

References

(1) Adams, K. L.; Puchades, M.; Ewing, A. G. In Vitro Electrochemistry of Biological Systems. *Annu. Rev. Anal. Chem.* **2008**, *1*, 329-355.

(2) Dayton, M. A.; Ewing, A. G.; Wightman, R. M. Response of Microvoltammetric Electrodes to Homogeneous Catalytic and Slow Heterogeneous Charge-Transfer reactions. *Anal. Chem.* **1980**, *52* (14), 2392-2396.

(3) Murray, R. W.; Ewing, A. G.; Durst, R. A. Chemically Modified Electrodes - Molecular Design for Electroanalysis. *Anal. Chem.* **1987**, *59* (5), 379A-390A.

(4) Amatore, C.; Arbault, S.; Guille, M.; Lemaître, F. Electrochemical monitoring of single cell secretion: Vesicular exocytosis and oxidative stress. *Chem. Rev.* **2008**, *108* (7), 2585-2621.

(5) Stulík, K.; Amatore, C.; Holub, K.; Marecek, V.; Kutner, W. Microelectrodes: Definitions, characterization, and applications (Technical Report). *Pure Appl. Chem.* **2000**, *72* (8), 1483-1492.

(6) Wightman, R. M.; Amatore, C.; Engstrom, R. C.; Hale, P. D.; Kristensen, E. W.; Kuhr, W. G.; May, L. J. Real-time characterization of Dopamine overflow and uptake in the rat striatum. *Neuroscience* **1988**, *25* (2), 513-523.

(7) Ostertag , B. J.; Ross , A. E. The Future of Carbon Based Neurochemical Sensing: A Critical Perspective. *ECS Sens. Plus* **2023**, 2, 043601.

(8) Wightman, R. M. Probing cellular chemistry in biological systems with microelectrodes. *Science* **2006**, *311* (5767), 1570-1574.

(9) Couper, A. M.; Pletcher, D.; Walsh, F. C. Electrode materials for electrosynthesis. *Chem. Rev.* **1990**, *90* (5), 837-865.

(10) Kawamata, Y.; Hayashi, K.; Carlson, E.; Shaji, S.; Waldmann, D.; Simmons, B. J.; Edwards, J. T.; Zapf, C. W.; Saito, M.; Baran, P. S. Chemoselective Electrosynthesis Using Rapid Alternating Polarity. *J. Am. Chem. Soc.* **2021**, *143* (40), 16580-16588.

(11) Wu, K. H.; Wang, D.; Lu, X. Y.; Zhang, X. F.; Xie, Z. L.; Liu, Y. F.; Su, B. J.; Chen, J. M.; Su, D. S.; Qi, W.; et al. Highly Selective Hydrogen Peroxide Electrosynthesis on Carbon: In Situ Interface Engineering with Surfactants. *Chem* **2020**, *6* (6), 1443-1458.

(12) Folkman, S. J.; Finke, R. G.; Galán-Mascarós, J. R.; Miyake, G. M. Carbon-Electrode-Mediated Electrochemical Synthesis of Hypervalent Iodine Reagents Using Water as the O-Atom Source. *ACS Sustain. Chem. Eng.* **2021**, *9* (31), 10453-10467.

(13) Liu, C. B.; Li, R.; Zhou, W.; Liang, Y.; Shi, Y. M.; Li, R. L.; Ling, Y. F.; Yu, Y. F.; Li, J. X.; Zhang, B. Selectivity Origin of Organic Electrosynthesis Controlled by Electrode Materials: A Case Study on Pinacols. *ACS Catal.* **2021**, *11* (14), 8958-8967.

(14) Cheng, Y. T.; Hao, Z. Q.; Hao, C. R.; Deng, Y.; Li, X. Y.; Li, K. X.; Zhao, Y. B. A review of modification of carbon electrode material in capacitive deionization. *RSC Adv.* **2019**, *9* (42), 24401-24419.

(15) Kim, K. J.; Park, M. S.; Kim, Y. J.; Kim, J. H.; Dou, S. X.; Skyllas-Kazacos, M. A technology review of electrodes and reaction mechanisms in vanadium redox flow batteries. *J. Mater. Chem. A.* **2015**, *3* (33), 16913-16933.

(16) Xing, L.; Shi, W. D.; Su, H. N.; Xu, Q.; Das, P. K.; Mao, B. D.; Scott, K. Membrane electrode assemblies for PEM fuel cells: A review of functional graded design and optimization. *Energy* **2019**, *177*, 445-464.

(17) Majlan, E. H.; Rohendi, D.; Daud, W. R. W.; Husaini, T.; Haque, M. A. Electrode for proton exchange membrane fuel cells: A review. *Renew. Sustain. Energy Rev.* **2018**, *89*, 117-134.

(18) Nibel, O.; Taylor, S. M.; Patru, A.; Fabbri, E.; Gubler, L.; Schmidta, T. J. Performance of Different Carbon Electrode Materials: Insights into Stability and Degradation under Real Vanadium Redox Flow Battery Operating Conditions. *J. Electrochem. Soc.* **2017**, *164* (7), A1608-A1615.

(19) Chakrabarti, M. H.; Brandon, N. P.; Hajimolana, S. A.; Tariq, E.; Yufit, V.; Hashim, M. A.; Hussain, M. A.; Low, C. T. J.; Aravind, P. V. Application of carbon materials in redox flow batteries. *J. Power Sources* **2014**, *253*, 150-166.

(20) Poon, M.; McCreery, R. L.; Engstrom, R. Laser activation of carbon electrodes - relationship between laser-induced surface effects and electron-transfer activation. *Anal. Chem.* **1988**, *60* (17), 1725-1730.

(21) Kozbial, A.; Zhou, F.; Li, Z. T.; Liu, H. T.; Li, L. Are Graphitic Surfaces Hydrophobic? *Acc. Chem. Res.* **2016**, *49* (12), 2765-2773.

(22) Li, Z. T.; Wang, Y. J.; Kozbial, A.; Shenoy, G.; Zhou, F.; McGinley, R.; Ireland, P.; Morganstein, B.; Kunkel, A.; Surwade, S. P.; et al. Effect of airborne contaminants on the wettability of supported graphene and graphite. *Nat. Mater.* **2013**, *12* (10), 925-931.

(23) Hurst, J. M.; Kim, M. A.; Peng, Z. B.; Li, L.; Liu, H. T. Assessing and Mitigating Surface Contamination of Carbon Electrode Materials. *Chem. Mater.* **2019**, *31* (18), 7133-7142.

(24) Takmakov, P.; Zachek, M. K.; Keithley, R. B.; Walsh, P. L.; Donley, C.; McCarty, G. S.; Wightman, R. M. Carbon Microelectrodes with a Renewable Surface. *Anal. Chem.* **2010**, *82* (5), 2020-2028.

(25) Yue, L.; Li, W. S.; Sun, F. Q.; Zhao, L. Z.; Xing, L. D. Highly hydroxylated carbon fibres as electrode materials of all-vanadium redox flow battery. *Carbon* **2010**, *48* (11), 3079-3090.

(26) Yang, S. D.; Chen, Q. Quantifying Electron Transfer Kinetics on Porous Carbon Electrodes for Redox Flow Batteries. *J. Electrochem. Soc.* **2020**, *167* (16), 160501.

(27) Patel, A. N.; Collignon, M. G.; O'Connell, M. A.; Hung, W. O. Y.; McKelvey, K.; Macpherson, J. V.; Unwin, P. R. A New View of Electrochemistry at Highly Oriented Pyrolytic Graphite. *J. Am. Chem. Soc.* **2012**, *134* (49), 20117-20130.

(28) Güell, A. G.; Cuharuc, A. S.; Kim, Y. R.; Zhang, G. H.; Tan, S. Y.; Ebejer, N.; Unwin, P. R. Redox-Dependent Spatially Resolved Electrochemistry at Graphene and Graphite Step Edges. *ACS Nano* **2015**, *9* (4), 3558-3571.

(29) Liu, C. M.; Sun, C. X.; Gao, Y. J.; Lan, W. J.; Chen, S. W. Improving the Electrochemical Properties of Carbon Paper as Cathodes for Microfluidic Fuel Cells by the Electrochemical Activation in Different Solutions. *ACS Omega* **2021**, *6* (29), 19153-19161.

(30) He, D.; Soo, V. K.; Stojcevski, F.; Lipinski, W.; Henderson, L. C.; Compston, P.; Doolan, M. The effect of sizing and surface oxidation on the surface properties and tensile behaviour of recycled carbon fibre: An end-of-life perspective. *Compos. -A: Appl. Sci.* **2020**, *138*, 106072.

(31) Schrick, B.; Hydutsky, B. W.; Blough, J. L.; Mallouk, T. E. Delivery vehicles for zerovalent metal nanoparticles in soil and groundwater. *Chem. Mater.* **2004**, *16* (11), 2187-2193.

(32) Belmont, J. A.; Amici, R. M.; Galloway, C. P. Reaction of carbon black with diazonium salts, resultant carbon black products and their uses. US5851290A, 1998.

(33) Hart, N. T.; Lane, W. C.; de la Garza, L. Electrochemical Quantification of Acetaminophen: An Engaging Cyclic Voltammetry Laboratory for the Quantitative Analysis Course. *J. Chem. Educ.* **2020**, *97* (8), 2254-2259.

(34) Lin, K. X.; Chen, Q.; Gerhardt, M. R.; Tong, L. C.; Kim, S. B.; Eisenach, L.; Valle, A. W.; Hardee, D.; Gordon, R. G.; Aziz, M. J.; et al. Alkaline quinone flow battery. *Science* **2015**, *349* (6255), 1529-1532.

(35) Nicholson, R. S. Theory and application of cyclic voltammetry for measurement of electrode reaction kinetics. *Anal. Chem.* **1965**, *37* (11), 1351.

(36) Sarac, H.; Patrick, M. A.; Wragg, A. A. Physical-properties of the ternary electrolyte potassium ferri-ferrocyanide in aqueous sodium hydroxide solution. *J. Appl. Electrochem.* **1993**, *23* (1), 51-55.

(37) Winkler, K. The kinetics of electron-transfer in $Fe(CN)_6^{4-/3-}$ redox system on platinum standard-size and ultramicroelectrodes. *J. Electroanal. Chem.* **1995**, *388* (1-2), 151-159.

(38) Morales, D. M.; Risch, M. Seven steps to reliable cyclic voltammetry measurements for the determination of double layer capacitance. *J. Phys. Energy* **2021**, *3* (3), 034013.

(39) Yoon, Y.; Yan, B.; Surendranath, Y. Suppressing Ion Transfer Enables Versatile Measurements of Electrochemical Surface Area for Intrinsic Activity Comparisons. *J. Am. Chem. Soc.* **2018**, *140* (7), 2397-2400.

(40) Bard, A. J.; Faulkner, L. R. *Electrochemical Methods Fundamentals and Applications*; John Wiley & Sons, 2001.

(41) Kang, B. B.; Tang, H. C.; Zhao, Z. D.; Song, S. S. Hofmeister Series: Insights of Ion Specificity from Amphiphilic Assembly and Interface Property. *ACS Omega* **2020**, *5* (12), 6229-6239.

(42) Dillenburger, J. D.; Schulte, L.; Mahale, P.; Suleiman, M.; Mallouk, T. E. Anion-Dependent Structure, Dehydration, and Hydroxide Ion Conductivity of Magnesium Aluminum Layered Double Hydroxides. *Chem. Mater.* **2023**, *35* (16), 6437-6446.

(43) Fumagalli, L.; Esfandiar, A.; Fabregas, R.; Hu, S.; Ares, P.; Janardanan, A.; Yang, Q.; Radha, B.; Taniguchi, T.; Watanabe, K.; et al. Anomalously low dielectric constant of confined water. *Science* **2018**, *360* (6395), 1339.

(44) Metlay, A. S.; Chyi, B.; Yoon, Y.; Wycisk, R. J.; Pintauro, P. N.; Mallouk, T. E. Three-Chamber Design for Aqueous Acid-Base Redox Flow Batteries. ACS Energy Letters, 2022.

(45) Yan, Z. F.; Wycisk, R. J.; Metlay, A. S.; Xiao, L. Q.; Yoon, Y.; Pintauro, P. N.; Mallouk, T. E. High-Voltage Aqueous Redox Flow Batteries Enabled by Catalyzed Water Dissociation and Acid-Base Neutralization in Bipolar Membranes. *ACS Cent. Sci.* **2021**, *7* (6), 1028-1035.

CHAPTER 5: CONCLUSIONS AND OUTLOOK

Conclusion

Recently, bipolar membrane (BPM) technologies have entered a renaissance period, with the abundance of fundamental research on BPMs leading to an increased integration and development of BPM devices. The acid-base redox flow battery (RFB), a BPM containing RFB, is of particular interest to BPM research due to its bidirectional use, and thus necessary forward and reverse bias development. In this dissertation, we compartmentalized the acid-base redox flow battery system and conducted fundamental research on the individual components of a flow battery system (e.g. membranes, device design, electrodes).

In chapter 2, graphite oxide (GO) as a BPM water dissociation catalyst was studied. Ordered deposition of GO was demonstrated to grant some leverage towards understanding the relationship between degree of areal coverage and electrochemical performance. GO was found to have higher conductivity towards protons than hydroxide ions, leading to a threshold oriented coverage point after which, water formation from hindered hydroxide ion transport begins to compete with migratory separation of protons and hydroxide ions. This increased water association reaction density leads to BPMs with higher overpotentials and is theoretically supported by two simplified numerical models.

In chapter 3, a three-chamber acid-base redox flow battery system was discussed. Compared to the original two-chamber system, the three-chamber design was found to mitigate membrane fouling arising from ferro/ferricyanide exchange into a BPM's AEL. This new design also allowed for new flexibility in selecting catholyte redox species, leading to the assembly of a bromine-anthraquinone system with a remarkably high open circuit voltage of ~1.7 V.

In chapter 4, charge transfer kinetics and capacitance at a functionalized graphitic electrode surface was investigated. We hypothesized that functionalization of a graphitic electrode with 4-(diazonium)benzenesulfonic acid demonstrated both an increase in heterogeneous charge transfer to a one electron redox couple and increased specific capacitance due to two primary factors related to the functional group's imparted hydrophilicity. Following the Helmholtz model for an electrode's double layer capacitance, (1) increased hydrophilicity limited the amount of hydrophobic adventitious hydrocarbons adsorbed to the electrode surface, and thus shortened the dielectric distance in the electrode's double layer. (2) Following precedent on the rigid ordering of water at hydrophobic surfaces, the increased hydrophilicity decreased the order of water and thus increased the dielectric constant of water at the electrode surface.

One major segment of the acid-base redox flow battery system that remains open to development is the chosen redox species for the anolyte and catholyte. As noted in chapter 3, the requirements that must be met for the redox species, particularly the catholyte, are restrictive. Both species must be aqueous stable and highly soluble, and, for more practical commercialization, ideally air stable and composed of inexpensive materials.[1, 2] In the classic two-chamber acid-base redox flow battery system, the anolyte redox species must also be electronegative, acid stable, and ideally anionic. Thus, organic molecules functionalized with strong acid components like sulfate groups can make for good anolyte candidates. Conversely, the catholyte redox species must be electropositive, alkaline stable, and ideally cationic.[3] Throughout the literature, such strict molecular requirements are difficult to find. A quaternary ammonium functional group would itself impose cationic properties, but is a good organic leaving group, and can make the overall redox molecule susceptible to elimination reactions.[4] While the three-chamber design partially alleviates some of these concerns, the requirements remain stringent.[5]

Recent work from Li et. al.[6] demonstrated principles of molecular size exclusion mitigating crossover of active redox species. Beyond molecular systems, material-based slurry systems have shown some recent precedent in electrochemical devices like pseudocapacitive flow capacitors for desalination and energy storage applications.[7-9] Importantly, molecules encapsulated by slurry materials are no longer in direct contact with the surrounding electrolyte, and thus can display increased stability and solubility. However, reported slurry systems generally use some sort of porous carbon particle that is microns in size. In typical redox flow battery systems, charge transfer from the electrode to the reactive species is diffusion dependent, and thus size dependent. The timescale of diffusion to the electrode for these micron-sized slurry systems is too long for practical utilization in a flow battery.[10] Nanosized porous materials like nanozeolites offer an interesting carbon particle alternative for these slurry systems. Faujasite-Y in particular has wide literature precedent for nanosized synthesis[11] as well as redox species encapsulation.[12] Utilization of a nanozeolite slurry system would not only mitigate crossover issues seen in all redox flow battery systems through a size exclusion approach, but would also mitigate redox species restrictions like solubility and stability encountered in the acid-base redox flow battery system, thus vastly expanding the library of possible redox species.

Overall, while much recent progress has been made in the field of BPMs and BPM device integration, the area remains ripe for continued research and development towards a complete fundamental understanding of BPM systems.

References

(1) Winsberg, J.; Hagemann, T.; Janoschka, T.; Hager, M. D.; Schubert, U. S. Redox-Flow Batteries: From Metals to Organic Redox-Active Materials. *Angew. Chem. Int. Ed.* **2017**, *56* (3), 686-711.

(2) Chen, H. N.; Cong, G. T.; Lu, Y. C. Recent progress in organic redox flow batteries: Active materials, electrolytes and membranes. *J. Energy Chem.* **2018**, *27* (5), 1304-1325.

(3) Yan, Z. F.; Wycisk, R. J.; Metlay, A. S.; Xiao, L. Q.; Yoon, Y.; Pintauro, P. N.; Mallouk, T. E. High-Voltage Aqueous Redox Flow Batteries Enabled by Catalyzed Water Dissociation and Acid-Base Neutralization in Bipolar Membranes. *ACS Cent. Sci.* **2021**, *7* (6), 1028-1035.

(4) Wade, L. G. *Organic Chemistry*; Pearson Education, Inc., 2013.

(5) Metlay, A. S.; Chyi, B.; Yoon, Y.; Wycisk, R. J.; Pintauro, P. N.; Mallouk, T. E. Three-Chamber Design for Aqueous Acid-Base Redox Flow Batteries. *ACS Energy Lett.* **2022**, 7 (3), 908-913.

(6) Li, X.; Gao, P. Y.; Lai, Y. Y.; Bazak, J. D.; Hollas, A.; Lin, H. Y.; Murugesan, V.; Zhang, S. Y.; Cheng, C. F.; Tung, W. Y.; et al. Symmetry-breaking design of an organic iron complex catholyte for a long cyclability aqueous organic redox flow battery. *Nat. Energy*, **2021**, 6, 873-881.

(7) Hatzell, K. B.; Beidaghi, M.; Campos, J. W.; Dennison, C. R.; Kumbur, E. C.; Gogotsi, Y. A high performance pseudocapacitive suspension electrode for the electrochemical flow capacitor. *Electrochim. Acta* **2013**, *111*, 888-897.

(8) Tomai, T.; Mitani, S.; Komatsu, D.; Kawaguchi, Y.; Honma, I. Metal-free aqueous redox capacitor via proton rocking-chair system in an organic-based couple. *Sci. Rep.* **2014**, 4, 3591.

(9) Rommerskirchen, A.; Kalde, A.; Linnartz, C. J.; Bongers, L.; Linz, G.; Wessling, M. Unraveling charge transport in carbon flow-electrodes: Performance prediction for desalination applications. *Carbon* **2019**, *145*, 507-520.

(10) Bard, A. J.; Faulkner, L. R. *Electrochemical Methods Fundamentals and Applications*; **2001**.

(11) Awala, H.; Gilson, J. P.; Retoux, R.; Boullay, P.; Goupil, J. M.; Valtchev, V.; Mintova, S. Template-free nanosized faujasite-type zeolites. *Nat. Mater.* **2015**, *14* (4), 447-451.

(12) Sewell, G.; Forster, R. J.; Keyes, T. E. Influence of steric confinement within zeolite Y on photoinduced energy transfer between $Ru(bpy)_3^{2+}$ and iron polypyridyl complexes. *J. Phys. Chem. A.* **2008**, *112* (5), 880-888.